UNIWERSYTET IM. ADAMA MICKIEWICZA W POZNANIU

Rozprawa doktorska

DIFFUSION AND STRUCTURAL CHANGES IN $Al_{1-x}Si_xO_y$ THIN FILMS

investigated by Time-of-Flight Secondary Ion Mass Spectroscopy

mgr Paweł Piotr Michałowski

Promotor pracy: dr hab. Maciej Wiesner

Poznań, 2014

Oświadczenie autora pracy

Ja, niżej podpisany mgr Paweł Piotr Michałowski oświadczam, że przedkładaną pracę magisterską pt:

Diffusion and structural changes in $Al_{1-x}Si_xO_y$ thin films; investigated by Time-of-Flight Secondary Ion Mass Spectroscopy

napisałem samodzielnie. Oznacza to, że przy pisaniu pracy, poza niezbędnymi konsultacjami, nie korzystałem z pomocy innych osób, a w szczególności nie zlecałem opracowania rozprawy lub jej istotnych części innym osobom, ani nie odpisywałem tej rozprawy lub jej istotnych części od innych osób.

Oświadczam ponadto, że wydrukowana oraz elektroniczna wersja pracy są identyczne.

Podziękowania

Dziękuję Bogu za wszelkie udzielone mi łaski w życiu osobistym jak i zawodowym. Od Niego otrzymałem zdolności abym mógł ukończyć tę pracę i Jemu się nieustannie zawierzam.

Pracę dedykuję Ewie Jakubowskiej, dzięki której każdego dnia staję się lepszym człowiekiem. Dziękuję Ci za Twoją cierpliwość i codzienną modlitwę, a przede wszystkim za wszystkie dni, które spędziliśmy i spędzimy razem.

Dziękuję mojej Rodzinie, Mamie, Tacie, Anitce i Jurkowi wraz z Miłoszem i Juliuszem, Asi i Michałowi. To wspaniałe uczucie gdy człowiek może liczyć na wsparcie tak wielu cudownych osób!

Dziękuję ojcom i braciom Pasjonistom za wsparcie duchowe w najtrudniejszym okresie powstawania niniejszej pracy.

Dziękuję Panom Dziekanom Wydziału Fizyki Uniwersytetu Adama Mickiewicza, prof. dr hab. Antoniemu Wójcikowi oraz prof. dr hab. Adamowi Lipowskiemu za umożliwienie mi obrony pracy doktorskiej. Dziękuję mojemu promotorowi, dr hab. Maciejowi Wiesnerowi za wszystkie cenne uwagi i konsultacje.

Nie sposób wymienić wszystkich osób, które dobrą radą, życzliwym słowem lub ciepłym uśmiechem pomogły mi w napisaniu tej pracy. Wszystkim Wam z całego serca dziękuję!

Paweł Piotr Michałowski

Streszczenie

Aby umożliwić dalszy rozwój pamięci typu flash należy zastąpić powszechnie dziś używaną krzemionkę cienką warstwą materiału o wysokiej stałej dielektrycznej, co umożliwi dalszą miniaturyzację zapobiegając równocześnie wzrostowi prądu tunelowego. Aby tego dokonać potrzebne są szczegółowe badania, które mogą wyłonić najbardziej odpowiedni materiał z bardzo licznego grona potencjalnych kandydatów.

W niniejszej pracy główną metodą pomiarową była Spektroskopia Mass Jonów Wtórnych wyposażona w analizator czasu przelotu (z angielskiego ToF-SIMS), którą przebadano cienkie warstwy kompozytowego materiału $Al_{1-x}Si_xO_y$ o zróżnicowanej strukturze, począwszy od czystego tlenku aluminium (x = 0) aż do x $\approx$ 0.4. Próbki zostały wytworzone przy pomocy techniki Atomic Layer Deposition (ALD) na podłożu krzemowym Si(001) z naturalną warstwą tlenku lub dodatkową warstwą Si_3N_4 o grubości 6nm. Następnie próbki poddano obróbce termicznej poprzez zastosowanie metody Rapid Thermal Annealing (RTA) w szerokim zakresie temperatur (650 - 1100°C) oraz w różnych atmosferach (azotowej, tlenowej i wodorowej).

W trakcie pracy zidentyfikowano i scharakteryzowano wiele zjawisk fizycznych wywołanych przez obróbkę termiczną: krystalizację, kurczenie, gęstnienie oraz dyfuzję krzemu z substratu poprzez cienkie warstwy, której poświęcono najwięcej uwagi w niniejszej pracy. Wykazano, że w próbkach krystalicznych dominującym mechanizmem jest dyfuzja wzdłuż granicy ziaren polikrystalicznych.

W dalszej części pracy dokonano opisu ilościowego zjawiska dyfuzji i wykazano, że energia aktywacji zależy od ilości krzemu zawartego w materiale kompozytowym i zmienia się zgodnie z następującymi wzorami: $E_a = 0.8 - 0.51x$ eV dla próbek amorficznych oraz $E_a = 2.64 + 1.65x$ eV i $E_a = 3.10 - 0.53x$ eV dla próbek krystalicznych wytworzonych na naturalnym tlenku oraz z dodatkową warstwą azotku krzemu. Szczegółowa analiza tzw. profilów głębokości wykonanych metodą SIMS dostarczyła satysfakcjonującego wyjaśnienia tego faktu: tlenek krzemu posiada silną tendencję do reakcji z warstwą $Al_{1-x}Si_xO_y$ tworząc w ten sposób warstwę przejściową, która znacznie

utrudnia dalszą dyfuzję krzemu z substratu. Stwierdzono, że krzem, który dotarł na powierzchnię próbki zostaje tam uwięziony i w trakcie dalszej obróbki termicznej nie powraca wgłąb próbki, a jedynie porusza się po powierzchni cienkiego filmu. Wyznaczono, że energia aktywacji dyfuzji powierzchniowej wynosi $E_a = 1.50 \pm 0.03$ eV, a maksymalny współczynnik proporcjonalności dyfuzji powierzchniowej jest o dwa rzędy wielkości większy od dyfuzji w poprzek próbki i dlatego w czasie długotrwałej obróbki termicznej na powierzchni próbki tworzy się jednorodna warstwa krzemu. Za pomocą trzech niezależnych metod wykazano, że w pewnym momencie następuje wysycenie tego procesu i krzem nie może już w większych ilościach gromadzić się na powierzchni próbki.

W dalszej części dokonano ilościowego opisu procesu dyfuzji. Maksymalny współczynnik proporcjonalności dyfuzji D_0 (w nieskończenie wysokiej temperaturze) dla czystego tlenku aluminium wynosi $(1.6 \pm 0.3) \times 10^{-12}\mathrm{cm}^2/\mathrm{s}$, $(2.9 \pm 0.2) \times 10^{-4}\mathrm{cm}^2/\mathrm{s}$ oraz $(6.7 \pm 0.2) \times 10^{-3}\mathrm{cm}^2/\mathrm{s}$ dla (odpowiednio) próbek amorficznych, krystalicznych wytworzonych na naturalnym tlenku oraz krystalicznych z dodatkową warstwą azotku krzemu. Dokładna analiza profili głębokości pozwoliła na wyjaśnienie tej rozbieżności między dwoma typami próbek: okazało się, że SiO_2 znacznie łatwiej wchodzi w reakcję z warstwą $Al_{1\text{-}x}Si_xO_y$ tworząc warstwę przejściową, która wstrzymuje dalszą dyfuzję.

Poprawność wyznaczonych parametrów dyfuzji potwierdzono dodatkowo badaniami dielektrycznymi. Porównano wartości eksperymentalne względnej przenikalności elektrycznej oraz obliczone na podstawie modelu teoretycznego i okazało się, że wszystkie wartości (dla różnych grubości próbek i/lub zmiennych parametrów obróbki termicznej) pozostają w zgodzie.

Abstract

The development of the next generation charge trapping non-volatile memory devices requires replacement of the blocking oxide material (currently SiO_2) with a high-k dielectric thin film. Precise analytical characterization may appoint the most potent material from a large variety of possible candidates.

This work focuses on the Time-of-Flight Secondary Ion Mass Spectroscopy (ToF-SIMS) of $Al_{1-x}Si_xO_y$ thin films with composition varying from pure Al_2O_3 up to x $\approx$ 0.4. Samples were fabricated by the Atomic Layer Deposition (ALD) on Si(001) wafers with either native oxide or additional 6 nm thick Si_3N_4 layer and further treated by the Rapid Thermal Annealing (RTA) in a wide range of temperatures (650 - 1100°C) and ambients (nitrogen, oxygen, hydrogen).

Variety of thermal induced phenomena were identified and properly characterized: crystallization, compaction, densification and the diffusion of silicon from the substrate which was the central aspect of this work. The grain boundary diffusion was identified as the diffusion mechanism in crystalline samples. The diffusion-induced surface segregation of silicon was further inquired into and the activation energy of the surface diffusion was found to be $E_a = 1.50 \pm 0.03$ eV. Furthermore it was acknowledged that the diffusion coefficient of the surface diffusion is two orders of magnitude higher than in the bulk and thus formation of an evenly segregated layer during the thermal processing is expected. Three independent methods proved that this process was saturable and at one point no more silicon could be agglomerated at the surface of the sample.

It was further noted that the activation energy of the diffusion depends on the amount of silicon in compound material and the relation was found to be $E_a = 0.8 - 0.51x$ eV for amorphous samples and $E_a = 2.64 + 1.65x$ eV and $E_a = 3.10 - 0.53x$ eV for crystalline samples deposited on native oxide and silicon nitride, respectively. Detailed analysis of the SIMS depth profiles provides a satisfactory explanation of this phenomenon: SiO_2 has much stronger tendency to react with $Al_{1-x}Si_xO_y$ material forming an interface layer that restrain further diffusion of Si from the substrate.

The corresponding pre-exponential factor D_0 (the diffusion coefficient at infinite temperature) for pure alumina thin films was found to be $(1.6\pm0.3)\times 10^{-12}\text{cm}^2/\text{s}$, $(2.9\pm0.2)\times10^{-4}\text{cm}^2/\text{s}$ and $(6.7\pm0.2)\times10^{-3}\text{cm}^2/\text{s}$ for amorphous, crystalline deposited on oxide and crystalline deposited on nitride samples, respectively.

The validity of the diffusion parameters was further confirmed by the dielectric measurements. The theoretical and experimental values of the relative permittivity of the samples were compared and found to be in an agreement.

Contents

Podziękowania **3**

Streszczenie **5**

Abstract **7**

1 Introduction **13**

2 Theory **15**
2.1 High-k materials 15
2.1.1 Moore's law and its limitation 15
2.1.2 New materials 16
2.1.3 Aluminum oxide 17
2.2 Defects 17
2.2.1 Point defects 18
2.2.2 Linear Defects - Dislocations 21
2.2.3 Planar defects 22
2.2.4 Bulk defects 26
2.2.5 Defect interaction 27
2.3 Diffusion in solids 29
2.3.1 Fick's laws of diffusion 30
2.3.2 Solutions to the diffusion equations 32
2.3.3 Arrhenius equation 47
2.3.4 Diffusion mechanism 48
2.3.5 Limitations of the diffusion process 52

3 Experimental setups **59**
3.1 Sample preparation 59
3.1.1 Atomic Layer Deposition 59
3.1.2 Rapid thermal annealing 60
3.2 Diagnostics 62

3.2.1 Ellipsometry . . . 62
3.2.2 Grazing incidence X-ray diffraction . . . 64
3.2.3 X-ray reflectometry . . . 65
3.2.4 X-ray photoelectron spectroscopy . . . 66
3.2.5 Capacitance-voltage profiling . . . 68
3.2.6 Atomic Force Microscopy . . . 68
3.2.7 Time-of-Flight Secondary Ion Spectroscopy . . . 70
3.2.7.1 Basic principles . . . 70
3.2.7.2 Operation modes . . . 74
3.2.7.3 Experimental setup . . . 77
3.2.7.4 Data evaluation . . . 81

4 Results and discussion 91
4.1 Basic characterization . . . 91
4.1.1 Crystallization . . . 91
4.1.2 Compaction and densification . . . 91
4.2 ToF-SIMS depth profiling . . . 92
4.2.1 Quantification . . . 93
4.2.2 Segregation . . . 96
4.3 Annealing conditions . . . 96
4.3.1 Annealing ambients . . . 96
4.3.2 Cooling rate . . . 98
4.3.3 Diffusion mechanism . . . 102
4.4 Diffusion model . . . 102
4.4.1 Source boundary condition . . . 102
4.4.2 Diffusion in the thin film region . . . 103
4.4.3 Surface boundary condition . . . 105
4.4.3.1 Time dependent relation . . . 105
4.4.3.2 Surface diffusion . . . 109
4.4.3.3 Conclusions . . . 112
4.4.4 Conclusions . . . 112
4.5 Diffusion parameters . . . 113
4.5.1 Diffusion coefficient . . . 114
4.5.2 Diffusion length . . . 116
4.5.3 Activation energy . . . 117
4.5.4 Conclusions . . . 118
4.6 Samples with different compositions . . . 118
4.6.1 Si_3N_4 sublayer . . . 118
4.6.2 Composite material $Al_{1-x}Si_xO_y$ . . . 123
4.7 Dielectric measurements . . . 127
4.7.1 Amorphous samples . . . 128

4.7.2 Crystalline samples 130
4.7.3 Interface 133

5 Summary **137**
5.1 Results 137
5.2 Usefulness of ToF-SIMS technique 140

Bibliography **143**

Chapter 1

Introduction

The development of electronic devices is one of the most crucial task of the human society. The wide range of appliances like memory and processing units for computers, sources of a renewable energy, batteries, sensors, actuators and many more are increasing the quality of a human life. The present technology is reaching its limit and better devices cannot be manufactured just by improvement of the well known solutions. A breakthrough came with nanotechnology: an interdisciplinary science compromising fields of physics, chemistry, biology, medicine and engineering.

This research strives for a better comprehension of the production and operation processes of a charge trapping non-volatile memory devices. A proper analytical approach is the key to manufacture more efficient, stable and cheaper appliances. A careful material characterization can not only explain why the performance of the device is not as good as expected, but also can suggest a suitable solution of the problem.

There are two main targets of this work, first is to describe thermal induced processes occurring in an ultra thin alumina material which is considered to be among the most promising candidates for a blocking oxide replacement in next generation of charge trapping non-volatile memory devices. Second, is to prove that Time-of-Flight Secondary Ion Mass Spectroscopy (ToF-SIMS), despite the current trend of using it only for preliminary qualitative measurements, may provide a lot of detailed information, including quantitative description. Even though it cannot work as a completely independent method after creating suitable models based on other techniques ToF-SIMS can be used to identify and describe unknown samples.

In Chapter 2 I will describe the urgent need for a replacement of silicon dioxide with a suitable high-k material. Starting with famous Moore's law, the observation and forecast which became the ultimate goal of an entire chip industry; I will continue by pointing the reason of a breakdown of silicon

based memory devices and eventually I will introduce the concept of the high k-material, their main advantages and drawbacks.

A proper characterization of the solid state material cannot exclude the concept of defects. I will start with a general definition, followed by the distinction of a several groups of defects. A possible interaction of defects will be further discussed with a strong emphasis on its influence on the diffusion process.

The manufacturing process of the high-k material is usually difficult and elaborated. I will not describe in detail every production stage but rather focus on one of the most important production step: thermal annealing. It is well known that the high temperature processing induces diffusion of materials and therefore I will present a sufficiently detailed summary of the theory of the diffusion process.

In Chapter 3 I will describe basics and setups of production and analytical techniques that were used in the experiment. The main emphasis will be placed on the Time-of-Flight Secondary Ion Mass Spectroscopy, the leading method used in the most of characterizations. I will discuss the complexity, usefulness and possible applications of the method. I will argue that despite many difficulties the quantification of the obtained results is possible. The data evaluation process will be described in detail.

Chapter 4 will be dedicated to the presentation of all thermally induced processes that were successfully characterized, namely crystallization and the resulting compaction and shrinkage, diffusion with a strong indication on its mechanism, segregation, interface formation and surface diffusion. Complementary dielectric measurements will also be shown. All results will be presented in qualitative and quantitative description.

In the last part, Chapter 5, I will summarize achievements of my work and discuss usefulness of ToF-SIMS technique as a leading analytical method.

Chapter 2

Theory

2.1 High-k materials

2.1.1 Moore's law and its limitation

Moore's law is an empirical observation that describes the long-term development of the computing hardware and states that the number of transistors, the fundamental building blocks of all computer chips, that can be placed on an integrated circuit, doubles approximately every two years (see Figure 2.1). It was first described by the Intel co-founder Gordon E. Moore in 1965 [1] with some later revisions about the time of doubling the number of transistors [2]. At the beginning it was rather an observation and forecast. Moore claimed that the trend will follow for at least ten years, but as his law was widely accepted and set as an ultimate goal of the entire chip industry [3] it turned out to be true for almost half a century with a strong probability to continue in the following years.

The constant development of new production techniques allowed this trend to be fulfilled. However the ultimate limits of the law were known and obvious: the fundamental barrier is a size of an atom. This fact was mentioned several times by Moore himself [4], but the vision of breakdown came much earlier, still far from the atomic size. The development of a new generation of chips used advancing production techniques which allowed further downscaling of the transistors, but the material used for a gate dielectric remained the same for decades: silicon dioxide. It became clear that at some point even if the further decrease of the oxide thickness was possible it would disturb the performance of the device. As the thickness of the oxide drops below 2nm the leakage current caused by the tunneling effect increases drastically leading to a waste power consumption and reduced device reliability. The future of silicon based devices is coming to its end.

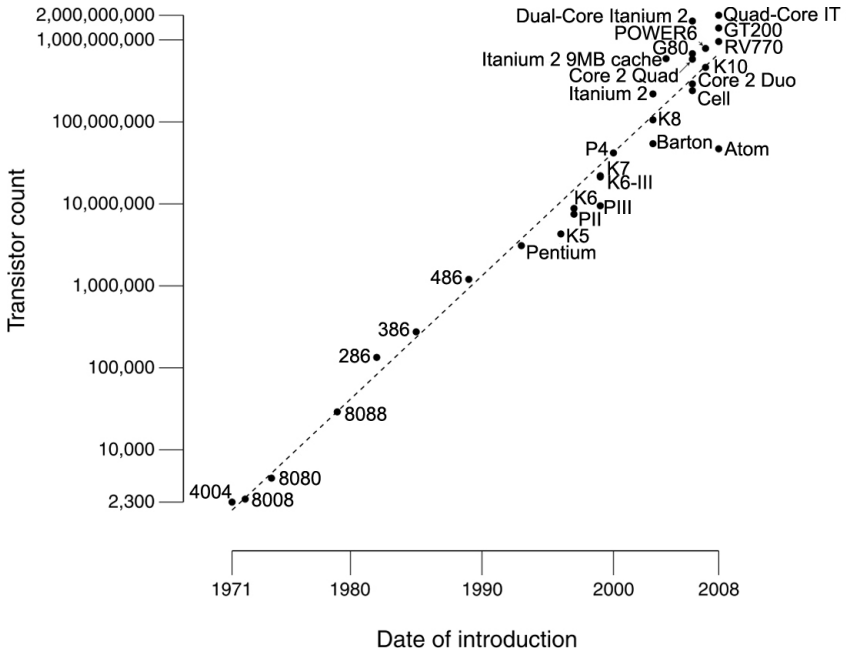

Figure 2.1: Moore's law. Line: CPU transistor count doubling every two years. Dots: generations of processors.

2.1.2 New materials

The gate oxide of a transistor can be modeled by a parallel plate capacitor with a capacitance given by:

$$C = \frac{\kappa \epsilon_0 A}{t} \tag{2.1}$$

where κ is the relative dielectric constant of the material (3.9 for SiO_2), ϵ_0 is the permittivity of free space, A is the capacitor area and t is the thickness of the capacitor oxide.

The increase of the capacitance can be achieved not only by downscaling the oxide thickness, but also by the increase of the relative dielectric constant. It can be done by replacing the silicon dioxide with a material with higher dielectric constant. The colloquial name used for such oxides is high-k materials. Even a thicker layer of such a material may assure higher capacitance with the drastic reduction of the leakage current.

Intensive studies to implement the high-k materials in manufacturing of electronic devices are performed worldwide. Unfortunately this is connected with a complex production process. Silicon dioxide is formed by simple oxidation of a Si substrate. It assures high uniformity and a good quality of

an interface which has a major influence on the performance of the electronic devices. A high-k material that can potentially be used as a replacement of the silicon dioxide as a gate dielectric must fulfill many requirements, not only being able to integrate in manufacturing process, but also should maintain high thermal and chemical stability, mobility of charge carriers and minimize the number of defects which reduce the performance of the device. Another feature that a potential material should have is a relative low production cost. This is very important if the material is to be used in mass production.

Many materials are considered as a potential candidate for a gate oxide replacement [5–15]. Among them there are hafnium dioxide [16–24], hafnium silicate[24–29], zirconium dioxide[30–32], zirconium silicate[25, 26, 33–35] and aluminum oxide[36–40].

2.1.3 Aluminum oxide

From the group of pure metal oxides, alumina is considered to be among the most promising candidates for a suitable replacement of the blocking oxide material in a charge trapping nonvolatile memory devices [36–40]. The increase of the dielectric constant is only moderate (from 3.9 for SiO_2 to 9 for Al_2O_3), but alumina is known to be one of the chemically and thermodynamically most stable materials [41, 42].

2.2 Defects

A perfect crystal exhibits a periodic structure and every atom should be in the correct position at repeating fixed distances, described by the unit cell parameters and thus mass and charge density have the periodicity of the lattice. A perfect crystal, however, does not exist as all crystals have some defects which disturb this periodicity. The name 'defect' can be confusing and considered as something unwelcome, yet in many cases defects are desired and intentionally introduced as they contribute and may enhance the properties of the material. For example adding alloying elements to a metal may increase its tensile strength, or doping semiconductors to enhance its electrical properties can be considered as a way of introducing crystal defects.

A good comprehension of the diffusion process requires additional knowledge about the microstructure of the solid materials. As it will be presented in the following sections the diffusion in a crystalline phase is mostly related to the various types of defects in the lattice and therefore it is essential to acquire at least the basic comprehension about defects in the solid state

materials before the detailed considerations about the diffusion process may begin. The concept of so-called point defects was introduced in 1926 by Yakov Frenkel [43] and further developed by Walter Schottky in 1930s [44]. Nowadays, the theoretical and experimental knowledge about the defects is enormous. However, it is not the scope of this work to present the detailed information about the thermodynamic reasons, formation processes, stability, equilibrium concentration, behavior and other topics related to defects. They are, however, covered in numerous literature [45–80] while in this work only a general information about different types of defects will be presented. The following sections will serve as a background for understanding diffusion mechanisms, barriers, traps, segregation and other defects-dependent diffusion-related processes.

Defects can be classified into four main groups depending on the number of dimensions that the defect is extended over.

2.2.1 Point defects

As the name suggests those defects are not extended in space in any dimension but rather localized at or around a single lattice point. However, there is no strict definition of the size of the point defect, but typically it is limited to a few extra or missing atoms occurring at one lattice point or in a very close proximity. Furthermore, point defects are usually not permanently fixed at a specific position. They have the ability to migrate across the sample, especially in elevated temperatures. The detailed information about the mobility of defects can be found in the following sections. Several variations of point defects can be considered and most of them are presented in Figure 2.2.

- Vacancy defect occurs when an atom is missing in the lattice site which would be occupied in a perfect crystal (see Figure 2.2.1.). Usually a collapse of the neighboring atoms is not observed due to the stability of the crystal structure. Vacancies are common, especially at high temperatures when atoms are frequently and randomly changing their positions leaving behind empty lattice sites. A vacancy is often denoted as a Schottky defect.

- Interstitial defect occurs when an atom occupies an interstitial void in the crystal structure i.e. a site where no atom can be found in a perfect crystal. An extra atom can be the same or smaller than atoms found in the lattice giving rise to the self interstitial (see Figure 2.2.2.) and the impurity interstitial defects (see Figure 2.2.3.), respectively. The concentration of the self interstitial defects is usually low specially for the tightly packed lattice as the extra atom distorts and highly stresses

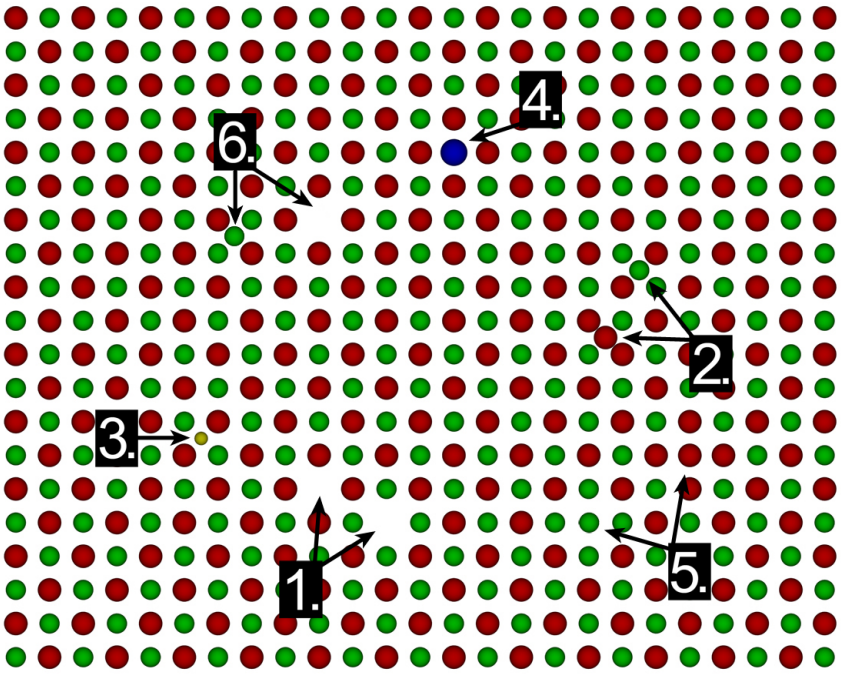

Figure 2.2: Schematic illustration of point defects in a compound solid consisting two different types of atoms in the lattice of a perfect crystal (red and green orbs) 1. Vacancy defects 2. Self interstitial defects 3. Impurity interstitial defect 4. Substitutional defect 5. Antisite defects 6. Frenkel defect

the structure. Atoms which form the impurity interstitial defects are usually much smaller than the atoms in the bulk matrix and fit well into the open spaces of the lattice structure without causing stress. Therefore the abundance of the impurity interstitial defects is usually much higher than the self interstitial defects and are often introduced intentionally to change the properties of a material. For example carbon atoms, with a radius of $0.071nm$, are added to iron to make steel. They fit nicely in the open spaces between the larger ($0.124nm$) host atoms.

- Substitutional defect often denoted as substitutional impurity occurs when an atom of a different type than the bulk atoms replaces one of the atoms in the lattice (see Figure 2.2.4.). Usually impurity atoms are similar in size to the bulk atoms (within approximately 15%). Those defects are very common as materials are never 100% pure. Similarly to

the impurity interstitial defects they are often introduced intentionally to change the properties of a material. Brass can be a good example, where zinc atoms with a radius of $0.133nm$ have replaced some of the copper atoms, which have a radius of $0.128nm$.

- Antisite defect occurs only in an ordered material with at least two different types of atoms in the lattice. An antisite defect is formed when an atom is on a site which is occupied in a perfect crystal, but it is not the correct type (see Figure 2.2.5.). As an example the body centered cubic lattice with two different types of atoms (e.g. cesium chloride crystal structure) can be considered. If type A atoms occupy the corners of a unit cell, and type B atoms are found in the center the antisite defect is formed when the unit cell has an A atom at its center or a B atom at one of its corners.

- Topological defect is formed when the chemical bonding of atoms is the same as in a perfect crystal, but the topology differs from the surroundings. An example is the Stone Wales defect in nanotubes, which consists of two adjacent 5-member and two 7-member carbon rings while all atoms should be aligned in rings containing six atoms.

- Complex defects are formed when two or more simple defects are joined and bound together. They cannot be treated separately as they influence one another. For example a nearby pair of a vacancy and an interstitial defect is often denoted as a Frenkel defect (see Figure 2.2.6.). In this case the vacancy cannot be taken by some other atom because it is prevented by nearby interstitial atom, which in turn cannot move easily to another void because it is energetically unfavorable as it will cause significant stress. Other types of combinations are also possible: divacancies; two small interstitial atoms may effectively share the same void or even be additionally bound to a nearby vacancy.

So far only defects in crystal structures have been considered, but amorphous solids may contain them as well. They are essentially harder to define as the amorphous materials do not have a periodic structure. The most common type of a defect in a amorphous material is a dangling bond which is formed when an immobilized atom has too few bonding partners to satisfy its valences and possesses unpaired electrons. The dangling bonds are usually formed at the surface of the sample, but can be found in the bulk as well when some atoms are missing (e.g. non stoichiometric relation between silicon and oxygen in amorphous silica). This concept is somewhat similar to

the vacancy defect in crystalline structures and some consequences of both types of defects can be often described in the same manner.

The point defects are usually not pinned at their positions, but rather propagate around the sample, especially for elevated temperatures. For example small interstitial impurities can relatively easily change the void or the vacancy can be taken by a neighboring atom leaving an empty space and thus effectively vacancies move in opposite directions than atoms. The mobility of point defects plays a significant role in many processes occurring in the sample, particularly the diffusion which will be discussed in the following sections.

2.2.2 Linear Defects - Dislocations

Dislocations are linear defects around which the periodic distribution of atoms is disturbed. They are usually generated as a result of stress applied to the sample. Furthermore, dislocations have an ability to move in the sample if the stress is still present. The knowledge about the motion of dislocations is required to explain many properties of some materials, for example the plastic deformation of a metal. However, the mechanism of motion of dislocation is significantly different than it was for point defects. The simultaneous movement of line arranged defects would require a considerable amount of energy, whereas gradual motion allows propagation of dislocations even at lower energies.

Two basic types of dislocations can be distinguished and the main difference is that a dislocation line moves parallel or perpendicular to the applied stress for the edge and screw dislocation, respectively. However, most dislocations are actually combinations of both types.

An edge defect can be considered as an extra half-plane of atoms in a lattice. Figure 2.3.1. presents a single layer of atoms with an edge dislocation. As it can be seen the disturbance of the positions of atoms is located only in the immediate vicinity of the top of the unfinished atomic line. However, as the same situation holds for layers of atoms located above and below, it can be understood that the defective points lie along a line which runs on the top of the extra half-plane.

If the stress is applied to the material the dislocation will move. As shown in Figure 2.3.1. the top part of the crystal moves gradually, slipping one plane at a time. The movement of the dislocation across the plane eventually causes the top part of the crystal to move with respect to the bottom half. This movement does not require breaking all the bonds across the middle plane simultaneously. To the contrary, only a small quantity of the bonds are broken during a single slip and therefore the deformation of

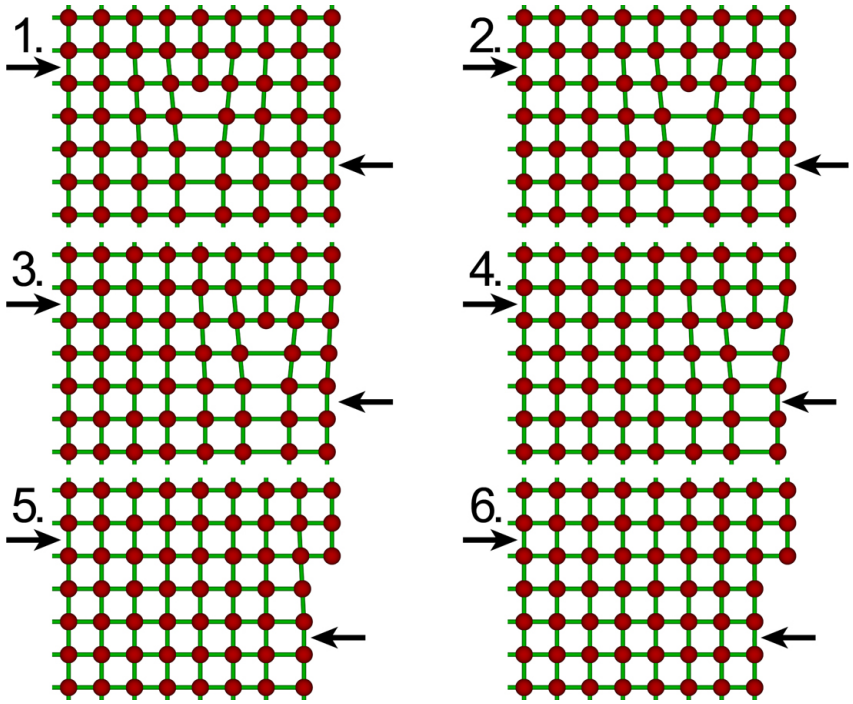

Figure 2.3: The edge dislocation as an extra half-plane of atoms in a lattice. If stress is applied (black arrows) the dislocation will propagate in the sample slipping one plane at a time, eventually reaching the edge of the sample.

the material is possible even if a relatively small force is applied (smaller than needed to deform a perfect crystal).

The screw dislocation (Figure 2.4) is different in this respect that the dislocation line propagates perpendicular to the applied stress. As it was with the edge dislocation, the movement of the screw dislocation requires much smaller force than would be required to break all bonds across the middle plane simultaneously.

2.2.3 Planar defects

Planar defects are commonly defined as interfaces between homogeneous regions of the material. Unlike point and linear defects, the mobility of planar defects is usually limited as it would require a significant amount of energy to move considerable quantity of atoms forming those defects. Migration of planar defect can only occur if the elevated pressure and temperature are present in the sample. Several types of the planar defects can be distinguished:

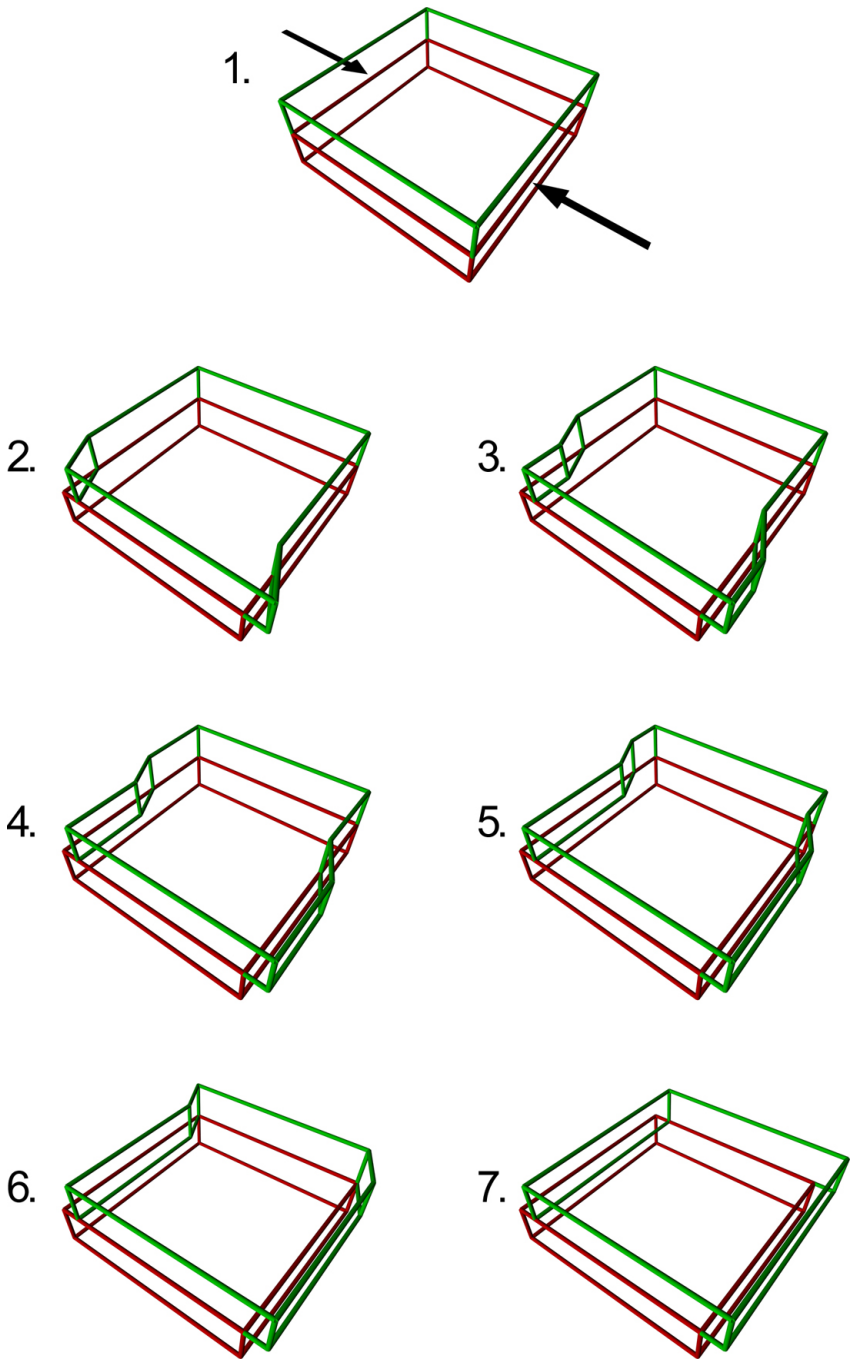

Figure 2.4: The screw dislocation and its movement along the sample as a result of applied stress. The black arrows indicating the direction of the stress were removed in most of the diagrams for a better visibility.

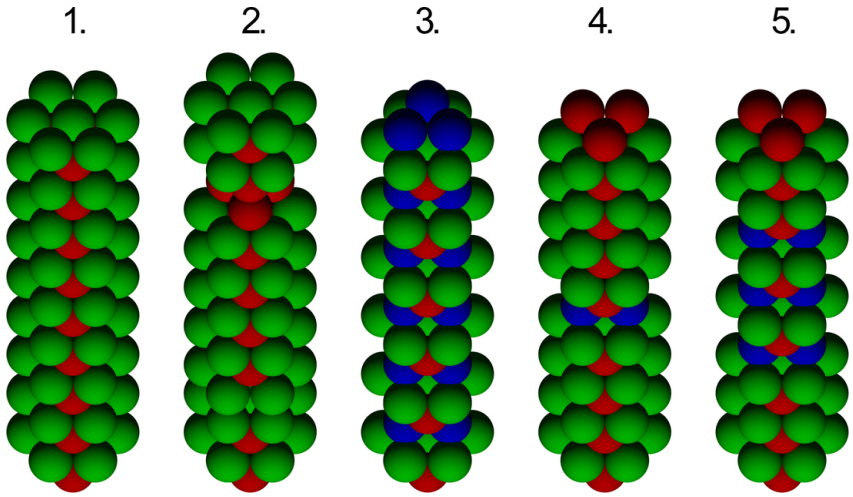

Figure 2.5: Several types of planar defects: 1. A perfect hexagonal close-packed (hcp) structure. 2. An hcp with both types of anti-phase boundaries. 3. A perfect face centered cubic (fcc) structure. 4. Stacking fault of hcp structure with additional layer of fcc structure. 5. A twin region: two hcp structures surrounding fcc structure.

- An anti-phase boundary occurs commonly in ordered compounds. The crystallographic direction is not affected, but the ordering of individual planes is altered. As an example the hexagonal close packed (hcp) structure (Figure 2.5.1.) can be considered. A perfect hcp structure consists of alternating layers A and B with different atom distribution (i.e. ABABABABAB stacking). An anti-phase will be crated if two layers of the same type will be placed next to each other (i.e. ABAB**AA**BABA or ABABA**BB**ABAB stacking). Figure 2.5.2. presents both possible anti-phase boundaries for hcp structure.

- A stacking fault can be understood as a disruption of the long-range stacking sequence over a few atomic spacings (usually one or two). This kind of defect appears in many crystal structures, but can be easily shown for the close packed structures: the face centered cubic (fcc) structure (Figure 2.5.3.) has the same arrangement of the first two layers as the hcp structure. However, the third layer is diverse. In the hcp, as already mentioned, the atom arrangement is the same as in the first layer, whereas it is different for the fcc: atoms are not placed directly above those in the first layer but arranged differently preserving, however, a close-packed structure. The hcp structure with

the stacking fault occurs when the perfect arrangement is not preserved, but a single layer characteristic for the fcc structure (C) can be found in the sample (e.g. ABABAB**C**ABABAB). Figure 2.5.4. presents a stacking fault for the hcp structure.

- A twin region is similar to a stacking fault, but is extended over more layers i.e. it occurs when a stacking fault does not correct itself immediately but continues over some number of layers. The name of the defect originated from the fact that a structure can be considered as consisting two different phases (e.g. hcp and fcc) separated by a set of twin stacking faults. For example if an hcp structure is subjected to have a twin region it may results in ABABAB**CABCABC**ABABA stacking (see Figure 2.5.4.)

- A grain boundary is a significantly different type of defect as it concerns polycrystalline materials while all previous examples applied to single crystals. However, most solids are composed of a number of crystallites, usually called grains. Each of them can be considered as a single crystal with the size ranging from nanometers to millimeters, depending on the material and the growth process. Furthermore, the orientation of each grain is usually different with respect to neighboring grains. Figure 2.6 presents a schematic illustration of a polycrystalline material with grains differing in size and orientation.

  Grains are usually formed due to the non-uniform growth of a crystal with many crystallization centers, each resulting in different crystal orientation. At the interface between two grains the atomic mismatch can be observed and the properties of the material along this interface are significantly different from the bulk material, e.g. weak bonding makes them preferred sites for the onset of corrosion. Furthermore, the presence of the grain boundaries tends to decrease the thermal and electrical conductivity of the material and limit the lengths and motions of dislocations through a material and thus, the strength of the material can be improved by reducing the crystallite size. The most common way to control the grain size is to adjust properly the cooling rate of the material after the thermal treatment. Generally, smaller grains will be produced during rapid cooling, whereas large grains will be formed for slower process.

  Tilt and twist boundaries (see Figure 2.7) are two basic types of grain boundary defects. However, similarly to the dislocations, most grain boundaries are actually combinations of both types. It is also common to distinguish low and high angle boundaries [81–84] as their properties,

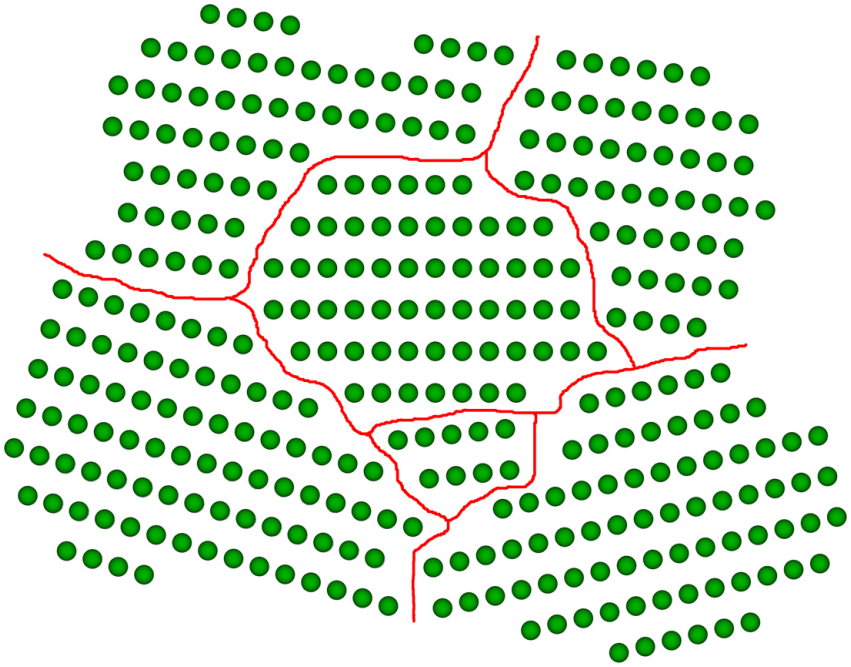

Figure 2.6: Polycrystal consisting of crystallites with different sizes and orientations. The distance between grains is exaggerated to visualize the concept of grain boundaries.

like energy distribution and mobility, differ significantly. However, this topic has a limited importance in this work and therefore it will not be discussed further.

- External surface - although it may seem not proper to consider the surfaces of the sample as defects, but it can be easily justified as they consist of atoms extended in two dimensions with properties significantly different from the bulk atoms of a perfect crystal.

2.2.4 Bulk defects

Bulk defects are extended in all directions and with much bigger scale than the rest of the defects described in this section. As it can be easily concluded, their mobility is drastically reduced and usually they do not move in the sample. Two basic types can be distinguished:

- Voids are defined as regions where a lot of atoms are missing from the lattice and can be considered as clusters of vacancies. The formation of

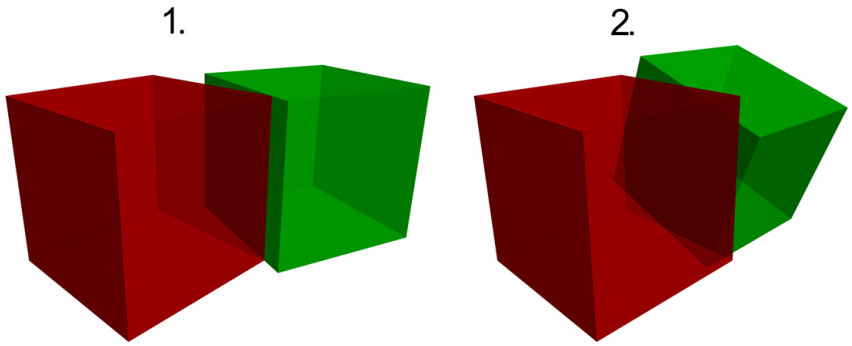

Figure 2.7: Formation of grain boundaries between two ideal cubic grains: a tilt boundary (1.) and a twist boundary (2.)

voids, however, varies: they may occur due to trapped air bubbles or as a result of shrinkage of a material during solidification process and are commonly called porosity and cavitation, respectively.

- Precipitate are regions where a large quantity of impurity atoms form a cluster with a different phase.

2.2.5 Defect interaction

It has been indicated several times that defects can interact with one another forming complex defects, or changing the respective properties, however, the concept of defect interaction has not been discussed in details. Yet, it is very important to acknowledge some processes that undergo between defects in order to understand properly the following sections concerning the diffusion rate. The comprehensive knowledge about the defect interaction is available in the literature [85–90], whereas this section will be limited only to a brief introduction of a few aspects which have the strongest relevance to the diffusion process. However, it is rather difficult to define strictly each type of interactions as they tend to occur simultaneously and some of them are the consequences of the others and therefore the following examples should be treated as a general description of defect interaction. Schematic illustration of defect interaction can be found in Figure 2.8

- Clustering - defects have an ability to bind together forming more complex defects with properties significantly different from that of individual parts. For example divacancies allow an easier atom exchange than a single vacancy. On the other hand the mobility of the bound interstitial impurities is strongly reduced. In a similar way, when a large

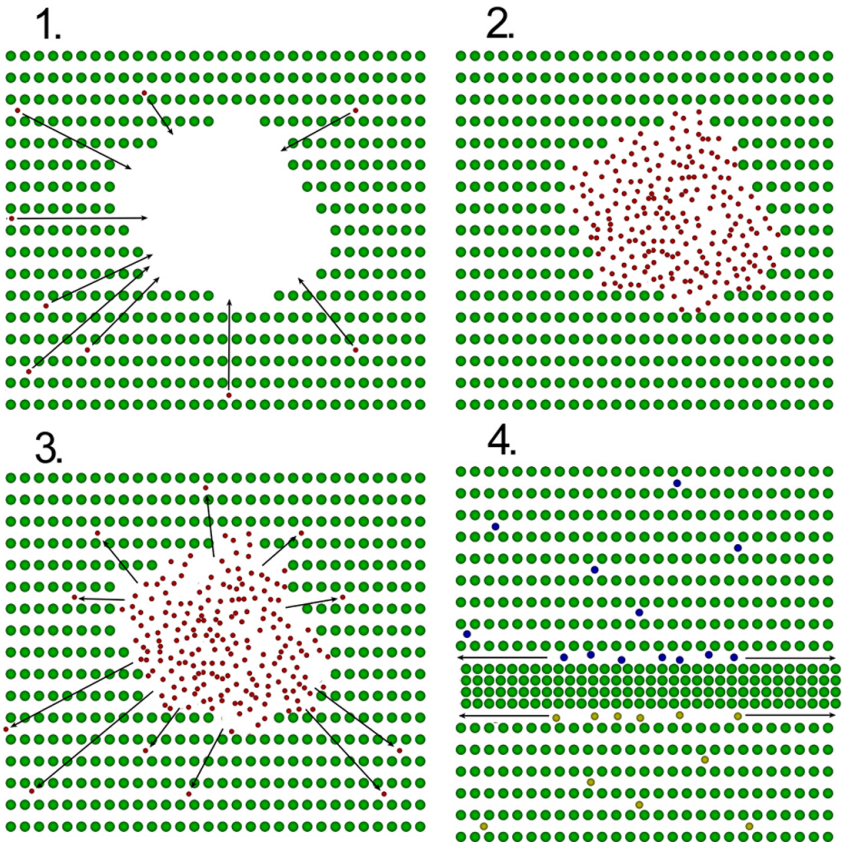

Figure 2.8: A few examples of defect interaction: 1. Small interstitial impurities reach the void in the material and start to form a precipitate. 2. At low temperatures the diffusion of impurities along the sample is energetically unfavorable and therefore impurity atoms are bound inside a precipitate. 3. At elevated temperatures bonds in the precipitate break and the bulk defect can be considered as a source of impurities which can diffuse along the sample. 4. Twin region with higher packing efficiency prevents the penetration of interstitial impurities. However, larger spacing due to the mismatch between the phases enhances the diffusion along the defect plane.

quantity of vacancies or impurities starts to agglomerate (forming voids and precipitates, respectively) they will not be able to move around the sample freely.

- Disintegration - a process opposite to the clustering. Some complex defects may decompose giving rise to several more basic defects. For example at elevated temperatures the bond between atoms in precipitate may break and many single-atom impurities will be introduced and free to propagate across the sample. In this manner the precipitate may become a source of diffusing impurities.

- Immobilization - it is very often that one defect may slow down or even prevent the motion of the other defect. Impurities and grain boundaries are well known for preventing the movement of dislocations. Planar and bulk defects can form regions impenetrable for other defects forming the diffusion barriers.

- Enhancement of the mobility - on the other hand some defects may actually promote the faster movement of defects. Furthermore, usually this property is anisotropic. For example along dislocations and grain boundaries the spacing between atoms is larger than in the bulk material. It allows easier diffusion of impurities but only along those defects and thus so called high diffusivity paths are created.

2.3 Diffusion in solids

Diffusion is a time depending process in which the material is transported due to the atomic or molecular thermal motions. It occurs in matter regardless the state, but the kinetics and dynamics of the diffusion in gases, liquids and solids differs significantly and therefore each of them should be treated separately. The diffusion in solids is the central aspect of this work and therefore the diffusion in fluids will not be discussed.

A lot of technologically important processes are based on the diffusion phenomenon. Among many one can mention doping of semiconductors, oxidation of metals, hardening of steel, sintering or formation of solid-state compounds. To control those processes precisely the deep knowledge about the kinetics and dynamics of the diffusion is required. An intensive study of the solid state diffusion has been performed and described worldwide for more than half a century [91–117].

As it was already said, the diffusion process differs significantly for different states of matter. However, even if only the solid state diffusion is

considered, there are fundamental differences in the diffusion mechanism depending on the phase of the material. For example for crystalline phase the diffusion is mostly related to the various types of defects occurring in the lattice e.g. vacancies, interstitials, dislocations, free surfaces, grain or phase boundaries etc. The mobility of atoms along those defects is typically much higher then in the lattice and therefore so called high-diffusivity paths play the most significant role in the whole diffusion process in the solid. However, this concept cannot be applied to disordered materials like glasses. Typically, the diffusion in disordered materials is not localized as it is an often case in crystalline material. Furthermore, a particle moving in the ordered state usually always meets the same energy barrier, whereas in amorphous materials the broad distribution of the energy barriers is expected. Therefore the effective mobility of the particle is not determined by the average energy barrier height but rather by the highest barrier that has to be overcome. Consequently, the diffusion in amorphous material is often subject to size dependency.

As it was clearly shown, the diffusion is a very complex process. There are a few general rules to describe it, but further investigations should be performed separately for each material type. Since the semiconductors are the key material in this work, this section will be limited to summarize the essential knowledge about the diffusion in semiconductors only. Furthermore, it has to be noted that the rate of the diffusion in solids is very slow when compared to fluids and therefore it has to be taken into account that in most cases the appreciable influence of the diffusion will only take place at elevated temperatures. Consequently, other high temperature related processes (e.g. crystallization, oxidation or even melting) have to be taken into consideration as well.

2.3.1 Fick's laws of diffusion

The general equations that quantitatively describe the diffusion process are called the Fick's laws of diffusion and were introduced by a German scientist Adolf Fick in 1855 [118]. Observations of salt-water system undergoing diffusion led him to the conclusion that the flux of diffusing material goes from the region of higher concentration towards the region with lower concentration, being proportional to the concentration gradient. Almost half a century before (1807) a French mathematician and physicist Jean Baptiste Joseph Fourier introduced analogous equations describing the heat flow and its relation to the temperature gradient [119]. Although both theories were purely empirical their importance cannot be underestimated. They provide the general rules governing diffusion and heat transport processes, respec-

tively, and the further development and understanding of those phenomena were not only based on them, but also confirmed their validity.

It is very important to emphasize that since the Fick's laws of diffusion are very general each specific solution may be very complex and should be treated separately. The procedure of solving the diffusion equation is significantly different depending on the anisotropic properties of the material or even on the type of coordinate systems (Cartesian, cylindrical, spherical) that is used to describe the particular case. In this work the silicon out-diffusion from the substrate through the thin films was investigated and therefore only one dimensional solutions of the Fick's equation will be considered as it fits best for this particular experiment. Solutions of diffusion equations for various coordinate systems can be found in most books concerning the diffusion process, while the detailed knowledge about the diffusion in anisotropic materials was covered in many books concerning nonlinear partial differential equations [120–124].

Fick's First Law

The relation between diffusion flux and the concentration gradient introduced by Fick follows:

$$J = -D\frac{\partial C}{\partial x} \tag{2.2}$$

where J is the diffusion flux in dimensions of [(number of atoms) m^{-2} s^{-1}], D is the diffusion coefficient in dimensions of [m^2 s^{-1}], C is the atomic density in dimensions of [(number of atoms) m^{-3}], and x is the position [m]. This equation represents the simplest form of the Fick's first law of the diffusion. However, some complexities may arise from the fact that the diffusion coefficient is not necessarily a constant value. As it was suggested before it may be altered by the anisotropic properties of the material but also by its concentration dependency.

Equation of continuity

For a simple diffusion process it can be assumed the the number of diffusing particles is conserved. This implies that no chemical reaction of diffusing particles, nor exchanges with sources, nor sinks are present in the system (more complex situations will be covered in the following sections). Let us consider a test distance Δx at some particular point of the material with the flux J across this distance. If the sum of the inflow and outflow of the material across the distance Δx is not balanced a net accumulation or loss must occur. It can be expressed with a simple formula:

$$\frac{\partial C}{\partial t} = -\frac{\partial J}{\partial x} \tag{2.3}$$

This equation is known as the equation of continuity.

Fick's Second Law

The Fick's First Law (eq. 2.2) and the Equation of continuity (2.3) can be combined and the rate at which the concentration changes in diffusion system can be derived:

$$\frac{\partial C}{\partial t} = \frac{\partial}{\partial x}(D\frac{\partial C}{\partial x}) \tag{2.4}$$

Which is denoted as the Fick's Second Law of the Diffusion, or diffusion equation. This is a second order partial differential equation. In case of concentration dependent D the equation is non-linear and usually cannot be solved analytically. As it was already mentioned, this situation will not be covered in this work. However, if the diffusion coefficient is constant (i.e. does not depend on the location nor concentration) the order of the differentiating can be exchanged:

$$\frac{\partial}{\partial x}(D\frac{\partial C}{\partial x}) = D\frac{\partial^2 C}{\partial x^2} \tag{2.5}$$

And thus one obtains the simplified version of the Fick's Second Law of the Diffusion, which is often denoted as linear diffusion equation:

$$\frac{\partial C}{\partial t} = D\frac{\partial^2 C}{\partial x^2} \tag{2.6}$$

which describes the change of a concentration with time.

2.3.2 Solutions to the diffusion equations

To describe the diffusion process quantitatively the solution (i.e. concentration as a function of time and position) to the Equation 2.6 has to be found and the diffusion coefficient has to be determined. Despite some assumptions (e.g. D is constant) this equation is still very general and there is no universal solution as the system may vary in many aspects like size, type of the source, initial and boundary conditions. It is virtually impossible to show every solution or even present the procedure of solving the diffusion equation for most experiments and therefore this section will again be significantly reduced. A few very simple solutions will be shown to present a general procedure followed by more complicated situations, which fit best for this particular experiment. A more comprehensive description of the mathematical solutions for the diffusion equations can be found in numerous textbooks (e.g. [125–128]). As the diffusion problem was already compared to the heat transfer, it is also very helpful to study solutions of heat equations

(e.g. [129]). In most cases by a simple replacement of the temperature with the concentration and the corresponding thermal with mass diffusivity, one can obtain solutions for many particular diffusivity problems. Furthermore, some of the diffusion equations cannot be solved analytically and therefore numerical methods have to be employed. The description of this procedure can be found in literature as well [101, 126–128, 130].

Instantaneous planar source

The first important step is to consider the diffusion from a plane source into the infinite system. At the beginning of the experiment ($t = 0$) the concentration is zero everywhere except for the point where the plane is located ($x = 0$) where it is infinite. It can be expressed as:

$$C(x, 0) = M\delta(x = 0) \tag{2.7}$$

where M denotes areal density of diffusing particles and $\delta(x = 0)$ the Dirac delta function. For $t > 0$ particles spread into the system and a straightforward integration of Equation 2.6 shows:

$$C(x, t) = At^{-\frac{1}{2}} e^{-\frac{x^2}{4Dt}} \tag{2.8}$$

In an infinite medium the material is not consumed during the diffusion and therefore it is possible to evaluate the parameter A as follows:

$$M = \int_{-\infty}^{\infty} C(x, t)dx = \int_{-\infty}^{\infty} At^{-\frac{1}{2}} e^{-\frac{x^2}{4Dt}} dx \tag{2.9}$$

Changing the variables:

$$\begin{aligned} \eta^2 &= \frac{x^2}{4Dt} \\ 2\eta d\eta &= \frac{2x}{4Dt} dx \\ \frac{x}{\sqrt{4Dt}} d\eta &= \frac{x}{4Dt} dx \\ dx &= \sqrt{4Dt} d\eta \end{aligned} \tag{2.10}$$

And substituting to the Equation 2.9 one can obtain:

$$M = At^{-\frac{1}{2}} \int_{-\infty}^{\infty} e^{-\eta^2} \sqrt{4Dt} d\eta = A\sqrt{4D} \int_{-\infty}^{\infty} e^{-\eta^2} d\eta = A\sqrt{4\pi D} \tag{2.11}$$

And therefore

$$A = \frac{M}{\sqrt{4\pi D}} \tag{2.12}$$

It can be substituted to the Equation 2.8 and the so called Gaussian solution can be formulated:

$$C(x,t) = \frac{M}{\sqrt{4\pi Dt}} e^{-\frac{x^2}{4Dt}} \tag{2.13}$$

In this solution half of the material diffuses in the positive direction and the other half in the negative one. In reality this situation is very rare as it describes some kind of a sandwich geometry in which the planar source of the diffusing particles is placed in between two semi-infinite regions occupying negative and positive half-spaces. However, this solution can be very useful when taken into account that it is symmetrical about $x = 0$ which means that it is also valid for a semi infinite situation where the diffusion occurs only in one direction i.e. when the thin film of diffusing particles is deposited on the surface of a sample with considerable larger thickness. This simple solution proved to be very useful in description of many experiments, for example Si doping by diffusion. In this situation the solution of diffusion equation differ by a factor of 2 with Equation 2.13 and reads:

$$C(x,t) = \frac{M}{\sqrt{\pi Dt}} e^{-\frac{x^2}{4Dt}} \tag{2.14}$$

The quantity $L_d = \sqrt{4Dt}$ is called a diffusion length and a straightforward calculation based on Equation 2.13 or 2.14 may prove that the diffusion length is an average distance that particles propagated into the sample. The concept of the diffusion length appears often in other diffusion-related problems and provides useful information: the infinite system assumption is only valid if the sample extent L is much bigger than the diffusion length ($L \gg L_d$). Otherwise this model cannot be applied and another description should be found. Equation 2.14 is illustrated on Figure 2.9 for different diffusion lengths and its application is discussed for specific sample size L.

Instantaneous planar source approximation can be used to describe the experiment providing the thickness of the sample is much larger than both the diffusion length and the deposited thin film. The solution is very useful and frequently used but still limited. Hence other models have to be exploited as well.

Volume source

The setup of many experiments is designed is such a way that diffusant is spread evenly over some finite region rather that concentrated on a single plane. Let us consider the most general situation consisting a semi infinite volume source with a constant concentration C_0 that extends from $-\infty$ to $x = 0$ at time $t = 0$. This problem is often denoted as a diffusion couple,

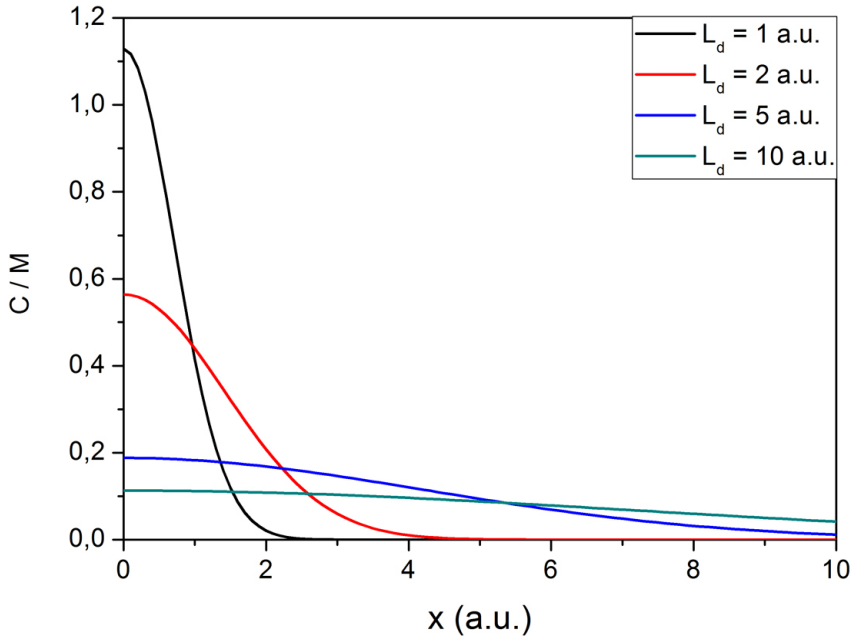

Figure 2.9: Semi-infinite Gaussian solution of the diffusion equation for a sample size $L = 10a.u.$ and varying diffusion length L_d. The semi-infinite assumption is valid for $L_d = 1a.u.$ and $L_d = 2a.u.$, questionable for $L_d = 5a.u.$ and not applicable for $L_d = 10a.u.$

where two semi-infinite bars with different compositions are joined and permitted to mix. The volume source of the diffusant can be considered as a stack of plane sources with thickness $d\xi$, each of them containing an areal density $C_0 d\xi_i$ of material located at ξ.

As it was assumed that the diffusion process is linear (diffusion coefficient does not depend on the location nor concentration), the principle of superposition can be used to solve this problem. According to Equation 2.13 the distribution of the material coming from the plane at $x = \xi$ equals to:

$$dC_i(x,t) = \frac{C_0 d\xi_i}{\sqrt{4\pi Dt}} e^{-\frac{(x-\xi_i)^2}{4Dt}} \tag{2.15}$$

The superposition of each individual response from all planes can be expressed as an integral:

$$C(x,t) = \int_{-\infty}^{0} dC_i(x,t) = \int_{-\infty}^{0} \frac{C_0}{\sqrt{4\pi Dt}} e^{-\frac{(x-\xi)^2}{4Dt}} d\xi \tag{2.16}$$

By changing the variables and limits of integration by:

$$\begin{aligned} \frac{x-\xi}{\sqrt{4Dt}} &= \eta \\ d\xi &= -\sqrt{4Dt}d\eta \\ \xi = 0 \rightarrow \eta &= \frac{x}{\sqrt{4Dt}} \\ \xi = -\infty \rightarrow \eta &= \infty \end{aligned} \tag{2.17}$$

One can obtain:

$$\begin{aligned} C(x,t) = -\frac{C_0}{\sqrt{\pi}}\int_{\infty}^{\frac{x}{\sqrt{4Dt}}} e^{-\eta^2}d\eta = -\frac{C_0}{\sqrt{\pi}}(\int_{\infty}^{0} e^{-\eta^2}d\eta - \int_{\frac{x}{\sqrt{4Dt}}}^{0} e^{-\eta^2}d\eta) = \\ = \frac{C_0}{\sqrt{\pi}}(\int_{0}^{\infty} e^{-\eta^2}d\eta - \int_{0}^{\frac{x}{\sqrt{4Dt}}} e^{-\eta^2}d\eta) = \frac{C_0}{\sqrt{\pi}}[\frac{\sqrt{\pi}}{2} - \frac{\sqrt{\pi}}{2}erf(\frac{x}{\sqrt{4Dt}})] = \\ = \frac{C_0}{2}[1 - erf(\frac{x}{\sqrt{4Dt}})] \end{aligned} \tag{2.18}$$

where

$$erf(x) = \frac{2}{\sqrt{\pi}}\int_{0}^{x} e^{-\eta^2}d\eta \tag{2.19}$$

is the definition of the error function. One can also introduce the definition of the error function complement:

$$erfc(x) = 1 - erf(x) \tag{2.20}$$

and thus obtain a so-called Grube-Jedele solution:

$$C(x,t) = \frac{C_0}{2}erfc(\frac{x}{\sqrt{4Dt}}) \tag{2.21}$$

Just like in the previous case the diffusion length $L_d = \sqrt{4Dt}$ is an average distance that particles propagated into the sample. To successfully use the Grube-Jedele solution the system has to fulfill following requirement: the size of both bars, which can be called the source (L_s) and the acceptor (L_a) of diffusant must be much bigger than the diffusion length. Equation 2.21 is illustrated on Figure 2.10 for different diffusion lengths and its application is discussed for specific bars size L_s and L_a.

The Grube-Jedele solution describes the situation where the extent of the volume source is semi-infinite i.e. $L_s \gg L_d$. However, if the size of volume source is limited, one can use the same procedure to calculate adequate solution. Let us consider the simplest case: a slab confined between $-h < x < h$

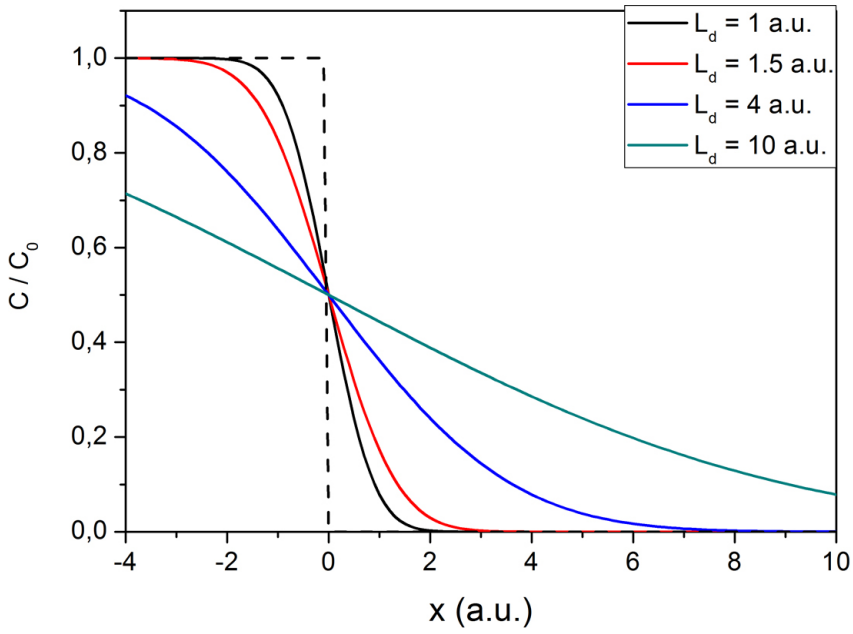

Figure 2.10: The Grube-Jedele solution of the diffusion equation for a size of source bar $L_s = 4a.u.$ $(-4 \leq x \leq 0)$ and acceptor bar $L_a = 10a.u.$ $(0 < x \leq 10)$ and varying diffusion length L_d. Dashed line shows the initial distribution of diffusant. The semi-infinite assumption is valid for $L_d = 1a.u.$ and $L_d = 1.5a.u.$. For $L_d = 4a.u.$ the requirement $L_a \gg L_d$ is met, but $L_s \gg L_d$ is not. For $L_d = 10a.u.$ none of the requirements is fulfilled. In the last two cases the Grube-Jedele solution cannot be applied.

with a uniform initial concentration C_0. Once again, the volume source can be treated as a stack of plane sources and the concentration of diffusant along the x-axis is given by the superposition:

$$C(x,t) = \int_{-h}^{h} \frac{C_0}{\sqrt{4\pi Dt}} e^{-\frac{(x-\xi)^2}{4Dt}} d\xi \tag{2.22}$$

Performing similar calculation, the final solution expressed with error functions can be derived:

$$C(x,t) = \frac{1}{2} C_0 [erf(\frac{h-x}{\sqrt{4Dt}}) + erf(\frac{h+x}{\sqrt{4Dt}})] \tag{2.23}$$

Figure 2.11 illustrate the 'slab diffusion' case for different diffusion lengths.

Similar to the Equation 2.13, the solution is symmetrical about $x = 0$ and describes the propagation of the material in both directions. In case

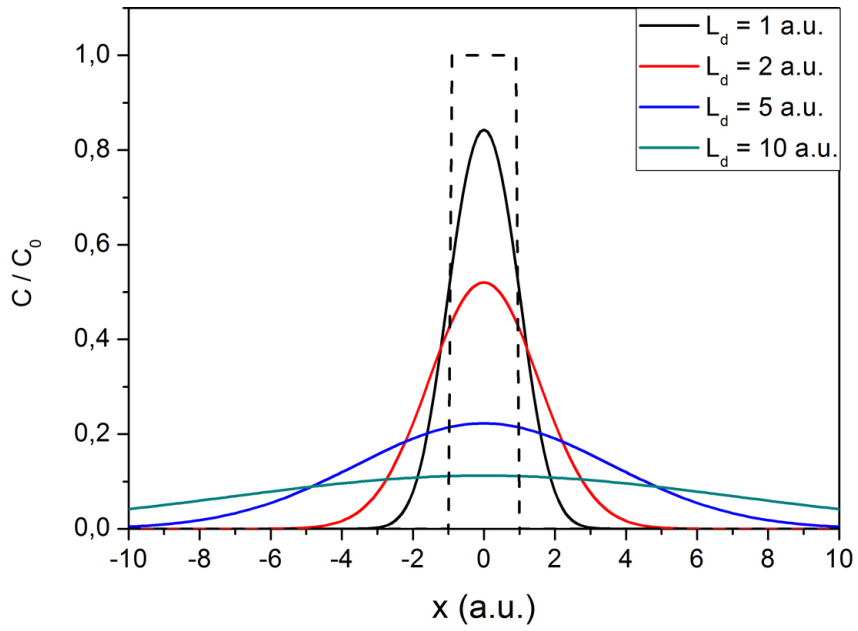

Figure 2.11: Diffusion from slab with a width of $2h$ for varying diffusion length L_d. Dashed line shows the initial distribution of diffusant. The validity of the semi-infinite assumption is similar to Gaussian solution.

of the one direction diffusion (i.e. diffusant initially concentrated in volume with limited thickness propagating into semi-infinite region) a superposition principle should be applied resulting in an additional factor 2 in the Equation 2.23.

Constant surface concentration

In previous models the total amount of diffusing material was kept constant and its distribution was well described by the initial conditions. However, many experiments are designed in the way that an increasing amount of diffusing particles is incorporated into the sample. To provide a uniform diffusion process the experiments are often designed with a constant concentration of diffusant at the surface of the sample (e.g. carburisation and nitridation of metals).

In this situation the solution of the diffusion equation can be very easily derived from the Grube-Jedele solution. A straightforward calculation based on Equation 2.21 leads to the conclusion that the concentration at $x = 0$ is constant and equal $\frac{C_0}{2}$ for $t > 0$. This property is clearly visible on Figure 2.10. Therefore if we assume that the surface of a semi-infinite sample is

located at $x = 0$ and the concentration of diffusing particles is kept constant and equal to $C_s = \frac{C_0}{2}$, the solution can be directly derived as:

$$C(x,t) = C_s erfc(\frac{x}{\sqrt{4Dt}}) \tag{2.24}$$

However, it is essential to emphasize that the similarity of the mathematical formula cannot lead to the conclusion that this is the same solution. In the Grube-Jedele solution the total amount of diffusing material was constant while in this case it is increasing with time and the amount of material which diffuses into the sample per unit area in time can be calculated as follow:

$$M(t) = \int_0^\infty C_s erfc(\frac{x}{\sqrt{4Dt}})dx \tag{2.25}$$

By changing the variables and limits of integration to:

$$\begin{aligned} \frac{x}{\sqrt{4Dt}} &= \eta \\ dx &= \sqrt{4Dt}d\eta \\ x = 0 &\rightarrow \eta = 0 \\ x = \infty &\rightarrow \eta = \infty \end{aligned} \tag{2.26}$$

one can obtain:

$$M(t) = \sqrt{4Dt}C_s \int_0^\infty erfc(\eta)d\eta \tag{2.27}$$

By using a well-known property of the error function complement:

$$\int_0^\infty erfc(\eta)d\eta = \frac{1}{\sqrt{\pi}} \tag{2.28}$$

The final solution can be obtained:

$$M(t) = \sqrt{\frac{4Dt}{\pi}}C_s \tag{2.29}$$

Although the exact relation can be different for various experiments, the general conclusion that the amount of material which diffuses into the sample is proportional to the square root of time is valid for most experiments with constant surface concentration of the diffusant.

Reflective boundary

So far only the solutions with a sample size approximated as infinite or semi-infinite were discussed and many times it was indicated that this assumption is not valid for many types of experiment. If the extent of the sample is comparable with the diffusion length it has to be determined what is happening with the diffusant at the sample boundary as it can undergo many different processes (e.g. evaporation, accumulation or reflection). Each situation should be considered, some are easy to calculate while other cannot be solved analytically and require numerical methods.

At the beginning let us consider a simple case of a reflective boundary. Initially the material is confined and evenly distributed over a slab with thickness $2h$ centered at $x = 0$. Using the superposition principle it is easy to derive the diffusion equation for a system which extends between $x = -l$ and $x = l$. It is expressed with infinite series of error functions:

$$C(x,t) = \frac{1}{2}C_0 \sum_{-\infty}^{\infty} (erf\frac{h + 2nl - x}{\sqrt{4Dt}} + erf\frac{h - 2nl + x}{\sqrt{4Dt}}) \tag{2.30}$$

Figure 2.12 presents this general solution for a case with a finite source and a finite system size. By exploiting the superposition principle one can easily derive the solution for other types of sources (planar, volume or constant surface concentration) with reflective boundaries.

Laplace transform

As it was already briefly indicated, many diffusion problems are difficult or even impossible to solve using the standard calculation procedures. However, there are several mathematical methods which proved to be helpful in physics, particularly in solving partial differential equations. Among other the Laplace transform seems to be very suitable for solving the diffusion equations.

The Laplace transform is a linear operator that transforms the function $f(t)$ to a function $\hat{f}(p)$ and is defined as:

$$\hat{f}(p) = \int_0^{\infty} e^{-pt} f(t) dt \tag{2.31}$$

where the argument t is a non-negative real number while p is a complex number sufficiently large to converge the integral. Frequently the argument of the initial function t is associated with time and the Laplace transform change the function from the time domain to the frequency domain. This alternative description proved to be very useful as many calculations and

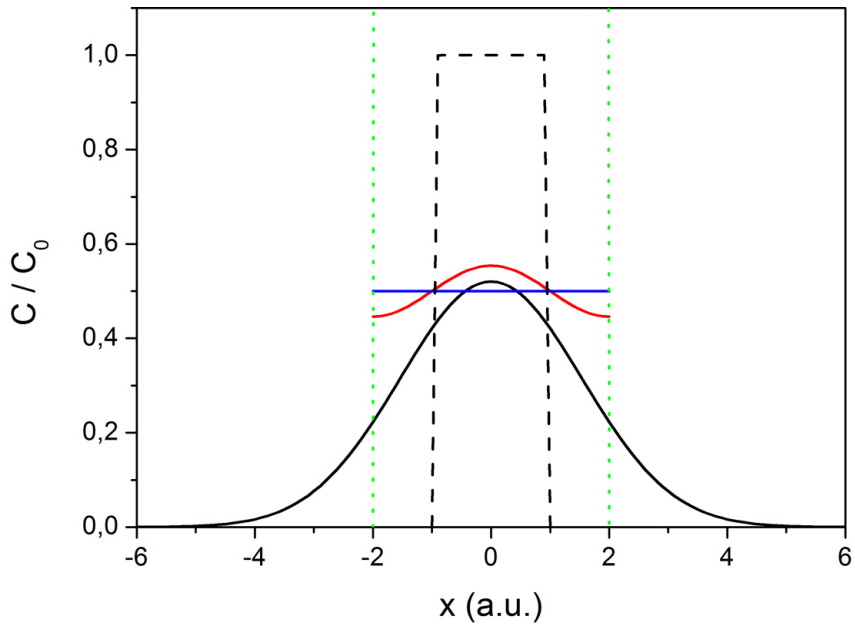

Figure 2.12: Diffusion from slab with a width of $2h = 2a.u.$ for a sample which extents between $x = -2a.u.$ and $x = 2a.u.$ (green dotted lines). Black lines show the initial distribution of diffusant (dashed) and the distribution for a diffusion length $L_d = 2a.u.$ (solid) if there were no boundaries in the system (two semi-infinite regions). Red line shows the correction of the diffusant distribution for the same diffusion length with a presence of reflective boundaries. Blue line indicate that for sufficiently large times the distribution of the material in the system with reflective boundaries is uniform. Furthermore, the final concentration is half of the initial one, which was expected since the width of the sample was two times larger than the width of the initial slab.

operations are easier to perform in the frequency domain than in the time domain.

In case of the diffusion equation the Laplace transform removes the time variable, leaving a relatively simple ordinary differential equation and its solution can be interpreted as the transform of the concentration field. By performing the inverse Laplace transform the final solution of the equation of concentration expressed with both space and time variables can be obtained.

The exact description of the method, its applications and the tables of Laplace transforms can be found in numerous literature [131–146]. Further applications of the Laplace transform into the diffusion problems are described in some books as well [126, 129, 147]. In this work only a few useful

examples of solving the diffusion equation with the Laplace transform technique will be shown.

As an example let us consider the diffusion into a semi-infinite sample with a constant surface concentration C_s located at $x = 0$. For $t = 0$ the concentration of diffusant is 0 for a positive x-axis. By multiplying the diffusion equation (Equation 2.6) by e^{-pt} and integrating one can obtain:

$$\int_0^\infty e^{-pt}\frac{\partial C(x,t)}{\partial t}dt = D\int_0^\infty e^{-pt}\frac{\partial^2 C(x,t)}{\partial x^2}dt \tag{2.32}$$

In the right hand side the order of integration and differentiation can be exchanged leading to:

$$D\int_0^\infty e^{-pt}\frac{\partial^2 C}{\partial x^2}dt = D\frac{\partial^2}{\partial x^2}\int_0^\infty e^{-pt}C(x,t)dt = D\frac{\partial^2 \hat{C}(x,p)}{\partial x^2} \tag{2.33}$$

While the integration by parts of the left hand side leads to:

$$\int_0^\infty e^{-pt}\frac{\partial C(x,t)}{\partial t}dt = [C(x,t)e^{-pt}]_0^\infty + p\int_0^\infty e^{-pt}C(x,t)dt = p\hat{C}(x,p) \tag{2.34}$$

The first term vanished because of the property of the exponential function and the initial conditions ($C(x, t = 0) = 0$) leading to the final formulation of the transformed diffusion equation:

$$D\frac{\partial^2 \hat{C}(x,p)}{\partial x^2} = p\hat{C}(x,p) \tag{2.35}$$

The boundary conditions should be transformed as well:

$$\hat{C}(x = 0, p) = C_s\int_0^\infty e^{-pt}dt = \frac{C_s}{p} \tag{2.36}$$

The solution of Equation 2.35 that fulfills the boundary condition is:

$$\hat{C}(x,p) = \frac{C_s}{p}e^{-\sqrt{\frac{p}{D}}x} \tag{2.37}$$

According to the available tabulations, the corresponding Laplace transformation pair is:

$$f(t) = erfc(\frac{a}{2\sqrt{t}}) \Leftrightarrow \hat{f}(p) = \frac{1}{p}e^{-a\sqrt{p}} \tag{2.38}$$

And therefore the final solution of the diffusion equation can be obtained:

$$C(x,t) = C_s erfc(\frac{x}{\sqrt{4Dt}}) \tag{2.39}$$

The same solution was already given in Equation 2.24 where the constant surface concentration problem was treated by standard calculation methods. It proves the validity of the Laplace transformation technique. However, as it was mentioned before, there are many cases which cannot be solved directly and the Laplace transform technique finds its superior application.

Constant surface concentration and finite sample size

Let us consider the diffusion in a finite medium between $x = 0$ and $x = l$ with the boundary conditions:

$$C(x = 0, t) = 0 \tag{2.40}$$

$$C(x = l, t) = C_s \tag{2.41}$$

and the initial condition:

$$C(x, t = 0) = 0 \tag{2.42}$$

The Laplace transformed diffusion equation was already derived and reads:

$$D\frac{\partial^2 \hat{C}(x,p)}{\partial x^2} = p\hat{C}(x,p) \tag{2.43}$$

The transformation of the boundary condition leads to:

$$\hat{C}(x = 0, p) = 0 \tag{2.44}$$

$$\hat{C}(x = l, p) = C_s \int_0^\infty e^{-pt} dt = \frac{C_s}{p} \tag{2.45}$$

The general solution of Equation 2.43 is

$$\hat{C}(x,p) = Ae^{qx} + Be^{-qx} \tag{2.46}$$

where

$$q = \sqrt{\frac{p}{D}} \tag{2.47}$$

Equations 2.44 and 2.44 yield:

$$A = -B \tag{2.48}$$

$$\frac{C_s}{p} = A(e^{ql} - e^{-ql}) \tag{2.49}$$

Thus, the solution can be formulated as:

$$\hat{C}(x,p) = \frac{C_s}{p}\frac{e^{qx} - e^{-qx}}{e^{ql} - e^{-ql}} \tag{2.50}$$

If the size of the sample l is large compared to the characteristic length of the diffusion, then the second term in the denominator can be neglected resulting in:

$$\hat{C}(x,p) = \frac{C_s}{p}(e^{-q(l-x)} - e^{-q(l+x)}) \tag{2.51}$$

Performing the inverse Laplace transform given by Equation 2.38 the final solution can be obtained:

$$C(x,t) = C_s[erfc(\frac{l-x}{\sqrt{4Dt}}) - erfc(\frac{l+x}{\sqrt{4Dt}})] \tag{2.52}$$

Apparently, Equation 2.52 fulfills the surface boundary condition given by Equation 2.40 while for the $x = l$ the result is:

$$C(x=l,t) = C_s erf(\frac{l}{\sqrt{Dt}}) \tag{2.53}$$

which deviates from the boundary condition given by Equation 2.41, but only to a small extent, as the error function is close to 1 when l is large compared to the characteristic diffusion length, which was previously assumed.

Figure 2.13 illustrates the Equation 2.52 for reduced units. At large times, when the diffusion length becomes comparable to l, the profile approaches the expected linear function. It can be further acknowledged that even for the diffusion length equal to the sample extent l the deviation from the boundary condition located at $x = l$ is hardly noticed and is less than 0.5%. It provides the additional proof of the validity of the model.

It is also important to determine the total amount of material that diffuses into the sample per unit area in time. It can be calculated as follows:

$$M(t) = \int_0^l C_s[erfc(\frac{l-x}{\sqrt{4Dt}}) - erfc(\frac{l+x}{\sqrt{4Dt}})]dx \tag{2.54}$$

The first integral can be calculated by changing the variables and the limits of integration as follows:

$$\begin{aligned} \frac{l-x}{\sqrt{4Dt}} &= \eta \\ dx &= -\sqrt{4Dt}d\eta \\ x = 0 \rightarrow \eta &= \frac{l}{\sqrt{4Dt}} \\ x = l \rightarrow \eta &= 0 \end{aligned} \tag{2.55}$$

and thus

$$\int_0^l erfc(\frac{l-x}{\sqrt{4Dt}})dx = -\sqrt{4Dt}\int_{\frac{l}{\sqrt{4Dt}}}^0 erfc(\eta)d\eta \tag{2.56}$$

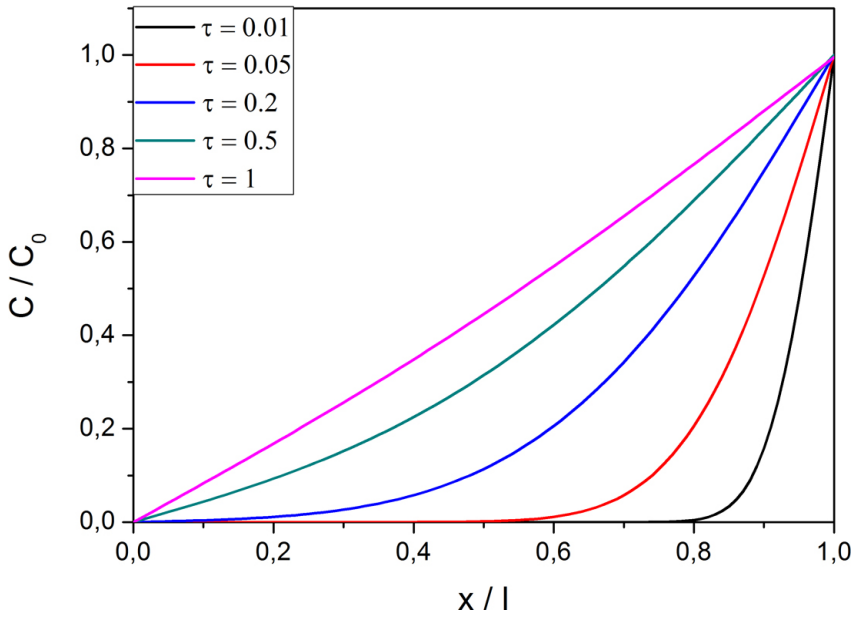

Figure 2.13: Normalized diffusion profiles for a reduced depth $\frac{x}{l} = 0...1$ at reduced times $\tau = \frac{4dt}{l^2}$

Based on a well-known property of the error function complement:

$$\int erfc(\eta)d\eta = \eta erfc(\eta) - \frac{e^{-\eta^2}}{\sqrt{\pi}} + C \tag{2.57}$$

The first integral takes the form:

$$\sqrt{4Dt}[\frac{1}{\sqrt{\pi}} + \frac{l}{\sqrt{4Dt}}erfc(\frac{l}{\sqrt{4Dt}}) - \frac{e^{-(\frac{l}{\sqrt{4Dt}})^2}}{\sqrt{\pi}}] \tag{2.58}$$

The same procedure should be applied to the second integral and thus the final solution can be formulated:

$$M(t) = \sqrt{4Dt}C_s[\frac{1}{\sqrt{\pi}} + \frac{2l}{\sqrt{4Dt}}erfc(\frac{l}{\sqrt{4Dt}}) - \frac{2e^{-(\frac{l}{\sqrt{4Dt}})^2}}{\sqrt{\pi}} + \\ - \frac{2l}{\sqrt{4Dt}}erfc(\frac{2l}{\sqrt{4Dt}}) + \frac{e^{-(\frac{2l}{\sqrt{4Dt}})^2}}{\sqrt{\pi}}] \tag{2.59}$$

As it was already assumed that the size of the sample l is much larger than the diffusion length $L_d = \sqrt{4Dt}$ and therefore all terms in the bracket but the first

vanish as both, the complementary error function and exponential function vanish for large argument. Therefore a simple solution can be derived:

$$M(t) = \sqrt{\frac{4Dt}{\pi}} C_s \tag{2.60}$$

which is similar to the Equation 2.29 which was previously derived for diffusion into the semi-infinite system with the constant surface concentration and therefore the same conclusion can be applied in this problem: the quantity of material that diffuses into the sample per unit area is proportional to the square root of the time of the experiment if the diffusion length is much smaller than the size of the sample. Figure 2.14 presents a suitable comparison of exact solution M_e according to Equation 2.59 and simplified M_s according to equation 2.60 for a reduced time $\tau = \frac{4Dt}{l^2}$. As expected, plots are in a perfect agreement for small values of the reduced time i.e. when the sample size is much larger than the diffusion length. The error in estimation of M_s is still below 5% for $\tau = 0.5$ which corresponds to $L_D \approx 0.7l$.

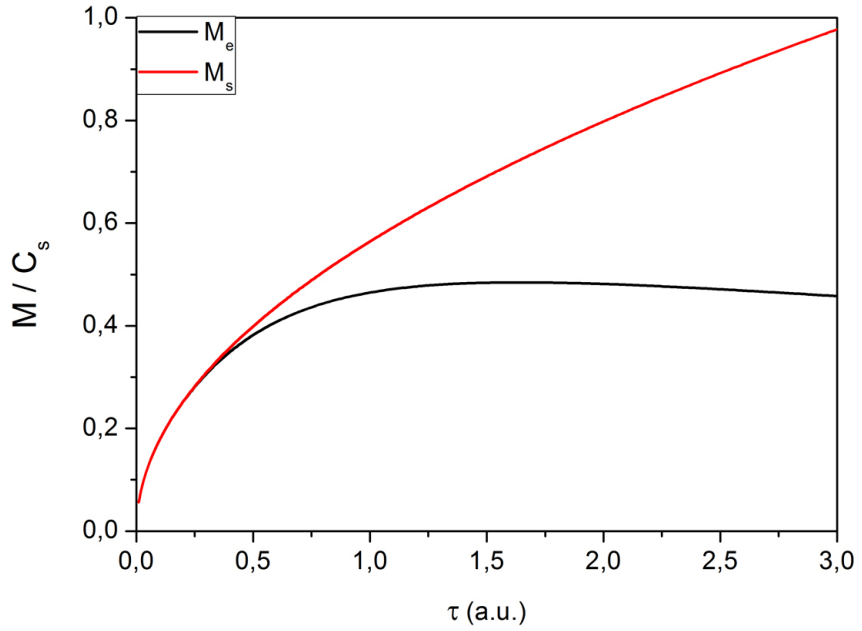

Figure 2.14: The total amount of material that diffuses into the sample per unit area at the reduced times $\tau = 0...3$. M_e and M_s denotes the exact and simplified solutions, respectively. The conformity is very good at lower times.

It is further interesting to calculate the gradient of the concentration at $x = 0$ which determines the flux through the boundary there. By differenti-

ation this becomes :

$$J(x=0,t) = \frac{\partial C(x,t)}{\partial x}|_{x=0} = \frac{4C_s}{\sqrt{\pi}l}\sqrt{\frac{l^2}{4Dt}}e^{-\frac{l^2}{4Dt}} \tag{2.61}$$

Figure 2.15 shows the gradient at the boundary located at $x = 0$. It approaches 1 in the reduced units at increasing time, which corresponds to $\frac{C_s}{l}$ and thus approaches the linear concentration function at large times. At times where the diffusion length exceeds the thickness ($\tau > 1$ in Figure 2.15), the approximation described above ($l \gg L_d$) leads to an apparent error and an artificial decrease of the gradient, which, however, still remains close to 1.

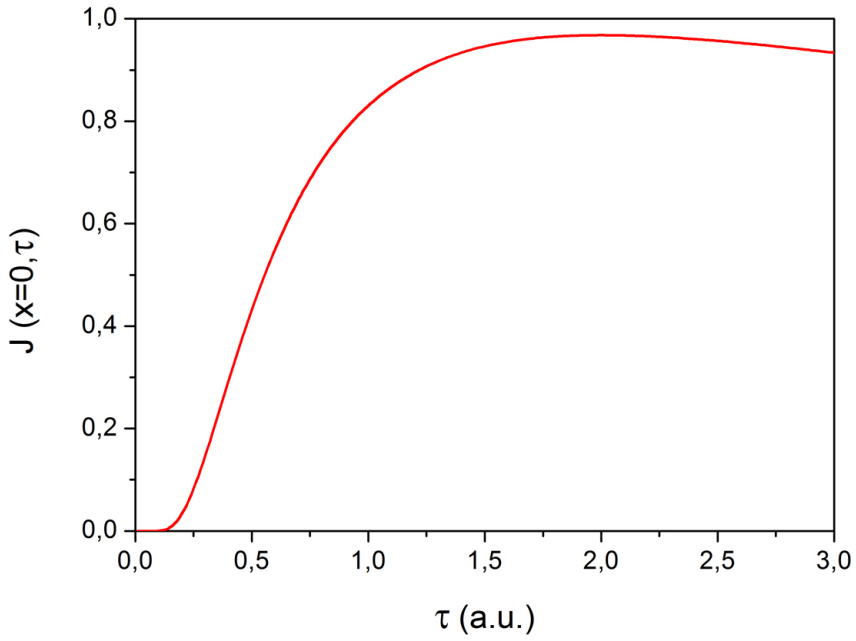

Figure 2.15: Surface gradient according to Equation 2.61 with $C_s = 1$ for the reduced time $\tau = 0...3$.

2.3.3 Arrhenius equation

The Fick's laws provides the general prediction about the rate of diffusion but do not describe the dependence upon thermodynamic variables such as temperature and pressure. The dependence on the latter was reported to be relatively small [148–154] as the diffusion decreases less than one order of

magnitude for pressures of $1GPa$. In the following experiments no intentional pressures were induced and therefore this subject will not be discussed.

Far more important is the temperature dependency as it has a significant impact on the diffusion process. An intensive study of the relation of the diffusion rate on temperature has been carried worldwide [148, 149, 155–163]. It has been noted that frequently (but not always!) the dependence of the diffusion coefficient on the temperature follows the simple empirical equation which is widely known as the Arrhenius equation. It describes the dependence of the rate constant of a chemical reaction on the temperature and the activation energy. It can be used to describe the temperature variation of diffusion coefficients, population of crystal vacancies, creep rates, and many other thermally-induced processes. The temperature dependence of the diffusion coefficient reads as:

$$D_a = D_0 e^{-\frac{E_a}{k_B T}} \tag{2.62}$$

where D_0 is the diffusion coefficient at infinite temperature, E_a is the activation energy for diffusion, k_B is the Boltzmann constant and T is the temperature. Both D_0 and E_a are often called the activation parameters of diffusion and the determination of them is a crucial task to obtain the knowledge about the diffusion process. The collection of the activation parameters can be found in [155] for metals and alloys and in [156] for semiconductor and other non-metallic materials.

2.3.4 Diffusion mechanism

The qualitative description of the diffusion process can be delivered by solving the Fick's laws of the diffusion and the Arrhenius equation. However, those equations are empirical and can be applied to any diffusion process, regardless the state of matter. To understand deeply the diffusion process in solid state materials and the difference compared to the diffusion in fluids, further investigations should be performed.

From a microscopic point of view the diffusion is accomplished by the Brownian motion of atoms or molecules. This kind of behavior was first observed by a botanist Robert Brown in 1827. However, the explanation of this phenomenon was delivered much later, in 1905 by Albert Einstein [164] who characterized the chaotic motion of small particles suspended in a liquid. The similar work about the thermally induced motion was delivered by Marian Smoluchowski [165] and therefore the relation between the diffusion coefficient and the mean square displacement of particles is called the Einstein-Smoluchowski relation. The excessive theoretical knowledge about

the atomic movement in solids will not be presented in this work. The information about its basics: a random walk theory, atomic jump process, jump rates, jump distances, activation energy of individual jump, correlation factor and the dependence on the size and chemical nature of the diffusing atom can be found in the literature [166–170].

The central aspect of this section is to provide the answer how atoms can move inside a solid sample. Although the effects of diffusion may seem to be the same, the material transport can be due to various mechanism. In the case of the crystalline material the main consideration is the periodic structure of the lattice which will limit the quantity of possible positions to occupy by diffusing particles and thus the diffusion path as well. For simplification, only the impurity diffusion will be considered in the following examples, although the same mechanisms can be applied to a self-diffusion as well. Several types of diffusion mechanism were suggested:

- Direct exchange and ring mechanism - one of the first explanations of the diffusion mechanism was a direct exchange hypothesis which assumed that two neighboring atoms can swap their positions (see Figure 2.16.1.). However, this would lead to a drastic distortion of a periodic lattice, especially for close-packed structures and therefore it was concluded that it is unlikely for such an energetically unfavorable process to occur in a crystalline sample [171, 172]. Later, a simple modification of this mechanism was proposed by Jeffries [173] and Zener [174] and called a ring mechanism. Its basic assumption was that three or more atoms may rotate simultaneously effectively exchanging their positions (see Figure 2.16.2.). The lattice distortions would be considerably smaller, but, as it required a simultaneous motion of more atoms, it was also concluded that there is no premise to accept it as a probable theory. The final proof was delivered by Kirkendall [175, 176] who substantiated the different rates of self-diffusion of atoms in a binary alloy. Neither the direct exchange nor the ring mechanism was able to explain this behavior

- Direct interstitial mechanism - as it was discussed in Section 2.2.1 some impurities are small enough to fit in interstitial sites of the host lattice. If they are provided with enough energy they can move along interstitial positions. The movement is achieved in gradual manner i.e. the impurity will jump only to a neighboring interstitial site, but eventually they can travel long distances without the permanent displacement of the matrix atoms. This kind of diffusion is not mediated by any defects and therefore the diffusion coefficient related to the direct interstitial mechanism is usually high. However, only small atoms like H, C, N,

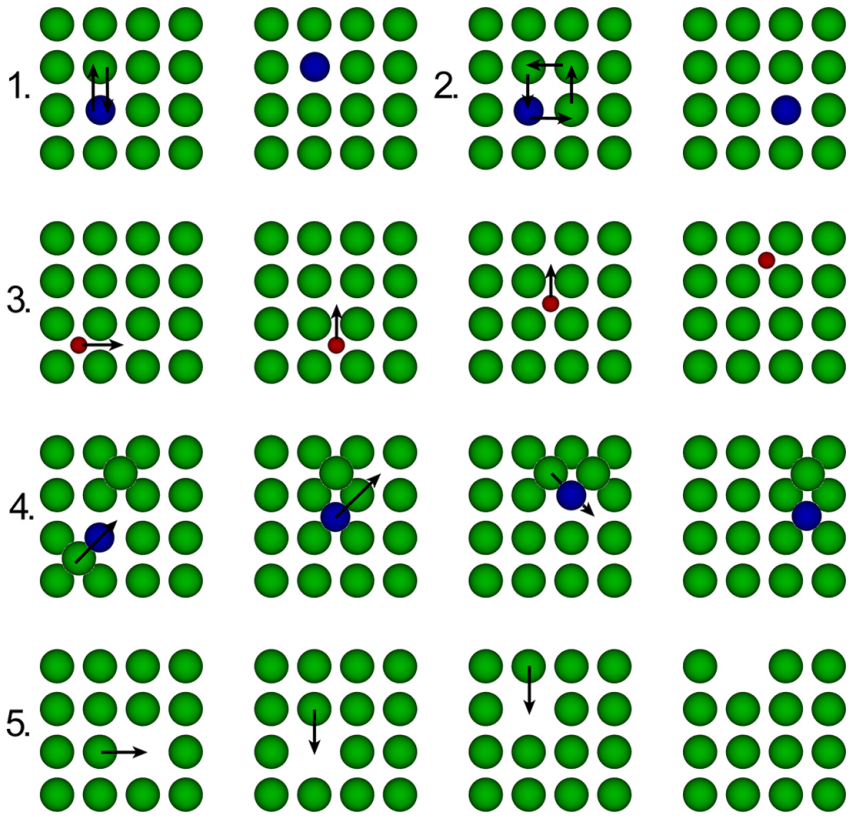

Figure 2.16: Various diffusion mechanisms: 1. The direct exchange mechanism. 2. The ring mechanism. 3. Direct interstitial mechanism. 4. Indirect interstitial mechanism. 5. Vacancy mechanism

and O incorporated in less dense materials may diffuse in this manner. The basic concept of the direct interstitial diffusion is shown in 2.16.3.

- Indirect interstitial mechanism - it concerns much bigger impurities which cannot move freely along voids in a crystal lattice and therefore occupy substitutional sites. However, their movement can be driven by interstitial defects and thus the name of the mechanism. An example of indirect interstitial diffusion is shown in Figure 2.16.4. The substitutional impurity is located next to the self-interstitial defect (the same consideration will hold for the impurity interstitial defect as well) and the collective motion of both defects can be promoted: the self-interstitial defect knocks out the impurity atom to some other interstitial site and takes its place. In the next step the impurity may move to another substitutional site, pushing a host atom to the interstitial site. This mechanism is strong for radiation-induced diffusion in metals and diffusion of dopants in silicon.

- Vacancy diffusion - where the diffusing atom is occupying a substitutional position in a lattice and its transport is mediated by an exchange with neighboring vacancy (see Figure 2.16.5.). By making a series of exchanges with vacancies the diffusing atom can travel a significant distance. Furthermore, it can be acknowledged that if a vacancy is considered as a particle it effectively travel the opposite direction than the diffusing atom. From a microscopic point of view it is essential to distinguish the diffusion mediated by vacancies and divacancies as their mobility is different and in some cases the diffusion via divacancies can be the dominant mechanism [177, 178]. However, the formation energy and mobility of defects is not a scope of this work and therefore the exact difference between two mechanisms will not be discussed, only the general mechanism of the diffusion mediated by vacancy defects will be considered.

There might be some more diffusion mechanisms in crystalline samples, but they usually find their applications only for systems fulfilling special conditions (e.g. higher than expected diffusion was observed for system near the phase transition [179, 180]) and therefore they will not be discussed. From the set of basic mechanism described above a straightforward conclusion can be formulated that the defect-mediated mechanisms are the most common in crystals since non-defect mechanisms are either unfavorable (direct exchange and ring mechanism) or apply only to small diffusing atoms (direct interstitial mechanism).

The situation is, however, different for amorphous materials. As it was stated in Section 2.2, the concept of defects in amorphous materials cannot be directly applied because of the lack of periodicity of a sample. Therefore it can be concluded that the diffusion mechanism for amorphous materials should be essentially different from that for crystals. Two basic mechanisms were suggested:

- Dangling bond mechanism - is somewhat similar to the vacancy mechanism in crystalline samples and is sometimes indicated with the same name. Its basic concept is the same: the movement of the diffusing atom is mediated by a missing host atoms and the defect propagates in the opposite direction. By a series of microscopic interchanges the diffusing atom may travel for macroscopic distances.

- Collective mechanism - the chaotic distribution of atoms and relatively weak bonding in amorphous materials allow the simultaneous movement of a larger number of atoms. It is usually described as a chain-like or caterpillar-like fashion (see Figure 2.17). Unlike in crystalline samples, atoms are not bound to specific positions defined by the lattice properties and therefore their movement is not so strongly restricted and thus the collective mechanism is considered to be relatively common (but not exclusive!) for amorphous materials. However, the diffusion rate is usually low, as a large number of atoms is required to be set in motion simultaneously.

2.3.5 Limitations of the diffusion process

In the previous sections the detailed information about the diffusion process has been presented. This knowledge was, however, quite specific and a more general point of view is required before continuing to the experimental part of this work. It is obvious that in reality the diffusion is not achieved by one mechanism solely, but rather by a combination of several mechanisms, out of which one can be, in fact, dominant. Furthermore, all previous considerations, despite including the defect theory, were rather idealistic and contained a lot of silent assumptions. Among many of them one can list:

- Perfection of the source of the diffusing atoms - not only the concentration of the diffusing atoms was set to be constant, but also their ability to penetrate into a sample was assumed to be unlimited.

- Homogeneity of the sample.

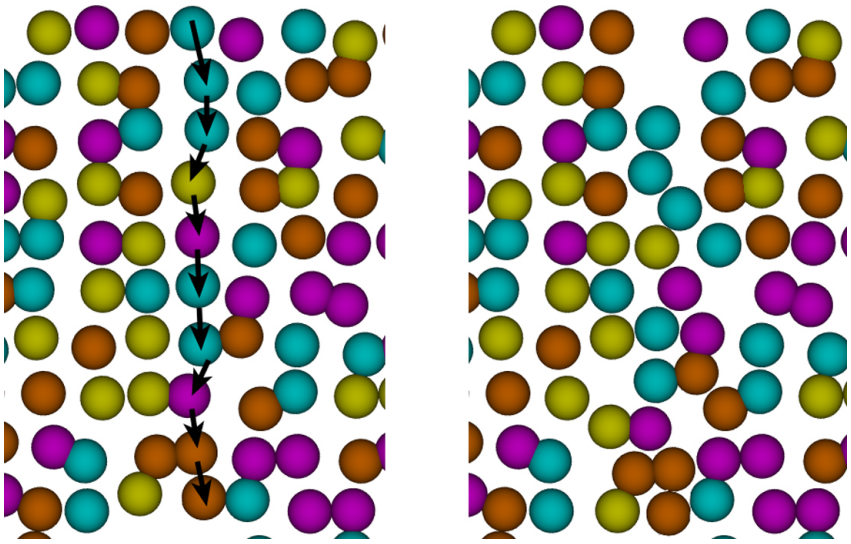

Figure 2.17: Chain-like diffusion mechanism for amorphous solids. A collective motion of several atoms can be observed.

- Trapping of diffusing atoms was not considered.

Therefore the scope of this section is to collect all previously acquired information and create a realistic model of the diffusion process. This will be achieved in three steps, each concerning regions of interest: source, bulk and the surface of the sample.

Source

Sources of the diffusing particles may vary in many aspects and the basic criterion is its state of matter, as many processes will differ for gaseous, liquid and solid sources. In this work only solid state sources will be considered.

As it was presented in Section 2.3.2 the concentration of diffusing particles at the contact between the source and the sample is often set constant. This assumption is reasonable for many experiments, however, its validity should always be confirmed first. Otherwise it can lead to a serious miscalculation of the diffusing parameters.

The assumption of the constant source concentration gives rise to an additional difficulty, far more complex: the solution of the Fick's laws of the diffusion does not include the actual energy a diffusing atom should acquire to overcome the binding energy and to be injected from the source to the sample where it can start to diffuse around. This activation energy is considerable for solid state sources and may depend strongly on the type of a source-bulk

interface.

Furthermore, it would be short-sighted to assume that the activation energy is constant during the experiment as it can be altered by many factors. It was explained in Section 2.3.4 that in a very common diffusion mechanism mediated by vacancies, the defects travel the opposite direction than the diffusing particles. Eventually it will cause an excess of vacancies near the interface which can be considered as an additional thin layer with properties different from both source and bulk material. It is difficult to undoubtedly predict how it would influence the activation energy as it may act as a diffusion barrier or may promote bonds breaking in the source, which would increase and decrease the activation energy, respectively.

When both the source and the bulk material are solids the diffusion of particles will most probably occur in both directions, i.e. atoms from the sample region will diffuse into the source as well. It can further alter the properties of the source and thus change the activation energy of the injection.

Bulk

As it was already stated in the most of the previous derivations, the bulk material was considered to be homogenous, while in the reality this assumption is not necessarily valid. The diffusion process can be altered by several factors:

- Stack composition - the sample is not necessarily made of homogeneous material, a stacking composition is common in manufacturing high-k based electronic devices. Therefore it should be acknowledged that each layer will be characterized by different diffusion parameters D_0 and E_a. Furthermore, some additional energy might be necessary to inject the diffusing atom from one layer into the other which might further limit the diffusion.

- Trap states - as it was discussed in Section 2.2.5, defects has an ability to cluster and restrain the further motion. Diffusing particles can be considered as impurities and during their motion they may encounter other defects which will trap them and prevent further propagation. For example a void defect can easily trap diffusing impurities and restrain the diffusion.

- Diffusion barriers - some defects, especially planar, can form an impenetrable layer which will prevent the diffusing particle to travel any further. The same effect can be observed for a stack composition if the energy required for the injection from one layer to another is enormous and thus it would be virtually impossible for a particle to diffuse

through such a layer. Barriers will therefore limit the space where the diffusion may occur.

- Additional sources - in most cases it is assumed that there is only one source of the diffusing atoms, usually located at the interface with the sample. However, the diffusing particles may come from other sources as well, located at different positions, even inside the sample. An impurity precipitate incorporated inside the sample may be an example of such an additional source. The description of the diffusing process with many sources can be a challenging task.

- High diffusivity paths - as it was clearly indicated in Section 2.2.5 some defects may create high diffusivity paths where the mobility of the diffusion particles along the defects is enhanced. The so-called grain boundary diffusion mechanism in polycrystalline materials is a perfect example and is shown in Figure 2.18. Usually the D_0 is several order of magnitude higher for the grain boundary diffusion than for the bulk diffusion and additionally the activation energy of such diffusion is usually smaller. Therefore in most polycrystalline materials the grain boundary diffusion mechanism is dominant and the impact of the bulk diffusion can be neglected.

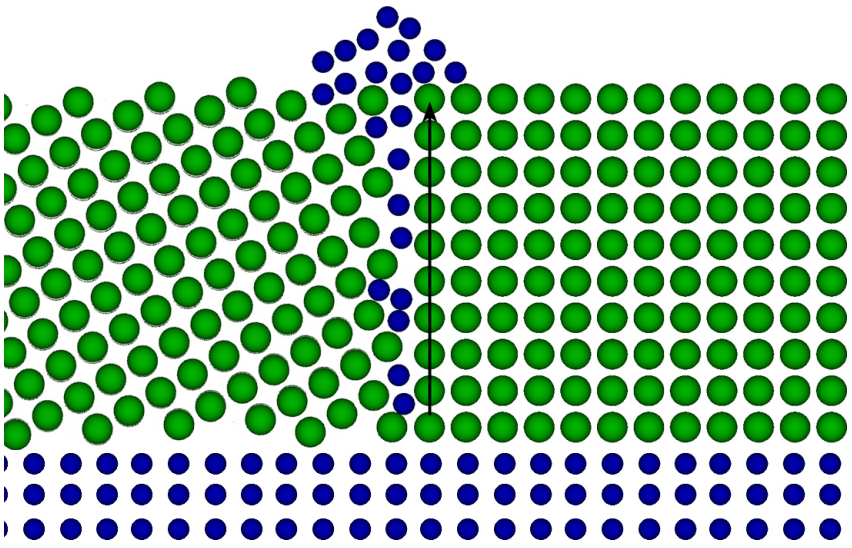

Figure 2.18: The grain boundaries form a so-called high diffusivity paths where the mobility of impurities is significantly enhanced in comparison to the bulk diffusion.

Surface

Section 2.3.2 presented several assumptions about the surface, but they were, however, rather a mathematical formalism, not a physical one and therefore it is essential to determine what may happen with the diffusant after reaching the surface of the sample. Three basic situations may be considered:

- Reflective boundary - the surface can be considered as a region where the activation energy for further movement is enormous and therefore particles are reflected and forced to move backwards.

- Evaporation boundary - particles that reaches the surface evaporate, i.e. are lost and have no further influence on the diffusion process. This corresponds well to the assumption with zero concentration at the surface.

- Sink boundary - particles are collected and agglomerated at the surface and therefore a process called surface segregation may occur. For a perfect sink surface it can be assumed that collected particles has no further influence on the diffusion process and therefore the zero concentration at the surface assumption is valid as well. There is, however, an essential difference between the evaporation and the sink boundary as the latter is subjected to a saturation of segregation where no more particles can be agglomerated at the surface of the sample.

  It should be also noted that even if the particles are collected at the surface and have no influence on the bulk diffusion, they can, however, move across the surface of the sample giving rise to a phenomenon called surface diffusion.

In reality it is rather uncommon for one of those basic surfaces to occur. Usually a combination of all effects can be expected and thus the complexity arises. As an example a surface with the following properties can be considered: a part of diffusing particles that reach the surface is reflected while the other part is agglomerated. The surface binding is, however, not perfect and some quantity of atoms evaporate. Furthermore the sinking properties can be imperfect as well and there might be high but finite activation energy for the agglomerate particles to be injected back into the sample and thus the segregated layer will efficiently work as an additional source of diffusing particles. Moreover, as the sample approaches the surface saturation phase the reflective properties of the surface might be increased at the expense of the sink properties.

Furthermore, it should be noted the influence of the surface on the diffusion process cannot be determined immediately after the beginning of the thermal processing of the sample as it has a finite thickness and it takes some time for the diffusing material to reach the surface. To obtain valuable information about the type of the surface boundary the diffusion with varying times should be analyzed

Diffusion rate

As it was clearly stated above, the transport of the particles is rarely achieved by one mechanism solely and therefore the total diffusion rate should be calculated with respect of this complexity. It is usually assumed that the total diffusion coefficient D_{tot} is given as a sum of contributions:

$$D^{tot} = D^I + D^{II} + ... \tag{2.63}$$

Combined with the Equation 2.62 it can be related to the diffusion parameters:

$$D^{tot} = D_0^I e^{-\frac{E_a^I}{k_B T}} + D_0^{II} e^{-\frac{E_a^{II}}{k_B T}} + ... \tag{2.64}$$

An effective value of the activation energy reads as follow:

$$E_a^{tot} = E_a^I \frac{D^I}{D^I + D^{II} + ...} + E_a^{II} \frac{D^{II}}{D^I + D^{II} + ...} + ... \tag{2.65}$$

and therefore a straightforward conclusion can be formulated: the diffusion mechanisms with a high activation energy might be neglected for low temperatures, but become more dominant for elevated temperatures.

However, those are the parameters describing only the diffusion process. It should be acknowledged that the injection of the particles from the source into the system requires some energy as well. Similarly, the influence of the surface on the diffusion process should be taken into consideration and therefore the parameters that are calculated from the experiment usually do not describe the particular type of the diffusion but the whole global diffusion process, including all important factors. This is very important to take into account, otherwise the upcoming experimental results might be incorrectly interpreted.

Chapter 3

Experimental setups

3.1 Sample preparation

In following section sample preparation techniques, namely Atomic Layer Deposition (ALD) and Rapid Thermal Annealing (RTA) will be shortly discussed. Apart from the theoretical description, information about the experimental conditions will be presented.

3.1.1 Atomic Layer Deposition

The Atomic Layer Deposition is a well known production technique that allows to deposit a uniform thin film of materials on a substrate[181–188]. The basic principle is a sequential use of pulses of gaseous precursors producing one atomic layer per cycle. Thus the method is self-limiting. It provides extremely high uniformity of the deposited films and excels control of their thickness as, within a certain range of process conditions, it is independent on all factors but the number of cycles. The growth of a monolayer takes place in four basic steps:

1. The first precursor is introduced into the process chamber resulting in the formation of an adsorbed monolayer on the surface of the substrate of the growing film.

2. A purge gas (typically nitrogen or argon) is introduced into the reaction chamber to remove remaining precursor species and other reaction by-products.

3. A second precursor is introduced to activate the surface and allow further reaction of the first precursor with the surface (sometimes this step is done together with additional activation, e.g. thermal treatment).

4. Reaction chamber is purged again.

Each cycle results in the formation of a single monolayer and allows to be repeated to produce thicker films. The basic principle of the ALD process is shown on Figure 3.1

A typical setup of an ALD chamber is presented on Figure 3.2. The system has to be designed in a way which allows a rapid reaction of the precursors with the substrate during the gas pulses and also a rapid purging in between.

The main advantage of the ALD process when compared to other techniques (e.g. chemical vapor deposition) is a simple and very accurate thickness control based on the number of cycles. Furthermore thin films have excellent uniformity as well as reproducibility and the growth of the different multilayer structures is straightforward. The major drawback of the ALD process is the deposition rate which is very limited. Nevertheless in the case of thin film deposition, where only a few nanometers (and thus cycles) are needed, this is not a significant issue. Some other limitations are the possibility of relatively high contamination and the impossibility to deposit several technologically important materials like Si, Ge or Si_3N_4.

For the following experiments, series of Al_2O_3 thin films and $Al_{1-x}Si_xO_y$ composite layers were fabricated by the Picosun P-300 Atomic Layer Deposition on cleaned p-type Si(001) wafers with a 1.2nm thick native oxide or with an additional 5nm Si_3N_4 layer above the oxide. The Al and Si precursors were trimethylaluminium + water and tris-dimethylamino-silane + ozone, respectively. Samples were produced with thickness ranging from 2 to 50nm. The standard value for which most experiments were performed is 15nm, and, unless otherwise specified, all descriptions concern this thickness. The composition of the $Al_{1-x}Si_xO_y$ was varied by adjusting the Al to Si precursor pulsing ratio between 6:1 and 1:4.

3.1.2 Rapid thermal annealing

The rapid thermal annealing is a manufacturing process which involves heating the sample to high temperatures for a specific time, usually ranging from a few seconds to several minutes[189–193]. The thermal treatment is a critical step in production of semiconductor devices as it may lead to the crystallization, damage repair, thermal oxidation, dopant activation, diffusion, formation of interfaces and many more phenomena. There are two basic groups of techniques used for heating the Si wafer: furnaces using steady heat sources and pulsed discharge lamps.

All samples were subjected to thermal treatment using the Mattson Flash

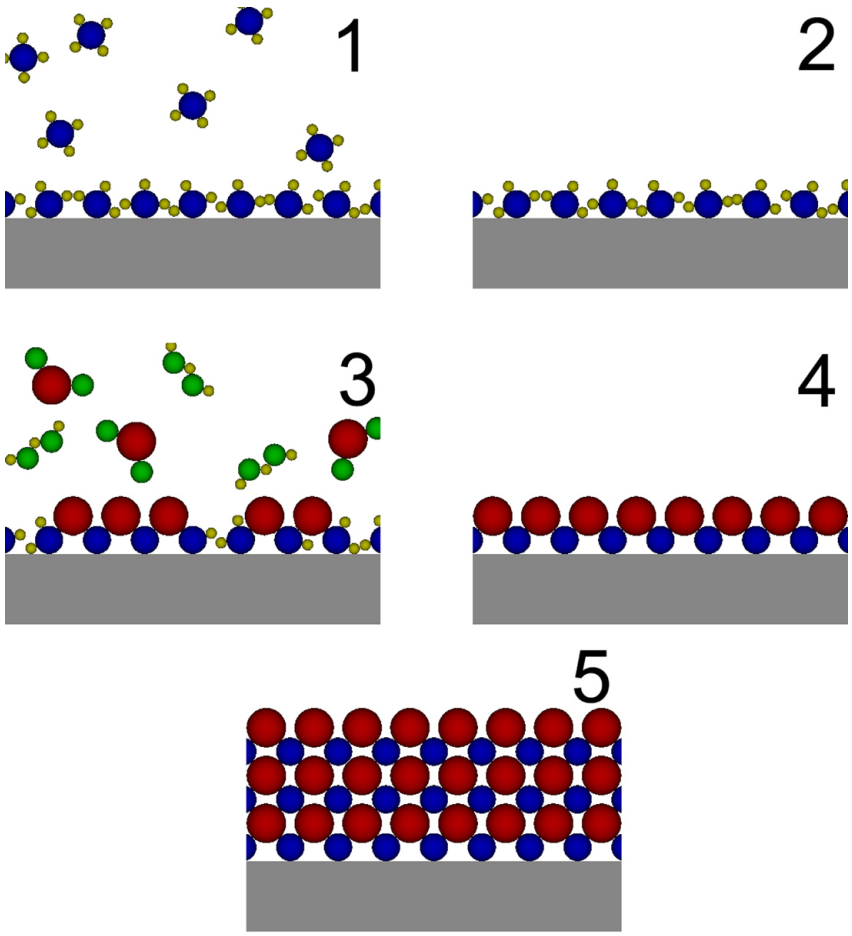

Figure 3.1: The basic principle of the ALD process. 1) Pulse of the first precursor, formation of the adsorbed monolayer on the substrate surface. 2) Purge. 3) Pulse of the second precursor, activation of the surface for the further deposition of the first precursor. 4) Purge. 5) The full cycle (step 1-4) can be repeated resulting in formation of desired number of monolayers of deposited material.

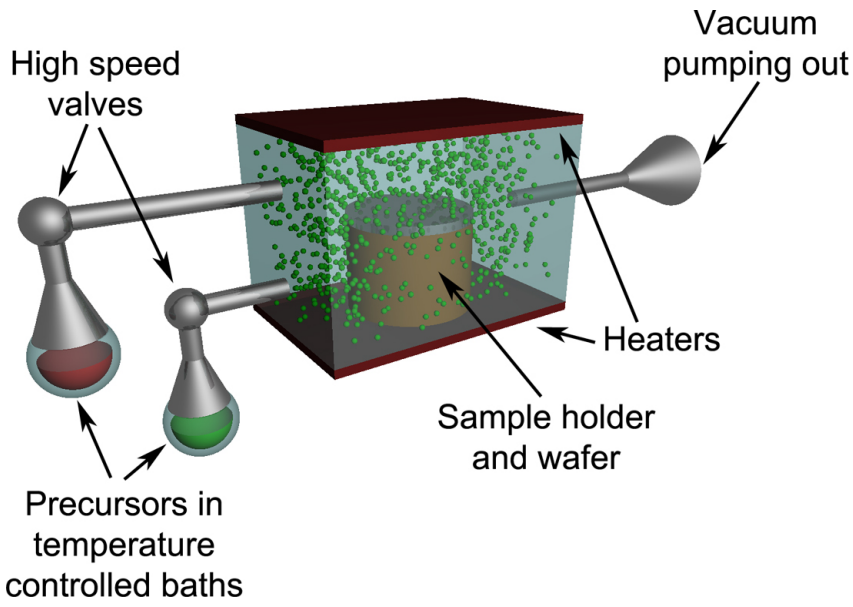

Figure 3.2: Atomic layer deposition system

Light Anneal Thermal Reactor, at different temperatures (600 - 1100°C), times (1 - 200s) and gas ambients (N_2, H_2, O_2). Unless it is specified otherwise, all further descriptions concern samples annealed for 20 seconds in the N_2 ambient.

3.2 Diagnostics

This part will cover all experimental techniques that were used in characterization of the diffusion process. Supplementary diagnostics (ellipsometry, X-ray techniques and Atomic Force Microscopy) will be shortly described along with the most important results whereas the central diagnostics for this work - Secondary Ion Mass Spectroscopy - will be explained in details with an extended discussion of the obtained results.

3.2.1 Ellipsometry

Ellipsometry is a non-destructive, non-contact optical method widely used for characterization of dielectric properties of thin films[194–198]. The goal is to measure the change of polarization of the light that was reflected (rarely transmitted) by the sample which can then be associated with the sample's

properties like the thickness and the complex refractive index or the dielectric function tensor. The standard ellipsometric setup is shown in Figure 3.3.

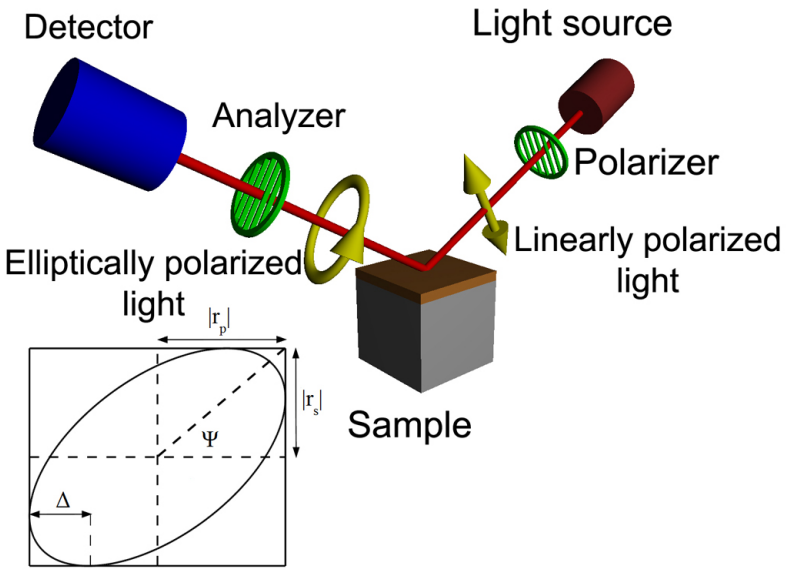

Figure 3.3: Basic principle of ellipsometry. Relative attenuation of s- and p-polarized light determines the tilt of ellipse while the relative phase shift determines the ellipticity.

In the single-wavelength ellipsometry the incident light is linearly or elliptically polarized and focused onto the sample. After reflection it is transmitted through a second polarizer (called analyzer) and reaches the detector. The light which is polarized parallelly or perpendicularly to the plane of incidence is called p- and s-polarized, respectively. The complex reflectance ratio follows the equation:

$$\rho = \frac{r_s}{r_p} = tan\Psi e^{i\Delta} \tag{3.1}$$

where r_s and r_p are the ratios of the complex amplitude of s and p components after and before reflection, respectively, $tan\Psi$ is the amplitude ratio and Δ is the phase shift. As the method measures the ratio of values it does not require any reference beam nor standard sample, although in most cases it requires a suitable model to convert measured values to desired physical parameters (direct calculation is only possible for simple cases of isotropic, infinitely thick samples).

However, the experimental output of the single-wavelength ellipsometry is restricted to one set of Ψ and Δ values per measurement. In order to determine the thickness and the complex refractive index of a sample simultaneously, the so-called spectral ellipsometry, which employs broad band light sources, should be used. After the measurement experimental data are compared to the predicted values calculated from a model. Even if thickness and optical constant of each layer is not known an estimate is given for the purpose of the preliminary calculation. Regression analysis is then performed to achieve the best match between the experimental data and the model. The unknown parameter are varied until an estimator (for example Mean Squared Error) reaches its minimum.

The thickness of all samples was obtained by SpectraFx 100 ellipsometer. Measurements were repeated after annealing to monitor the densification and thus shrinkage of samples due to crystallization.

3.2.2 Grazing incidence X-ray diffraction

The X-ray diffraction (XRD) is a technique that allows to determine the crystallographic structure of the sample[199–203]. The basic principle is the scattering of X-rays by the electrons surrounding atoms and molecules. From the produced diffraction pattern the structure of many different types of materials such as inorganic compounds, DNA and proteins can be obtained.

Figure 3.4 presents the basic principles of the XRD. A monochromatic X-ray plane wave is directed onto a sample consisting of N+1 equidistant atomic planes with spacing d. The incident and reflected angles equal θ. Typically, a value of the index of refraction for frequencies in the X-ray domain deviates from 1 by less than 10^{-5} and therefore the refraction effect in a general case can be neglected. Reflected waves will merge outside the crystal and the difference in the optical path for each wave gives rise to a phase shift. If the waves are in phase they will constructively interfere, resulting in a strong reflected wave with the amplitude N+1 times higher than that for a single reflected wave.

A well known condition for the constructive interference reads:

$$2d \sin \theta_n = n\lambda. \tag{3.2}$$

where θ_n is the so called Bragg angle for which interference of the nth order occurs. Longer wavelengths give larger Bragg angles and larger spacings d between the planes give smaller angles. For a given wavelength the Bragg angle can be measured and then the ratio $\frac{d}{n}$ can be calculated. If the order can be found than the spacing distance between planes can be determined.

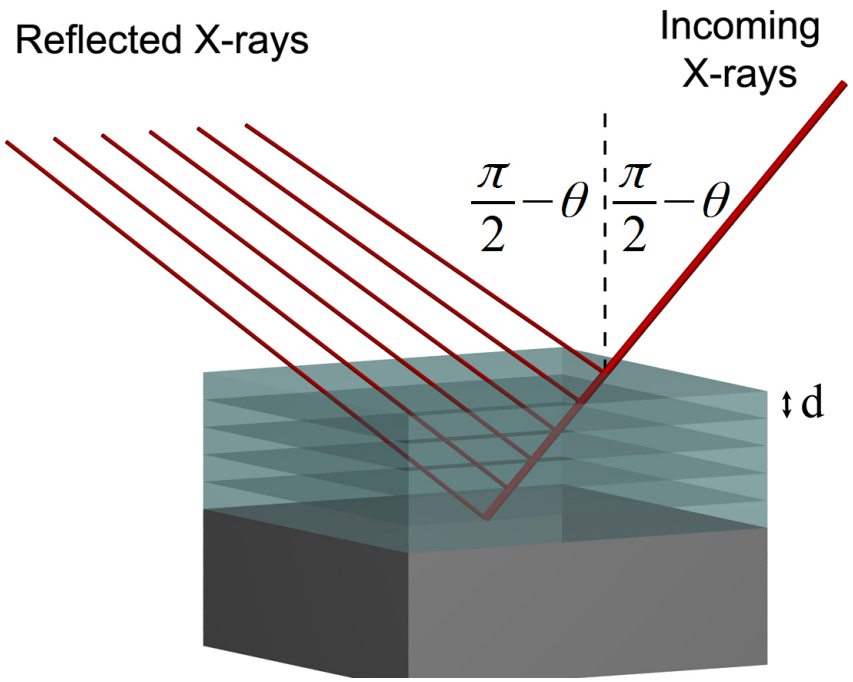

Figure 3.4: An example of the XRD principles: incoming X-ray radiation is reflected form five equidistant atomic planes with the spacing d. The incident and reflected angles equal θ. An interference of the reflected waves occurs.

Ideally the detected peaks should have infinitesimally small width width. However, this would only be true if the light was scattered by an infinite number of planes. As the number of reflecting planes decreases, the peak is broadened. A small but significant modification of the experimental setup can help to overcome this problem. The grazing incidence X-ray diffraction (GIXRD) is based on the fact that the refractive index of most materials at X-ray frequencies is slightly less than one and therefore the total external reflection of light from the surface is possible if the incident angle is small enough. This makes the technique extremely surface sensitive (down to nm scale).

In the following experiments, the Bede X-Ray Diffractometer was used to determine the crystallization phase of samples after annealing.

3.2.3 X-ray reflectometry

The X-ray-reflectometry (XRR) is a non-destructive and non-contact technique that can measure the thickness, density and the roughness of thin

films[204–206]. Furthermore it is possible to perform this measurement on multilayer samples as well.

Monitoring the intensity of the X-ray light reflected from a sample is the key of this technique. For an incident angles smaller than the critical angle a total external reflection occurs. It originates from the difference in electron densities between the layers and therefore can be related to the density of the material. The complex refractive index of a substance for X-ray beams is usually slightly less than 1 and given by:

$$n = 1 - \delta - i\beta \tag{3.3}$$

where both parameters δ and β depend on the X-ray wavelength and the density of the material. The critical angle is given by $\theta_c = \sqrt{2\delta}$ and thus the density of the thin film can be calculated and the thickness can be obtained by Fourier transformation of the extracted oscillation curve. This procedure, however, can only be applied for a perfect single-layer film. In practice such an idealized situation does not occur and therefore usually the experimental reflectivity curve is compared to the theoretical curve, based on a model. Regression analysis is then performed to achieve the best match between the experimental data and the model.

The Bede X-Ray Diffractometer was used to perform the XRR measurements. It was a backup method for the thickness characterization. The measurement of the density delivered an additional proof of crystallization as the crystalline sample are denser than the amorphous one.

3.2.4 X-ray photoelectron spectroscopy

The X-ray photoelectron spectroscopy (XPS) is a surface sensitive method that allows describing quantitatively the elemental composition and the chemical and electronic state of a sample[207–213]. This technique is based on the photoelectric effect - the phenomenon in which an incident photon leads to the ionization of an atom in a molecule or solid i.e. to the emission of an electron from the sample. In XPS a monochromatic source of radiation is used and therefore the overall process can be described as:

$$A + h\nu = A^+ + e^- \tag{3.4}$$

where A and A^+ denote neutral and ionized state of an atom A, respectively, h is the Planck constant, ν is the frequency of the radiation and e^- is the emitted electron. The energy conservation principle requires:

$$E(A) + h\nu = E(A^+) + E(e^-) \tag{3.5}$$

Since the energy of the emitted electron can be directly represented as its kinetic energy (KE) and the energy difference between the ionized and neutral atoms is as sum of the binding energy (BE) of the electron and the work function Φ (the difference between free electron level and the Fermi level) the formula can be expressed as follows:

$$KE = h\nu - BE - \Phi \tag{3.6}$$

This relation is also visualized on Figure 3.5. As the energy of the incoming photon is known, the obtaining of the photoelectron spectrum is based on presenting the number of emitted photoelectrons as a function of their binding energy. Each element will give rise to a unique set of peaks since they represent a characteristic binding energy associated with each core atomic orbital and therefore the elemental composition of the sample can be acquired. Furthermore, the intensity of peaks is related to the concentration of a specific element - that is number of detected electrons is proportional to the number of atoms in a given state - and thus the quantitative distribution of the surface elements is possible. The restriction to the top part of the sample (about 2nm) originates from the fact that electrons emitted from deeper regions are either recaptured or trapped in various excited states within the material or loses part of its energy due to the inelastic scattering.

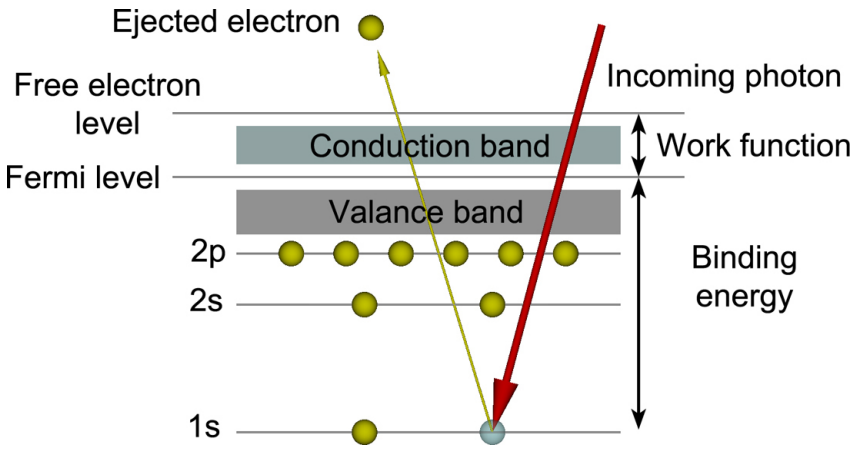

Figure 3.5: The principle of the XPS. The kinetic energy of an injected electron equals to the energy of photon minus the energy that was needed for the emission (the sum of the binding energy and the work function).

The Revera XPS Spectometer was used to determine the concentration of elements on the surface of samples allowing to create standards needed for other analytical techniques.

3.2.5 Capacitance-voltage profiling

Capacitance-voltage profiling (C-V profiling) is a technique used for characterization of semiconductor materials and devices [214–217]. The voltage that is applied to the device is varied and the measured capacitance is plotted as a function of voltage. It can provide many useful information such as capacitance, oxide thickness, doping profile or interface trap density.

However, in following experiments only the most simple and preliminary measurements to determine the capacitance (and thus the relative permittivity) of thin film samples were performed. Samples were relatively simple, with good uniformity and very low leakage current and therefore it was possible to apply one of the simplest C-V profiling method - Ramp Rate Method which is also often called Quasistatic C-V Measurement because it is performed at a very low test frequency (typically 1-10Hz), that is, almost DC. It only requires two source-measure units. The first one forces a current into a node of the sample while also measuring the voltage on that node and the second one measures the current at the other node. The capacitance can be therefore calculated as follows:

$$C = \frac{I}{\frac{dV}{dt}} \tag{3.7}$$

To successfully measure the capacitance of the samples their front side was covered with metal (aluminum and gold contacts were created, the results were comparable in both cases) forming one plate of the capacitor. The substrate - silicon wafer - could not by itself be the other plate of the capacitor and therefore a suitable voltage was applied to the wafer so that the majority charge carriers formed an accumulation layer directly at the interface between the substrate and the thin film region, effectively becoming the second plate of the capacitor whereas the thin film region was the insulator. One had to remember that the native oxide was present at the surface of the silicon wafer and therefore its contribution had to be excluded to obtain information about dielectric properties of the thin film region. The thickness was known from other measurements (ellipsometry, XRR) and thus the relative permittivity of the thin film was calculated.

Two Keithley 4200-SMU units were used to determine the relative permittivity of the samples.

3.2.6 Atomic Force Microscopy

The Atomic Force Microscopy (AFM) is a powerful technique which allows imaging of the surface of the sample with a resolution reaching the fraction of

a nanometer[218–223]. The AFM consists of a flexible cantilever with a sharp tip that is brought to the contact (or in some cases to close proximity) with the surface of the sample. An interaction between the tip and the surface can be attributed to many kinds of forces, among them: mechanical contact, van der Waals, capillary, chemical bonding, electrostatic, magnetic, Casimir, solvation forces, etc. They lead to the deflection of the cantilever which can be detected with the help of a laser which is shone on the cantilever and the reflection is detected by a position sensitive detector. The basic principle of the AFM is shown on the Figure 3.6.

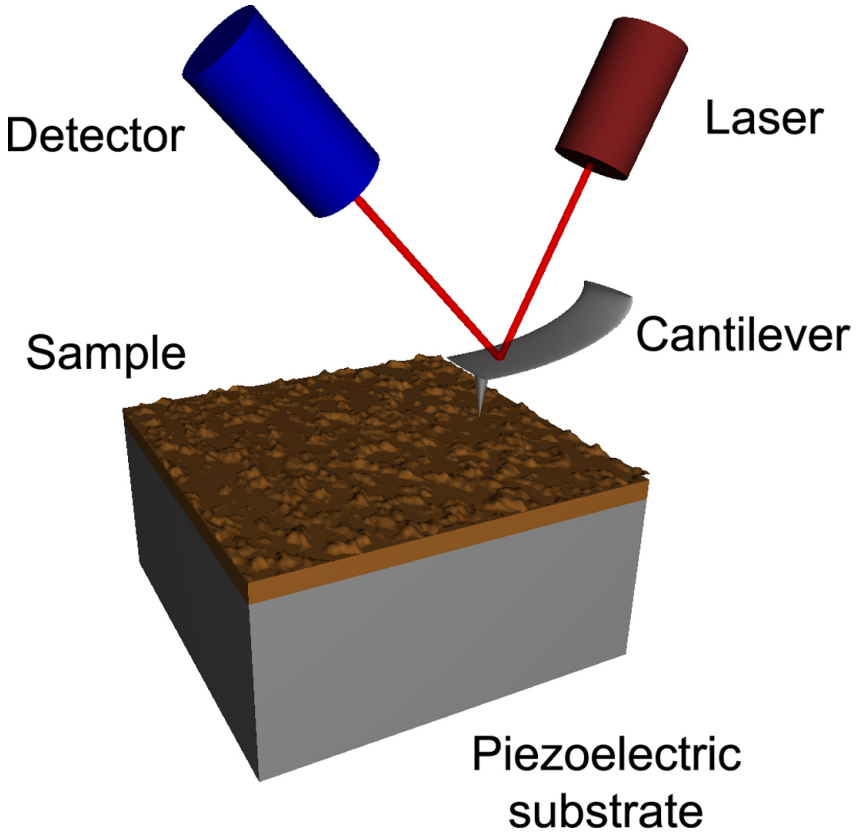

Figure 3.6: Atomic Force Microscopy setup.

To prevent the damage caused by the collision of the tip with the high feature of the sample the The AFM usually operates at the constant force mode - the piezoelectric sample holder rise or lower the sample to maintain the constant force. The movement of the sample is recorded and thus the morphology (and other parameters if other forces are present) can be obtained. The x and y plane movement allows to scan the surface of the

sample providing a three dimensional map of the surface of the sample.

Other operation modes (e.g. non-contact, tapping) will not be discussed as they were not used in this work. They are dedicated to characterization of soft and easily scratched samples.

In the following experiments the Veeco AFM was used to determine the surface movement of a Si island deposited on top of the sample during the thermal treatment.

3.2.7 Time-of-Flight Secondary Ion Spectroscopy

3.2.7.1 Basic principles

The Time-of-Flight Secondary Ion Spectroscopy (ToF-SIMS) is a powerful analytical technique that can provide information about elemental distributions in the sample[224–234]. The basic operation involves a bombardment of the surface of the sample with ions with energy usually in the range of 0.1 - 25 keV [230]. Primary ions collide with atoms of the sample and transfer part of their energy. If it is higher than the binding energy, then those atoms are also set in motion and will further collide with other atoms in the sample giving rise to a phenomenon called collision cascade.

Emission

A part of the energy of the primary ion will be transferred back to the surface region enabling atoms and molecules to be emitted from the sample, providing that the transferred energy is higher than the surface binding energy. Most of the emitted species are neutral, only a small fraction is positively or negatively charged. The mass spectroscopy of those secondary ions is a base for characterization of the surface of the sample [232].

SIMS is a very sensitive method for surface analysis because the emitted species originate only from one or two uppermost monolayers of the sample and thus the depth resolution of the method is very high [231]. The lateral resolution is far more challenging problem. In spite of the fact that species are emitted only a few nanometers away from the place where the sample was hit by the primary ion, the lateral resolution is mostly determined by the size of the ion beam, since the sample is not bombarded with single ions only, and typical value is in order of micrometers. Smaller beams could induce significant damage to the sample and bring about problems with the sensitivity.

Ion bombardment

SIMS is a destructive method. The emission of species is only the most

obvious effect of the ion bombardment. There are, however, more of them that need to be considered as they significantly change the structure of the sample. Before the proper analysis can take place these phenomena should be carefully described. Figure 3.7 presents the summary of principles of the SIMS technique.

- Ion implantation - the SIMS process is initialized by the bombardment of the surface of the sample with the beam of high energy ions (Figure 3.7 - position 1) which penetrates the sample, transfers the energy during collisions (Figure 3.7 - position 2) and finally is stopped and trapped in the sample. An obvious consequence is the change of the chemical composition of the sample as the primary ion species are introduced and mixed with the sample (Figure 3.7 - position 3). Furthermore the addition of the primary ions leads to the swelling of the sample as other atoms have to move to make space for incoming ions.

- Sputtering - the primary ion causes the motion of a significant number of atoms in the sample by direct collisions but also indirectly by giving rise to the collision cascade [224] (Figure 3.7 - position 2). A part of the energy is transferred back to the surface of the sample and atoms or even bigger molecules can be sputtered from the sample (Figure 3.7 - position 4) and thus a formation of a crater with rough edges can be observed. The sputtering process is quantitatively described by the parameter called partial sputter yield Y_A, which is defined as a number of sputtered species A per incident ion. This parameter strongly depends on both, the bombardment conditions (type, energy and incident angle of the primary ion) and properties of the sample (chemical composition, topography). The ratio between two partial sputter yields Y_A/Y_B of elements A and B is very rarely equal to the concentration of those elements. The probability of sputtering of one species can be significantly different from the other. This effect is called preferential sputtering and may lead to the depletion of one element when compared to the other (Figure 3.7 - position 5).

- Ionization probability - as it was described above, only the small fraction (usually about 1%) of species that are sputtered from the sample is ionized. The probability of ionization $\alpha(A)$ is defined as a ratio of the emitted ions $A^{\pm}$ to the total number of sputtered species A. Similarly as for the partial sputter yield, the ionization probability is strongly affected by the experimental condition and even for the same element can differ by several orders of magnitude for different primary ions. Some ions, for example Cs^+, enhance the formation of anions [227],

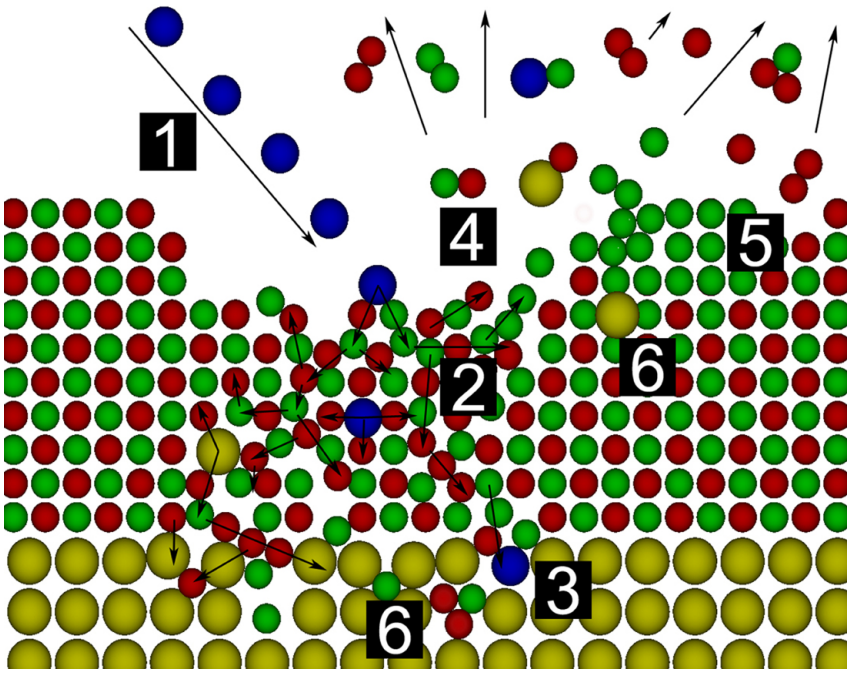

Figure 3.7: Principles of the SIMS technique: The ion bombardment (1) leads to the collision cascade (2) - the incident ions transfer part of their energy to atoms of the sample and set them in motion. They further collide with other atoms and as long as the transferred energy is higher than the binding energy, new atoms are knocked out from their positions. The direct result of the primary ion bombardment is their implantation inside the sample (3). A part of the energy transferred during the collision cascade is brought back to the surface of the sample and atoms and bigger clusters are emitted from the sample (4). Due to the differences in the partial sputtering yield a preferential sputtering may occur - higher probability to sputter one element when compared to the other results in the depletion of the first element in the sample (5). The collision cascade leads also to the sample mixing effect (6) - atoms which were initially not present in some layers can be found there.

while others, for example O_2^+, enhance the formation of cations [225]. Furthermore the ionization probability of the element A is strongly affected by its surroundings. This phenomenon is called a matrix effect and is one of the most challenging problems in the interpretation of the SIMS results. However, the detailed mechanism of the probability of ionization is still unknown.

- Mixing - the direct result of the primary ion bombardment and the collision cascade is the mixing of the sample. Some of the knocked out atoms and primary ions have sufficiently high energy to penetrate the sample for distances as long as several tens of nanometers [226]. This can lead to a significant alteration of the initial composition of the sample (Figure 3.7 - position 6). This effect is strongly visible if the sample consists of several thin, initially well defined layers. The atoms from the upper layers penetrate the deeper layers knocking off other atoms which in turn may travel back to the surface of the sample. This makes it difficult to interpret properly where there is the beginning and the end of a specific layer since the atoms can be detected at the depth where initially they were not present. The penetration depth, as before, depends on the experimental condition, especially on the primary ion energy and the type of the substrate. For soft materials the penetration depth can be a few orders of magnitude higher than the initial thickness of the layer!

Quantitative description

When all phenomena are taken into consideration the final relation describing the SIMS technique can be formulated:

$$I(A^{\pm}) = I_p Y(A)\alpha(A)C(A)\eta \tag{3.8}$$

where $I(A^{\pm})$ and I_p are the secondary and the primary ion currents, respectively, $Y(A)$ is the partial sputter yield, $\alpha(A)$ is the ionization probability, $C(A)$ is the concentration of an element A and η is the transmission and detection coefficient of the tool [228]. Both primary and secondary ion currents can be measured. In order to calculate the concentration of an element A in a sample the partial sputter yield, ionization probability and transmission and detection coefficient have to be determined. This is difficult because all of those parameters depend strongly on the experimental conditions. Furthermore, as it was mentioned above, the exact mechanism of the ionization probability is still unknown and this parameter may differ most significantly when the conditions of the experiment are changed even slightly. Thus, it

is virtually impossible to obtain the chemical composition of a sample based only on the SIMS measurements.

3.2.7.2 Operation modes

Negative and positive modes

As it was aforementioned in the basic description of the sputtering process, emitted ions can be negatively or positively charged, but, as they are further extracted by means of electrical field, it is obvious that anions and cations cannot be detected simultaneously. The sign of an extracting voltage should be set at the beginning of the experiment and thus the detection of only one type of ions will be possible.

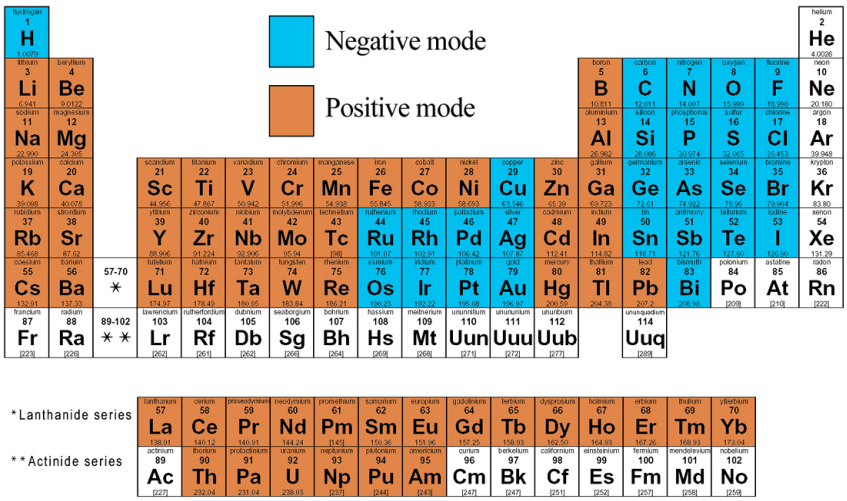

Figure 3.8: Periodic table of elements with preferential modes of detection.

The choice of the detection polarity should be taken carefully as different atoms have different tendency to form anions and cations. Figure 3.8 presents a general suggestion about the mode which is the most suitable for the detection of specific elements. It is important to acknowledge that in many cases both types of ions can be formed, so the picture presents the preferential polarity only and thus a higher intensity of the signal can be expected for this mode. Furthermore, it is also possible to detect compound ions, formed by more that one atom. It can facilitate the detection of elements in a non-preferable polarity. For example it is a common procedure in the negative mode to detect atoms in an oxygen cluster form, e.g. MO^- or MO_2^- if M^- cannot be directly detected.

Surface analysis

As it was already mentioned, the SIMS is a very surface sensitive technique and therefore is an excellent choice for monitoring the morphology of the surface of a sample. Furthermore, it is possible to limit the number of incident ions and therefore a so-called static SIMS can be considered as a semi-nondestructive method. The essential requirement is that statistically the same atomic site of the surface should not be hit more than once and only 0.1–1% of the area of the surface should be subjected to the ion bombardment. It can be achieved if the incoming dose is lower than $10^{12} - 10^{13} ions/cm^2$.

The static SIMS is widely used for surface characterization as the isotopes of trace elements can be detected in ppm concentration, for monitoring of oxidation process and studies of adsorption.

Depth profiling

When the surface of the sample is continuously subjected to the ion bombardment it will lead to erosion of consecutive layers of the sample and thus not only the surface composition, but also the information of the depth distribution of elements can be obtained. The basic principle of a so-called depth profiling is to determine the relation between the secondary current intensity as a function of time.

There are, however, a few complexities associated with the depth profiling. As the crater grows deeper and deeper the accidental sputtering from the edge regions may result in detecting of atoms from a broad distribution of depths, not only from the bottom of the crater as desired. The edge sputtering may significantly reduce the legibility of the measurements.

Furthermore, to sputter effectively a large number of atoms (as the whole layers should be removed) the incident fluence should be increased. This, however, will result in a high mixing effect, which, in turn, can make it difficult or even impossible to obtain reliable results, as it would be impossible to distinguish whether some elements were present in a specific layer before the experiment or were driven here during the collision cascade.

To overcome those problems a new mode of operation was proposed - the dual beam mode. The basic principle is presented in Figure 3.9. One of the beams is called the sputtering beam and the other the analyzing beam. The only task of the sputtering beam is to remove consecutive layers of the material. The energy of incident ions is relatively low, usually not higher than 2keV and therefore the energy is dissipated relatively fast as it is soon not high enough to overcome the binding energy[224, 227]. The collision cascade is very limited and as a consequence the mixing effect is small. On the other

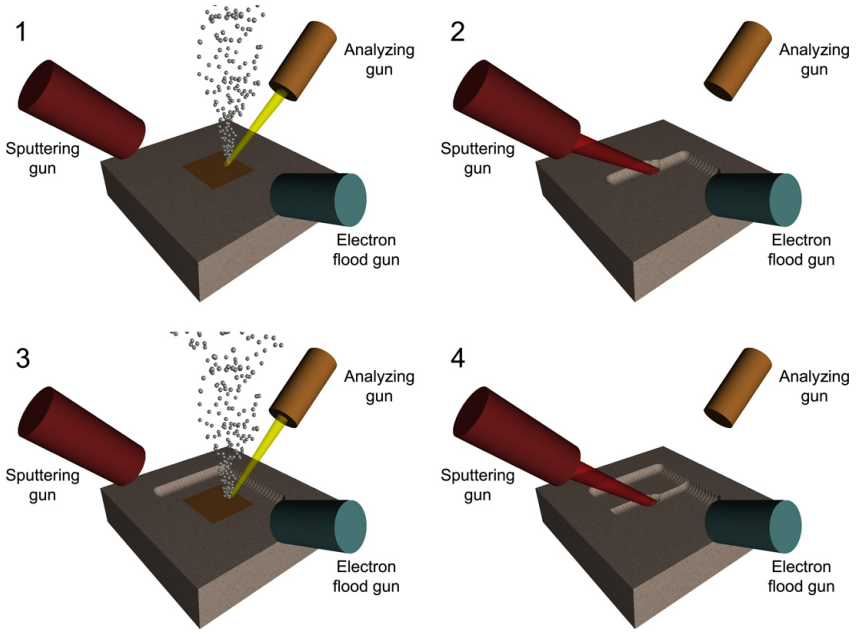

Figure 3.9: Dual beam operation mode: 1) The surface of the sample is analyzed (detector on). 2) Sputtering beam is rastered to form a square crater (detector off). 3) The bottom of the crater is analyzed, measurements are performed on the center of the crater to avoid the rough edges (detector on). 4) Deepening of the crater (detector off).

hand the fluence is very big (ion dose often higher than $10^{17} ions/cm^2$). This assures that virtually every atom that forms a monolayer of the material is sputtered away. This method is often called a dynamic SIMS.

The sputtering beam is rastered and used to create a crater with a flat bottom and and with a side in a range of several hundreds of micrometer. During the sputtering beam operation the detector is switched off because the high current of the incoming beam in most cases (except for conductors) may lead to the charging of the sample, which makes it more difficult and often even impossible to detect sputtered ions. After the sputtering the electron flood gun compensates the charges [233]. Sometimes the charging effects are so high that it is impossible to analyze the sample directly after the sputtering. The system has to wait several seconds before the analyzing beam and the detector are switched on. This method is called a non-intercalated depth profiling. It allows overcoming virtually all charging problems but is time-consuming.

When the sputtering beam is finally switched off, the actual measurement

is performed with the help of analyzing beam which is rastered on the middle of the crater and therefore the negative influence of the crater edges can be overcome. The analyzing beam, in contrary to the sputtering one, has a very low fluence (similarly to the static SIMS), but the incident ions have high energy (25keV or even higher). The collision cascade will be significant and therefore a lot of species will be emitted from the surface of the sample and analyzed in the detector. The low current (in a range of $1pA$) prevents the charging of the sample and even though the collision cascade is dense, the mixing of the sample will not be significant as the number of ions is very limited.

The depth profiling involves an alternative use of beams: at the beginning the surface is measured with the analyzing beam, than the uppermost monolayer(s) is removed with the sputtering beam and the surface of the crater can be measured again. Repetitive performance of this procedure will deliver the information about the depth distribution of elements.

3.2.7.3 Experimental setup

Figure 3.10 presents an overview of the IONTOF ToF-SIMS 300R setup, the tool which was used in the following experiments. The sputtering and analyzing guns focus beams of ion on the sample. The electron flood gun provides the charge compensation for samples which are susceptible to charging during the primary ion bombardment. The extractor accelerates all ions to a common energy. Ion mirrors (a series of electrodes onto which an electric field is applied) increase the measurement resolution by minimizing the spread of the ion energies.

Detector

The basic principle of the SIMS method was described above. The detection of ions was mentioned several times, but this subject was not discussed in details so far. There are many types of ion detectors, the most common are the electric, magnetic and the Time-of-Flight (ToF) ones. The latter one was used in the experiments.

The general principle of the ToF detector is a measurement of the time that ions need to travel the distance between the sample and the detector. The moment when an ion hits the detector can be easily determined, but the accuracy of the method requires that the emission time is specified as well. Therefore the ToF-SIMS uses very short pulses of the primary ion beam. All ions that are emitted from the sample come through the extractor where they are accelerated to common kinetic energy in a constant electrical field. The velocity of ions depends on their mass. The final formula can be derived

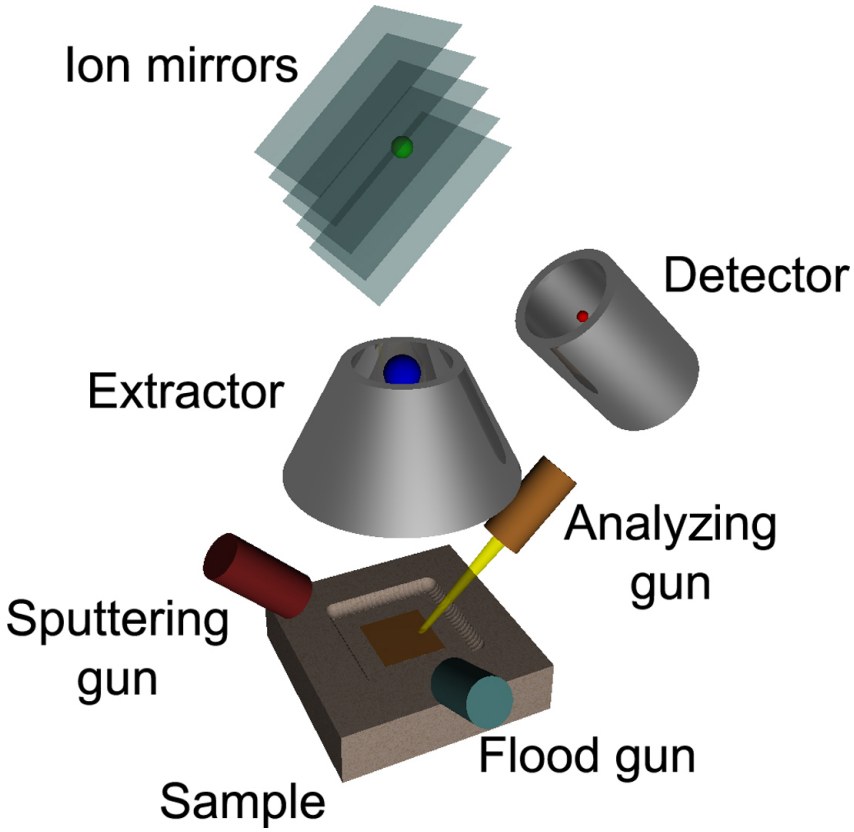

Figure 3.10: The ToF-SIMS setup.

from two following relations:

$$v = \frac{L}{t} \tag{3.9}$$

where v is the velocity of the ion, L is the distance between the sample and the detector, t is the time that is needed for the ion to reach the detector; and

$$qU = \frac{mv^2}{2} \tag{3.10}$$

where q is the ion charge, U is the accelerating voltage and m is the mass of the ion. The resulting expression reads

$$\frac{m}{q} = \frac{2Ut^2}{L^2} \tag{3.11}$$

It means that the detection is not based on the mass of the incoming ion but rather on the mass to charge ratio.

The ion detector typically consists of a microchannel plate detector. Unfortunately it is not free of the common detector drawback which is called a dead time of a detector. After the ion detection there is a certain time during which no additional ion can be detected. In practice it means that when an ion hits a detector there might be one or even more additional ions that hit it again directly afterward, but could not be detected due to the dead time of the detector. The software installed at the tool has an implemented mathematical formula that should decrease this problem. The detector is rastered to a specific, user controlled number of pixels. The software records the number of pixels that have been hit by incident ions and those which were not. Then, using the Poisson distribution formula, it assumes that some of the pixels have been hit not once but twice or even more times. This correction works quite well but only to some extent. The Poisson distribution is based on the number of pixels that have not been hit and if there is only few of them, then the formula starts to be inaccurate. In the extreme situation, when all pixels have been hit, the software has no information on how to proceed with the correction. This kind of a problem is called a signal saturation - at some point the Poisson distribution will lead to confusing results and therefore cannot be used. There are three possibilities to overcome the problem:

- Increase the number of pixels and thus the sensitivity of the detector. However, the more pixels are used, the more time-consuming a measurement becomes. For a standard raster size 128 x 128 pixels it took around one second to acquire a single ion image of the surface of the sample. For the biggest raster size, 2048 x 2048 it could take up to several minutes. This can be acceptable for surface scan but not for the depth profiling.

- Decrease the time slit of the detector and therefore the number of ions that undergo the analysis. The drawback is that the intensity of all signals will be reduced and therefore some of them will be below the detection limit and the valuable information about the sample will be lost. This affects particularly the trace elements.

- Use a less abundant isotope or a cluster ion for analysis. This method is considered to be the best, but also has small drawbacks as not every element has several stable isotopes and the analysis of clusters is usually less transparent as the intensity depends on both elements.

As an example of a problem a silicon signal coming from the Si substrate can be presented. For a standard raster and slit size the silicon signal is almost

always saturated. To avoid the problem the sensitivity of the detector should be drastically decreased, but it will result in losing the information about other, less intensive signals and thus in most cases it cannot be accepted. Another solution it to increase the raster size (in this case only the biggest settings prevent the saturation), but it is time-consuming and often useless as the important properties of a layer can be acquired using different signal, for example other isotope like ^{30}Si which has much smaller abundance and thus the signal is not saturated.

It is also important to realize that the signal can be saturated in one region but be trustworthy in another. In the following experiments the diffusion of Si from the substrate was investigated. The Si^- signal was saturated in the substrate but was successfully quantified in the thin film region where only relatively small amounts of Si were present. It was not proper to use the $^{30}Si^-$ signal as its intensity was below the detection limit in the thin film region.

The main advantage of the ToF detector is a possibility to detect simultaneously all ions and clusters with masses even up to $10000u$, but not just a few chosen ones as it is common in the other detector types. Furthermore it has a superior accuracy with the mass resolution $\frac{m}{\Delta m} > 10000$.

Ion mirrors

The major problem of the ToF detector is the fact that ions are not emitted exactly at the same time nor have the same energy. This leads to the broadening of the recorded peaks. To overcome this effect a system of ion mirrors are used - ions with higher energies penetrate mirrors deeper and the travel time difference with respect to the less energetic ions is reduced. This simple method significantly increases the resolution of the ToF detector.

Analyzing and sputtering conditions

In the following experiments both negative and positive modes of detection were used. Table 3.1 summarizes the information about the analyzing and sputtering conditions that was used in the experiment. As the charging effects were not significant, the depth profiling was performed in the intercalated mode, without the electron flood gun.

However, the shape of the crater created by the sputtering beam could have significantly influenced the measurement if it had been irregular or round-shaped. AFM imagining was performed to exclude this possibility and Figure 3.11 presents a line scan through the center of the crater. Due to the drastic change of height regions close to walls of the crater should be treated as a very rough estimation. A detailed imagining of a wall of the crater was also performed but it did not show any anomalies and was not important for

	Analyzing gun both modes	Sputtering gun negative mode	Sputtering gun positive mode
Ion species	Bi^+	Cs^+	$O_2{}^+$
Raster size	70μm x 70μm	400μm x 400μm	400μm x 400μm
Ion energy - current	25keV - 0.7pA	250eV - 8nA 500eV - 35nA 1keV - 80nA	 500eV - 70nA 1keV - 190nA

Table 3.1: Parameters of the primary and secondary beams used in the experiments. This typical setup was used in all measurements if not specified otherwise.

following experiments. The most important conclusion was that the center of the crater, at least 300μm x 300μm, was flat and its roughness was only slightly higher the roughness of the whole sample. Since the raster size of the analyzing beam was still much smaller than that area it was concluded that a proper aligning of the beams would not be a challenging task.

For some test experiments analyzing beam was aligned in such a way that its edge was very close to a wall of the crater. It was noted that it had significantly influenced the measurements, namely peaks in mass spectrum had been much broader. To exclude even the smallest possibility of the influence of the crater edges on the measurement it was assumed that only measurements where the analyzing beam would be at least 50μm away from the edges of the crater would be evaluated.

3.2.7.4 Data evaluation

Measurement reproducibility

It is important to stress that the following calculations were not based on a single measurement. For each operation mode, the incoming ion energy and the current there were at least ten (for some cases more than fifty!) depth profiles obtained. The reproducibility of all of them was found to be almost perfect. This constitutes a very strong proof that the diffusion process was properly described and the obtained results are trustworthy.

Interpretation

The interpretation of the ToF-SIMS measurements is a very challenging task and often more time-consuming than the actual experiment. It is tempting to accept the first conclusions as a credible, especially when they seem to confirm the assumed theory. Such an approach is potentially dangerous and may lead to confusing results and therefore is not acceptable. The confirma-

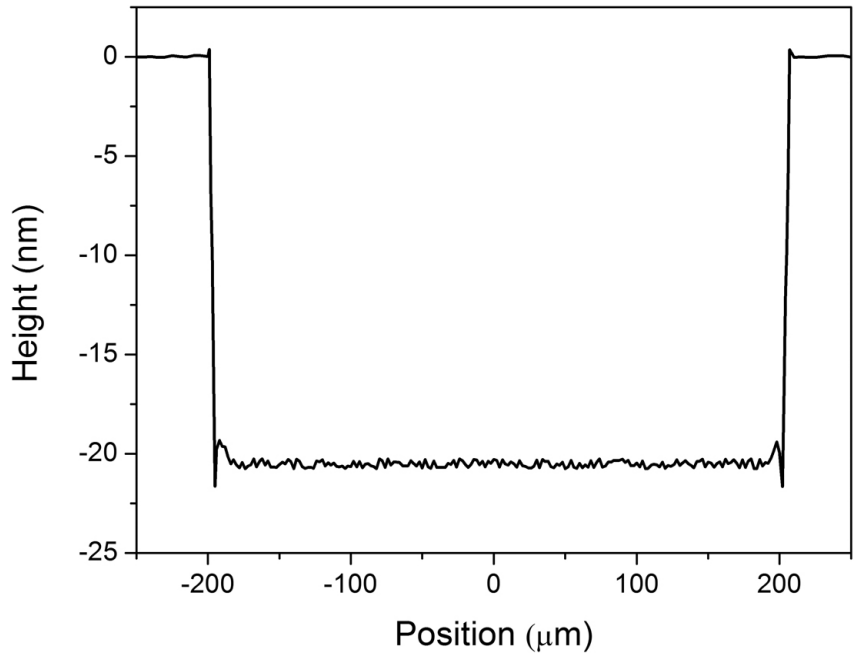

Figure 3.11: AFM line scan of the center of sputtered crater. Even though the accuracy of the imagining close to the edges of the crater is not very good it can be concluded that the center of the crater is flat and its roughness will not significantly influence ToF-SIMS measurements.

tion procedure is rather long and complicated but has to be carried out in order to be sure that the results are describing the physical phenomena (but not artifacts) as accurately as possible.

The problems occurring during the ToF-SIMS measurement can be divided into several main groups and each of them should be treated separately.

1. Ion identification - the basic problem arises from the fact that the Time-of-Flight detector provides the information about the mass to charge ratio (see Equation 3.11), not the mass only. Furthermore, cluster ions may have similar mass to that of other clusters or singular ions. And thus a problem with ions reaching the detector at the same time may occur. For example NO^- and $^{30}Si^-$ or $C_2H_4^-$ and Si^- ions have both the same nominal mass: 30u and 28u, respectively. A similar situation is with $SiOH_2^{2+}$ and Na^+. They are both recorded as 23u (the former cluster ion has the mass twice as the latter, but also the charge twice as the latter, so they both reach the detector at the same time). However, the actual mass (and as a result the mass to charge ratio as well) is

slightly different for those specific ions. The ToF detector has a very high mass resolution and most of those peaks can be resolved. However, it is a user task to distinguish them properly. The software provides very useful hints: it shows how good the estimation is by calculating the two following parameters:

- Deviation - expressed in ppm shows how well the ion mass matches the theoretical position.
- Explained - expressed in percentage. It is an elaborated formula that compares the intensity of other peaks in the spectrum to see what is the probability that the attributed ion is correct. For example if the $^{30}Si^-$ ion is considered, then there should be a peak corresponding to the $^{29}Si^-$ and $^{28}Si^-$ as well, each with the intensity corresponding to the abundance of those isotopes.

Those two parameters are very helpful, but it is the user who has to make a final decision. It is extremely rare that both parameters are perfect. This problem is more challenging for higher masses as there are more clusters which might have similar weight. Nevertheless with some experience ion identification is neither difficult nor time-consuming.

It can however be more complicated if a significant peak broadening is present. As it was clearly stated before, the ion peaks in the spectrum have finite widths. Sometimes, especially for heavier elements and clusters, the width is so broad that it overlaps with other ion or even several ions. In this case a proper ion identification is not possible as the problem is not related to the user's skills but rather to the tool itself as the ion mirrors cannot reduce the peak width properly. This effect is strongly visible for samples which suffer from the charging problem as it broadens peaks in the spectrum. To overcome this problem an additional charge compensating device (flood gun) and/or a non-intercalated mode of measurement should be used.

In those particular experiments only the light elements were considered and therefore problems with the ion overlapping and thus with the identification were virtually not present at all.

2. Depth calibration - As it was clearly stated in Section 3.2.7.1, the direct interpretation and quantification of the obtained results is not possible, nevertheless there are several methods to overcome the problem.

   At the beginning of the quantification process it should be acknowledged that from a single depth profile only a general distribution of

elements with a roughly estimated depth of their presence can be acquired. The SIMS technique cannot directly relate the measured sputtering time with the distance units and therefore a proper calibration is required. It might seem to be relatively easy, but one has to be aware that it is still an approximation and sometimes the perfect depth distribution of elements cannot be obtained. There are two basic ways to calibrate the profile, each has its strengths and drawbacks:

- Measurement of the crater depth using e.g. a profilometer. In this case the calibration seems to be straightforward: the ending point of the profile is attributed to the measured depth. Unfortunately different materials might have significantly different sputtering rates which can results in a large calibration error. To overcome this problem one can measure the sputtering rates for different materials separately and thus create a proper standard for the depth quantification. This is a time-consuming method as the sputtering rate needs to be calculated for all different ion energies separately, but once standards are established they can be used any time they are needed. Unfortunately it would be time-consuming and virtually impossible to create standards for all different types of samples and therefore it is usually assumed that similar samples have the same sputtering condition. For example if a set of samples differing only in annealing temperature is examined it can be assumed that the sputter rate remains constant. However, crystallization, densification or diffusion of some impurities which may take place at elevated temperatures can significantly change the sputtering properties of the sample and therefore it should be always checked whether the constant sputter rate assumption is valid.
- Measurement of the layers thickness. Knowing the exact thickness of each layer in the stack it should be easy to make the depth calibration. The problem is that individual layers cannot be easily separated in the depth profile due to the mixing effect. It will be always more or less arbitrary to set the end of one and the beginning of the other layer. It is important to use the same definition (e.g. when a specific signal drops to the half of its initial value) every time.

To increase the depth calibration accuracy both methods could be combined to see how well they match. In the following experiments both methods were successfully used.

3. Concentration calibration. As it was discussed in Section 3.2.7.1, the intensity of the SIMS signals depends strongly on the experimental conditions and even the slightest change of any parameter (e.g. the ion energy, or the incidence angle, or the sample composition) may significantly influence the outcome result and thus the concentration calibration is far more complicated.

   The consideration should always start with the qualitative comparison of the depth profile to the reference measurement. It is possible to obtain some valuable information, but only to some extent, provided that a reference measurement was performed on the sample with a similar sputtering conditions. A good example is a dopant profile of two samples doped with the same atoms but with a different dose and energy. If the substrate is the same (e.g. Si) such a comparison is possible and the information about which sample is doped higher can be acquired. However, if one of the samples has a different substrate (e.g. GaAs) this comparison is not possible due to the matrix effect. Hypothetically, in extreme situation it may happen that the slightly higher dopant concentration will significantly change the matrix, but fortunately such a situation is very rare.

   To perform the quantitative calibrations a suitable standard has to be created - samples with known concentration should be analyzed by the SIMS and the relative sensitivity factors (RSF) should be calculated. It is defined as follows:

$$RSF_{A_R} = \frac{C_A}{C_R}\frac{I_R}{I_A} \tag{3.12}$$

   where RSF_{A_R} is the relative sensitivity factor for element A with respect to the reference R, C_A and C_R are concentrations of element A and R, respectively, I_R and I_A are the secondary ion currents for elements R and A, respectively. The major element is usually used as a reference. In many cases only traces of element A are monitored and therefore it can be assumed that the concentration of the reference element is constant. A more convenient RSF can be defined as:

$$RSF_A = RSF_{A_R} * C_R \tag{3.13}$$

   Then the concentration of an element A can be derived as:

$$C_A = RSF_A\frac{I_A}{I_R} \tag{3.14}$$

   However, this method is not always faultless. As it was mentioned, the matrix effects may significantly change the ionization probability and

thus the secondary ion currents which practically means that the RSF is not a constant value, but depends on the composition of the sample. The quantification is trustworthy for homogeneous samples, but a proper calibration for more complex samples is always a challenging task especially for surfaces and interfaces between layers with different compositions where the matrix is drastically changed. Alas, it is the interface which is usually the most interesting region in the sample to examine. Serious miscalculations may occur if the matrix effects are not taken into consideration. Unfortunately, there is no universal method to overcome this problem, in most cases the quantification will not be possible if strong matrix effects are encountered.

Except for the matrix effects, the analysis of the interfaces may bring about an additional problem: it may happen that two different materials have a distinct susceptibility to charging. This usually results in a rapid change of the SIMS signals which does not correspond to the change of the concentration, but is a measurement artifact. The best example is the conductor/insulator interface where a drastic change of charging conditions can be observed. It makes it very challenging issue since the interface regions are very important for a proper quantification, especially for the depth calibration. Unfortunately there is no unquestionable mean to overcome the problem. The surface and the interfaces of the examined sample have to be treated very carefully to distinguish the real features from the SIMS artifacts.

4. Measurement stability - At the beginning of the experiments the tool was found to be very unstable. It was down more than a half of the operation time. Moreover, even when it was possible to acquire some measurements, many of them were unstable. Figure 3.12 presents some examples of such profiles. The black curve shows a very noisy measurement. An example shows an extreme situation when the disturbance affects even the region where the signals drops to zero. In this case no information can be acquired from the profile and the experiment had to be repeated completely. The red and blue curves seem to be similar: in both cases there is a disturbance in the intensity of the signal. It is very short, actually it affects only one or a few data points. The difference is that in the case of the red curve the intensity goes back to the initial value, while it is not the case for the blue curve. It can be concluded that in the case of the red curve there was some fluctuation of the primary ion current, while in the case of the blue curve the disturbance most probably affected the detector and therefore the intensity did not come back to a normal value. Usually such a mea-

surement has to be repeated except if only the qualitative information was required. In the case of the red curve the quantitative analysis can be performed as the artifact can be manually corrected. Nevertheless in some situations, namely when the artifact appears in the most interesting region, e.g. the interface between layers, it is advisable to repeat the measurement. An important fact is that those disturbances usually affected all signals in the profile. Fortunately, after some repairs the tool was fully operational and no longer unstable. The following measurements were performed after the initial problematic period and no unstable measurement was ever taken into account during this work.

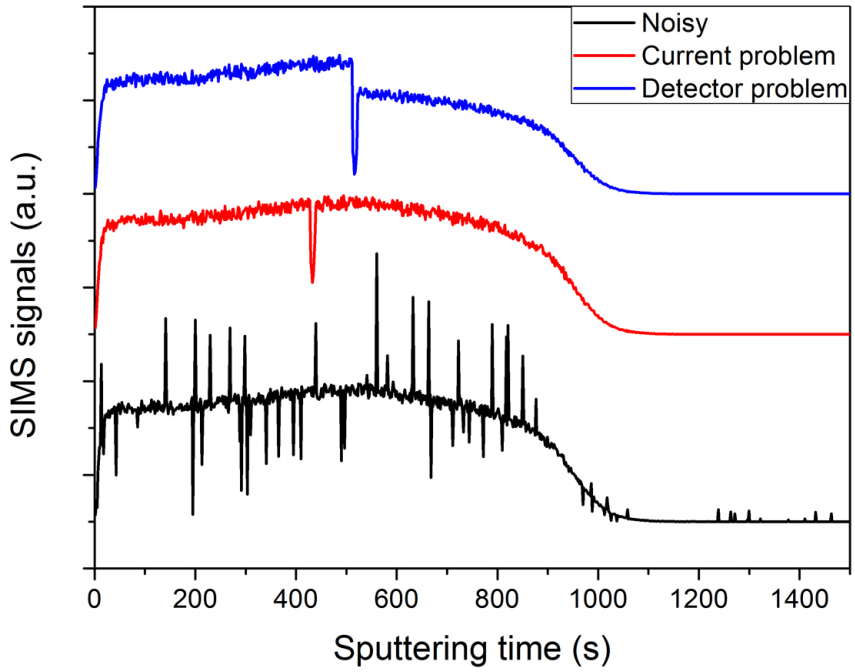

Figure 3.12: Some examples of unstable measurements. Black - a very noisy signal, the experiment has to be repeated. Red - a short fluctuation in the primary ion current, profile can be quantified if the artifact does not affect a crucial region, e.g. interface. Blue - a detector disturbance, only the qualitative information can be obtained.

There is another problem concerning the stability of measurements. Even if the same sample is measured twice it is very often that the intensity of all signals differs slightly, especially when the second measurement was performed some days later, in which case it is impossible to provide exactly the same measurement conditions (ion current, pres-

sure in the chamber etc.). To overcome this problem signals should be normalized. In the following experiment the reference was a ^{30}Si signal coming from the Si substrate. Therefore for every SIMS measurement presented in this work the intensity of all signals will be relative and presented in arbitrary units. Furthermore it is necessary to mention that in most measurements the intensities of ^{30}Si (for Si substrate region) and Al and O_2 (for thin film region) signals were found to be very similar (see Figure 4.2) and it may seem that they were simply normalized. It was, however, purely coincidental and therefore it is important to remember that the actual reference signal is defined as ^{30}Si signal coming from the Si substrate.

It is very important to stress that all stability problems described above concern the analyzing beam. The case of the sputtering beam is different. The tool that was used in the experiment has a very powerful feature - the automated sputtering current control. The user specifies only the desired value and the machine takes care to fulfill this condition. For the tools which require the user to adjust the sputtering current manually the fluctuation can reach even 5% between the measurements. With the automated control the fluctuation is more than an order of magnitude better. It ensures that the sputtering rate and thus the time scaling of the profile has an extreme good reproducibility. It is very important in this kind of measurements because sometimes the production procedure differs slightly - only a few tens of degrees of Celsius or a few seconds in annealing time. Without the automated current control those differences could not be resolved. This was tested on another tool without this feature and the results were very poor. It can be even stated that without the automated current control this experiment could not take place.

5. Beams misalignment - The analyzing beam needs to be centered in the crater made by sputtering beam. Unfortunately sometimes during the measurement beam misaligns and the analyzing beam starts to measure some part of the crater edge or even a non-sputtered areas. It can significantly change the obtained depth profile and therefore after each measurement the position of the sputtering and analyzing beam (both recorded by the software) has to be compared to exclude such a possibility. Otherwise the measurement has to be repeated.

6. Ion induced thermal effects - for sputtering beam the ion dose is relatively high (often higher than $10^{17} ions/cm^2$) and therefore ion bombardment may increase the temperature of sample and thus activate

the diffusion process. Fortunately in the following experiments this effect was found to be negligible small. The intensity of the normalized Si^- was compared for different sputtering energies (and thus doses) and was found to be the same for each energy.

7. Samples aging - It is not always possible to measure the full sample set at once, which would be the best. The reason is that sometimes the tool was down or used for different purposes. Furthermore some samples were manufactured later to fulfill specific conditions, often as a result of conclusions driven from previous measurements. This caused the problem that samples were measured after different aging time. Sometimes it may be crucial, for example a metal material may oxidize and change the outcome of the profile. Fortunately no significant change because of aging was noted in the following experiment. The same sample was measured again after several months from the first experiment and the results were compared. The only difference was the higher contamination level in the second experiment, but it was located only on the surface and therefore does not influence the quantitative analysis.

8. Different preparation conditions - As it was stated above, not all samples were fabricated at the same time and therefore the conditions were slightly different. Furthermore some of the samples were kept in the Clean Room environment while the others were exposed to air. It could somehow change the depth profiles. Fortunately the only difference that was found was a various contamination levels, but, as it was always very low, it did not affect the sputtering conditions in any way. Furthermore an additional experiment was done with a sample that was re-measured after long exposure to air. Again, no significant difference was found except for a higher concentration of contamination on the surface.

Chapter 4

Results and discussion

4.1 Basic characterization

The basic properties of alumina are well known and characterized. The thermally induced crystallization and compaction of the material has been reported [235–237] and will be briefly summarized in this section. It will serve as a background for further detailed discussion about the diffusion process that occurs in alumina during the RTA.

4.1.1 Crystallization

It is obvious that during the thermal treatment the structure of the sample may alter as the sample crystallizes during the process. It may significantly influence the diffusion process, so before any detailed calculations can be performed, the information about crystallization has to be acquired. The sample set was investigated by the GIXRD. It was found that samples annealed in temperatures above $900°C$ are in the crystalline η-Al_2O_3 phase (see Figure 4.1).

4.1.2 Compaction and densification

The thickness measurements were performed by the ellipsometry and the XRR and the results were found to be the same for both techniques. The latter method provided also information about the sample density. Both parameters are presented in Table 4.1. Measurements provided an additional proof of the location of the transition point around $900°C$: it is expected that during the crystallization samples densify and thus reduce their thickness. Indeed, the biggest change of the sample thickness and density is

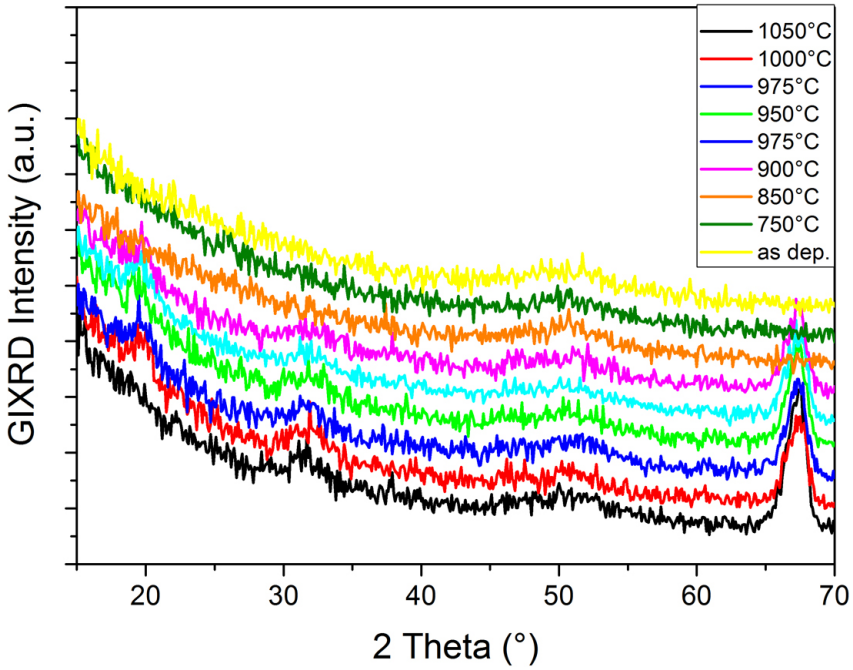

Figure 4.1: The GIXRD measurements reveal that samples samples crystallize in the η-Al_2O_3 phase at the annealing temperatures above $900°C$.

observed between $850[°C]$ and $900[°C]$ which corresponds to the GIXRD measurements.

It is, however, important to emphasize that both processes, crystallization and diffusion, occur simultaneously and both of them can have an impact on the density and the thickness of the sample. Therefore a relative change of the density is higher than a relative change of the thickness because, as it will be shown in following sections, samples do not crystallize as monocrystalls but rather have a polycrystalline structure; as a consequence some material can be accumulated in grain boundaries (and thus increase the density of the whole sample) without or with minimal influence on the thickness.

Most of the further analysis will have to be performed separately for the crystalline and amorphous phases.

4.2 ToF-SIMS depth profiling

Figure 4.2 presents a typical negative mode ToF-SIMS depth profile for the sample annealed at $1000°C$ for 20 seconds including an additional reference signal (Si^-ref) representing the silicon intensity for an as-grown sample. The

Annealing temperature $[°C]$	Thickness $[nm]$	Density $[g/cm^3]$
1100	14.5	3.92
1050	14.6	3.91
1000	14.6	3.84
975	14.6	3.84
950	14.6	3.84
925	14.6	3.83
900	14.7	3.83
850	16.0	3.11
800	16.0	3.01
750	16.0	2.97
700	16.0	2.87
650	16.1	2.85
as-grown	16.2	2.73

Table 4.1: The thickness and the density of samples annealed in a wide range of temperatures. The densification and thus the shrinkage of the samples as a result of crystallization is present for temperatures above $900°C$.

qualitative analysis reveals a diffusion of Si from the Si substrate through the Al_2O_3 thin film during the RTA which leads to a segregation of Si on top of the alumina layer surface. The amount of Si that is found inside and on the surface of the sample depends strongly on the annealing temperature and time. The depth profile may be divided into three separate regions: (i) a thin top layer indicating surface segregation of Si, (ii) the alumina thin film with a Si concentration gradient, and (iii) the interface to the Si bulk substrate towards which the concentration increases rapidly. The definition of the regions is arbitrary but the same procedure should be applied to all obtained profiles. The end of the surface layer was defined at the local minimum of the Si^- signal and the interface between the thin film region and the substrate - at the point where Al^- signal is decreased by half.

4.2.1 Quantification

Qualitative analysis provided valuable but incomplete information. To describe the diffusion process properly, the diffusion parameters should be determined and thus a proper quantification of the depth profile is required. As it was discussed in Section 3.2.7.1 and further treated in Section 3.2.7.4, the direct quantification of the SIMS results is not possible. It can be, however, accomplished by means of a relative sensitivity factor (see Equations 3.12 -

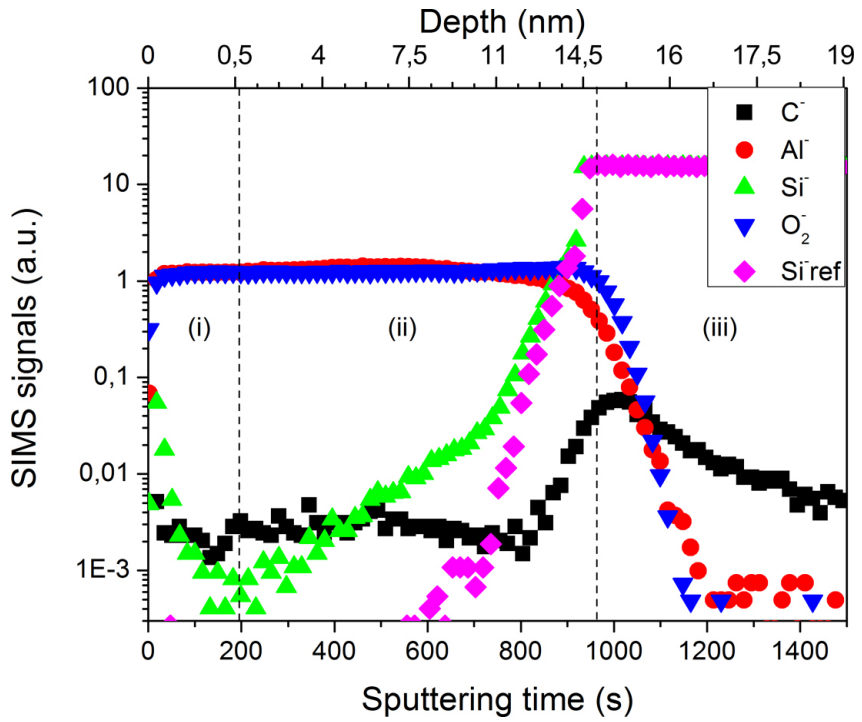

Figure 4.2: A typical depth profile for the sample annealed at 1000°C for 20s. All presented ions are singly ionized and each element refers to the most abundant isotope. Three regions can be identified: (i) a thin top layer indicating surface segregation of Si, (ii) the alumina thin film with a Si concentration gradient, and (iii) the interface to the Si bulk substrate. Si^-ref shows the intensity of Si^- signal for a non-annealed sample. Sputtering rate is significantly different for each region and therefore the depth scale was adjusted for each region separately.

Al:Si pulsing ratio	Si atomic percentage ($at\%$)	x in $Al_{1-x}Si_xO_y$
6:1	1.3	5.0
5:1	2.9	10.3
4:1	3.6	12.4
3:1	4.5	15.5
2:1	5.4	18.7
1:1	8.5	28.9
1:2	11.9	41.3
1:3	13.9	49.7
1:4	15.7	56.0

Table 4.2: Silicon atomic percentage for as-grown samples with the Al to Si precursor pulsing ratio varying between 6:1 and 1:4, as obtained from XPS.

3.14).

An attempt to determine the RSF for the Si^- signal was performed. As it was discussed in Section 3.1.1 the composition of the $Al_{1-x}Si_xO_y$ was varied by adjusting the Al to Si precursor pulsing ratio between 6:1 and 1:4. The Si atomic percentage of as-grown samples was determined by the XPS measurements. However, there was a certain probability that the surface contamination may significantly influence the measurement and hence an additional measurement was performed: a low energy sputtering has been used to remove several nanometers of a thin film (the side of the crater was about $1mm$) and the XPS measurements were performed on the bottom of a crater shortly afterward. The second measurement did not show any discrepancies. The result is presented in Table 4.2. Furthermore, all measurements were performed in vacuum and therefore the possibility of the contamination was limited.

Then, the intensity of the Si^- signal was compared to the Si concentration and therefore the RSF was determined. Furthermore, it was assumed that for a small Si concentration it is constant. Figure 4.3 shows the comparison between the ToF-SIMS intensity and the Si concentration. It is clearly visible that up to the concentration of around 10% (which corresponds to $x \approx 0.3$ in $Al_{1-x}Si_xO_y$) the dependence is linear and therefore the RSF is constant. Above that limit the matrix effects start to play a significant role and the quantification would be complex. It is important to stress that the RSF was calculated according to the Equation 3.12 and with the constant matrix concentration assumption (Equation 3.14) and in both cases the RSF was independent on the concentration of silicon if it remains below 10% and was dependent above 10%. Fortunately, the amount of Si that diffused through

the sample during the RTA in those experiments was always low enough to use a straightforward quantification procedure (constant RSF).

4.2.2 Segregation

As it was discussed in Section 3.2.7.4, the ToF-SIMS artifacts are very often present at the beginning of the depth profile and therefore it was not certain whether the Si peak originated from the actual segregation of Si on top of the sample or was just a measurement artifact. Silicon segregation on the surface of high-k materials was reported for Pr_2O_3, La_2O_3 [238] and Pd_2Si [239] but additional measurements were required to deliver an undeniable proof. Unfortunately samples had to be removed from vacuum and cleanroom environment and therefore it was expected that the silicon on the surface would be found in oxidized form. Both, XRR and XPS measurements confirmed silicon segregation on the surface of samples. It was further noted that the amount of Si on top of the sample increased for higher annealing temperatures and therefore it may be concluded that the Si segregation is a real feature, not just a SIMS artifact. The quantitative description of those measurements will be further explained in Section 4.4.3 where surface boundary conditions are discussed.

4.3 Annealing conditions

As it was shown in previous sections annealing leads to the crystallization of samples. This is, however, a complex process and one should expect polycrystalline structure. It is therefore advisable to manipulate the annealing conditions as it may alter the crystallization process and thus provide useful information about the microstructure of samples and perhaps even about the diffusion mechanism. Samples annealed in various atmospheres and with a different cooling rate will be discussed in this section.

4.3.1 Annealing ambients

Standard annealing was performed in an N_2 atmosphere. An additional sample set was created and annealed in various ambients. The annealing time was 20 and 60 seconds, while the temperature was $1100°C$ and $700°C$ for crystalline and amorphous samples, respectively. It was not easy to select the proper parameters, especially for the amorphous phase since at low temperatures the diffusion is moderate and the differences may not be visible if the annealing time is short. Furthermore some experiments showed that

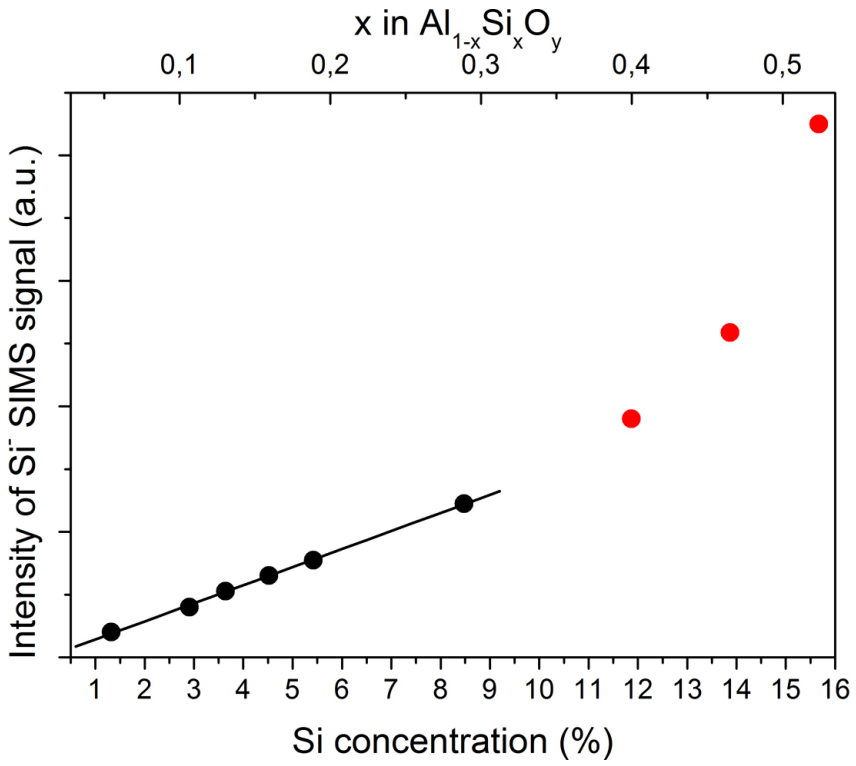

Figure 4.3: The relation between the intensity of the ToF-SIMS Si^- signal and the Si concentration in the sample. For samples with small Si concentration (below 10% which corresponds to $x \approx 0.3$ in $Al_{1-x}Si_xO_y$) the dependence is linear and therefore the RSF does not depend on the concentration of the Si (black dots). In this region quantification is possible. When the Si concentration increases the matrix effects play a significant role and the RSF factor depends strongly on the Si concentration (red dots). Then the straightforward quantification is not possible.

samples annealed for a long time in a temperature slightly below $900°C$ crystallize. Therefore the temperature was chosen to be small to prevent the crystallization, but with a much longer annealing time to allow a significant amount of Si to diffuse into the sample.

Samples were investigated with the ToF-SIMS. Figure 4.4 and 4.5 present the results for the crystalline and amorphous samples, respectively. The difference is clear. In the case of the crystalline phase the annealing ambient has no effect on the diffusion process. Both the top segregated layer and the diffusion gradient inside the thin film are the same for all samples. The only factors that have an impact are the annealing time and the temperature. At that point it is too early to determine the diffusion mechanism, but some conclusions can be formulated. As it was discussed in Section 3.1.2, the rapid thermal annealing process may significantly reduce the number of defects. Particularly, the annealing in the O_2 ambient should decrease the number of oxygen vacancies in oxide materials[240–243] and thus, if the vacancy mechanism was dominant, the diffusion process should be significantly reduced. However, this observation was not made, so that the vacancy mechanism does not appear to dominate in the crystalline samples.

On the other hand, the amorphous samples show higher diversity. Figure 4.5 had to be carefully scaled to show the region of interest and the ambient-related differences. Although the differences may seem small, but the result was reproducible. The diffusion of silicon in samples annealed in O_2 atmosphere is reduced. An interesting fact was noted for samples annealed in two steps, using the O_2 and N_2 ambients. The diffusion is lower for samples annealed for 30 seconds in oxygen and then in nitrogen than for samples with reverse order or annealing. Similarly to the previous consideration, the reduction of the oxygen vacancies can be related to the O_2 annealing. However, it can be clearly noted that the amount of diffused substance is reduced and therefore it can indicate that a presence of the oxygen vacancies may have a significant impact on the diffusion process for amorphous materials. This may lead to a conclusion that the dangling bond mechanism may play a significant role in the diffusion process.

4.3.2 Cooling rate

As it was described in Section 2.3.5, the grain boundary diffusion is a common diffusion mechanism in crystalline samples and therefore the following experiments were designed to investigate this possibility. It was mentioned in Section 2.2.3 that the size of grains in many polycrystalline materials depends on the cooling rate after the thermal treatment and thus a new sample set with varying thermal treatment conditions was created. The basic principles

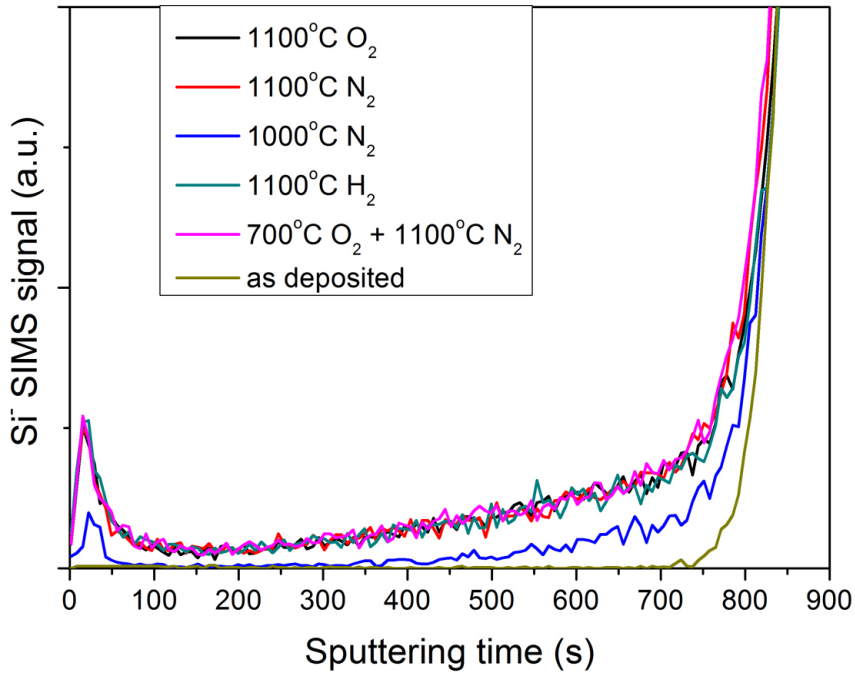

Figure 4.4: The Si^- signal for the samples annealed at $1100°C$ for 20 seconds in different ambients. The diffusion process does not depend on the atmosphere. The additional signal for the sample annealed at $1000°C$ in N_2 atmosphere was added as a reference.

of the experiment can be summarized as follows:

1. Every sample was annealed in a conditions to ensure the crystallization of the sample (if not specified otherwise the annealing temperature and the time were $900°C$ and $20s$, respectively).

2. The cooling rate was different for different samples.

3. The SIMS measurements were performed and the intensity of the Si^- signal was measured on the surface of the sample (region (i) in Figure 4.2) which is proportional to the total amount of material agglomerated on the surface.

4. Each sample was post-annealed, but all parameters were exactly the same for all of them: annealing temperature, the time and the cooling rate.

5. The SIMS measurements were repeated and the relative intensity of the Si^- signal was once again determined.

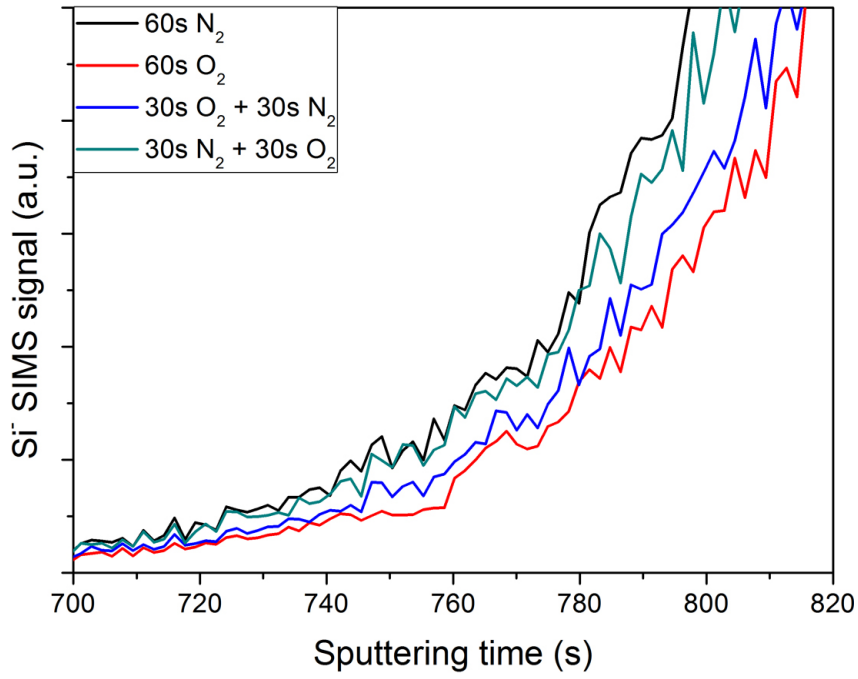

Figure 4.5: The Si^- signal for the samples annealed at $700°C$ for 60 seconds in different ambients. The diffusion process is reduced for the samples annealed in the O_2 atmosphere.

Very interesting observations were made: as it could be expected, for samples without the post-annealing the amount of diffused silicon was higher for samples with lower cooling rates as they were effectively heated for a longer time (see the black dots in Figure 4.6). However, the situation was reversed after the post-annealing at low temperatures (see the red dots in Figure 4.6): more silicon diffused into the samples which had higher cooling rates during the first annealing. The result can be explained by the mechanism of the grain boundary diffusion: samples cooled more rapidly form smaller grains and therefore the grain boundary density (number of boundaries per unit area) is higher. More grains means more high diffusivity paths and therefore effectively more silicon may diffuse into the sample. It would be difficult to explain this phenomenon by means of other diffusion mechanisms.

Furthermore different annealing conditions may change the width of the grain boundary and for bigger boundaries more silicon may diffuse into the sample. This effect, however, may not be confirmed by any of the available measurement techniques. Transmission Electron Microscope or the 3D Atom Probe Tomography (or other similar techniques) is required to check whether

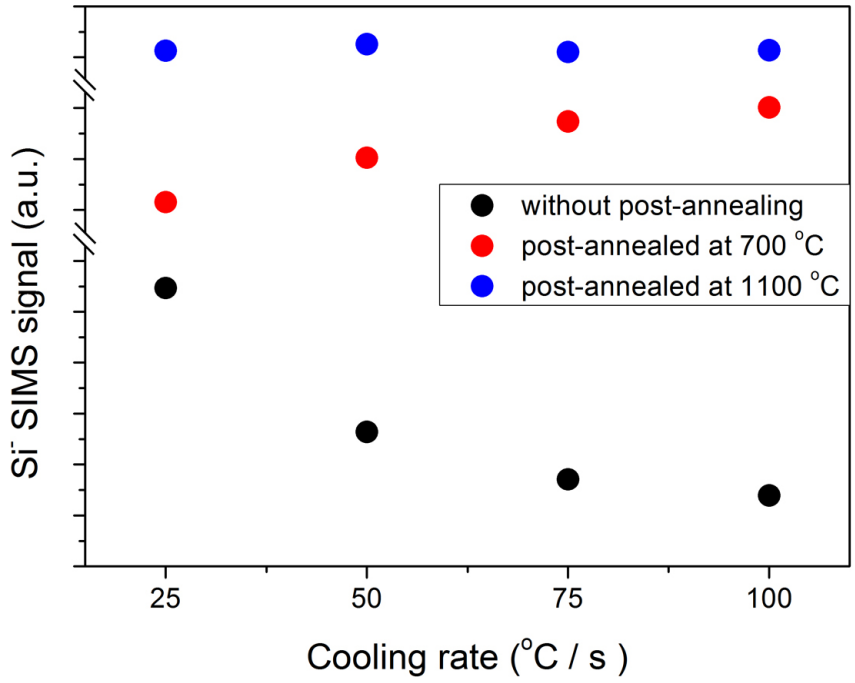

Figure 4.6: The intensity of the Si^- signal measured at the surface of the sample as a function of the cooling rate of the first annealing (annealing parameters: $900°C$ and $20s$). The scale between samples that were subjected to the same annealing conditions is preserved, but the scale between black, red and blue dots is not for a better legibility.

the annealing conditions change the width of the grain boundaries.

There were, however, a few exceptions. If the annealing temperatures and / or time were very low, then the effect was not observed. It is very easy to explain that as for such conditions very limited amounts of Si could diffuse into the sample and hence the difference was not visible.

A more complex situation arose for samples post-annealed in much high temperatures, usually exceeding $950°C$ (see the blue dots in Figure 4.6). In those cases the amount of diffused silicon was found to be almost the same for all samples. Furthermore, the diversity was smaller for samples annealed at higher temperatures and longer times. Once again, the explanation can be delivered: samples post-annealed at high temperatures are subjected to recrystallization and thus formation of a new grain structure. However as the cooling rate for the post-annealing was the same so is the grain boundary density. Thus the amount of silicon which diffused into the sample was also the same. The small diversity may originate from the first annealing, but for

high temperatures and times of post-annealing this effect is negligible.

A similar procedure was applied to amorphous samples but with the annealing temperature always below $900°C$. However, the second SIMS measurement always led to the same conclusion as the first one: more silicon was found in samples which had a lower cooling rate during the first experiment. No exception was observed. It is also very easy to explain: since there is no grain structure, samples with lower cooling rates were effectively heated for a longer time and therefore more silicon diffused into the sample.

4.3.3 Diffusion mechanism

This experiment delivers an additional premise that the grain boundary diffusion is most probably the dominant mechanism in crystalline samples. It is not a direct proof but a strong indication since it would be difficult to explain such a behavior without resorting to the grain boundary diffusion mechanism. It is worth mentioning that the influence of the cooling rate on the grain size is well describe in the literature [244–247] and was reported for various materials [248–251] including thin films samples [252–254]. Furthermore, the influence of the grain size (and thus grain boundary density) on the diffusion rate was also described and reported numerous times in the literature [102, 106, 109–111, 115, 117, 255–258].

4.4 Diffusion model

The qualitative information about the diffusion process was acquired and therefore it is time to continue with the quantitative analysis. However, to solve the diffusion equation the proper boundary conditions should be set, just as it was explained in Section 2.3.2 and further discussed in Section 2.3.5 concerning the limitations of the diffusion process. As the latter section suggested, three regions, namely, the source, the thin film and the surface should be considered. With this information a suitable model of the diffusion can be assumed and the specific solution of the diffusion equation can applied to calculate the diffusion parameters.

4.4.1 Source boundary condition

As it was explained in Section 3.2.7.3, the Si signal coming from the substrate was saturated for the standard detector raster and slit size. To overcome the problem the time slit and thus the sensitivity of the detector was decreased. A valuable piece of information about the diffusion profiles in the thin film

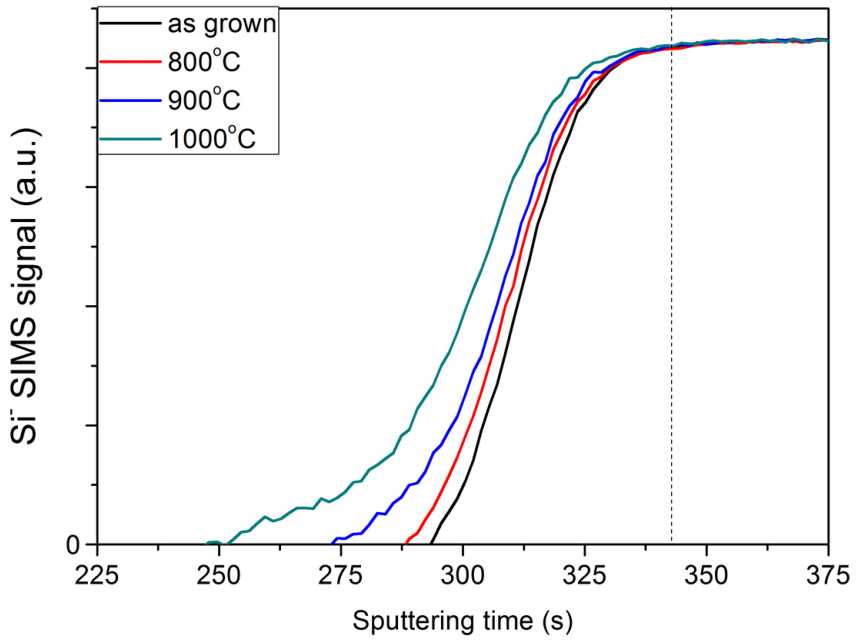

Figure 4.7: The Si^- signals for sammples annealed for $20s$ and different annealing temperatures at the reduced detector sensitivity to avoid the saturation of the signal. Dashed line represents the interface between the source and the thin film region defined, as usual, at the point where Al^- signal is decreased by half (signal not shown for a better legibility). The intensity and thus the concentration of Si at the interface between the source and the thin film region is constant.

region was not obtained, but the measurement allowed to characterize the interface region in detail. Figure 4.7 presents the relevant comparison of the Si^- signals for different annealing temperatures. A straightforward conclusion can be formulated: regardless of the annealing temperature the concentration of silicon is constant at the interface. A similar measurement was performed on samples annealed at the same temperature but for different time. They basically showed the same behavior, so they will not be presented. However, those experiments revealed that the assumption of the constant surface concentration can be applied in the diffusion model.

4.4.2 Diffusion in the thin film region

For the solution of the diffusion equation with a constant surface concentration (see Section 2.3.2) it was derived that the amount of material that

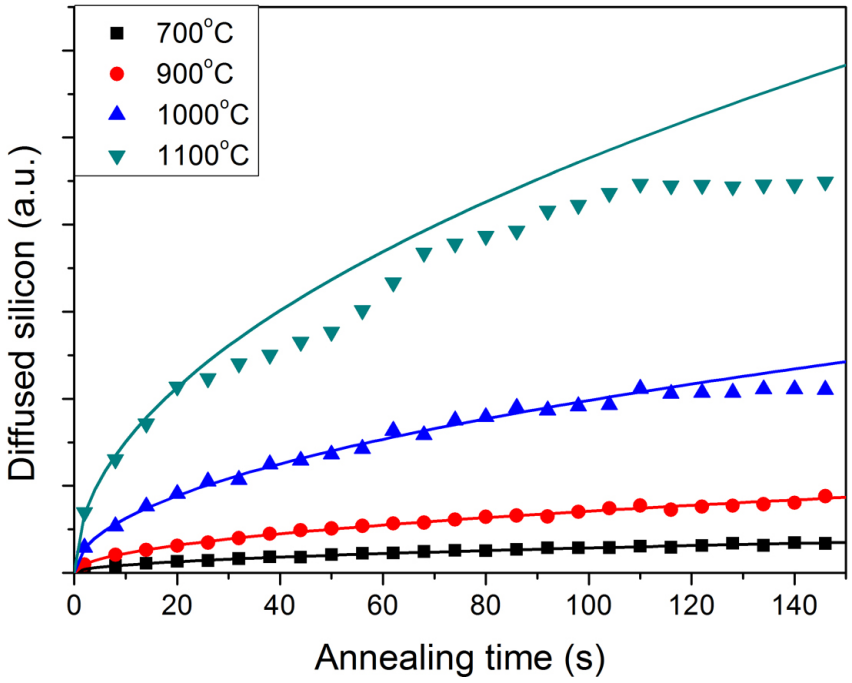

Figure 4.8: The amount of substance found in the thin film region as a function of time. As expected (see Equation 2.60), the square root relation was noted. Symbols represent experimental data and solid lines square root fitting performed on data from range 0 - 20 seconds where no diversion from the expectations was noted. The fit was expanded for the full range.

diffuses into the sample is proportional to the square root of the time (see Equations 2.29 and 2.60) if the diffusion length is smaller than the sample thickness. It is essential to check whether this relation holds. A new sample set was created with varying annealing time, the SIMS measurements were performed, the intensity of the silicon signal was integrated over the whole sample (regions (i) and (ii) in Figure 4.2) and its dependence on the annealing time was plotted in Figure 4.8. For samples annealed at low temperatures no deviation was noted and the amount of diffused material scaled with the square root of time. There were, however, some deviations for higher temperatures. For the highest temperature ($1100°C$) it started to deviate relatively fast, after 20 seconds, whereas for $1000°C$ it took much longer - approximately after two minutes of annealing. An important conclusion should be made: the deviation for all signals (some of them are not presented in the figure) always starts at the same level of relative intensity and thus the total amount of the silicon that diffused into the sample is the same. It would be

further interesting to determine the diffusion length at that point after the diffusion coefficient is calculated (see Sections 4.5.1 and 4.5.2)

The other problem concerning the thin film region is the diffusion limitations. Section 4.3 strongly indicated that the grain boundary diffusion and the dangling bond mechanisms can be dominant in the crystalline and amorphous samples, respectively. In spite of the lack of the direct proof of a specific mechanism it can be concluded that defects play a significant role in the diffusion process. Furthermore, the grain boundary diffusion is highly anisotropic, with the fast diffusion rate along the boundaries and much slower through the grains. It brings a difficulty to the proper interpretation of the obtained results. There might be a lot of diffusion barriers, trap states and even additional sources in the material. However, as it was explained in Section 3.2.7.3, the usual raster size of the analyzing beam was 70μm x 70μm and therefore the average rate of the diffusion will be measured, as an even distribution of defects can be expected. It is confirmed by the reproducibility of the measurement. It is justified to assume that a simple solution of the diffusion equation (as presented in Section 2.3.2, Equation 2.52) can be applied. However, it should be acknowledged that the derived diffusion parameters would describe the average diffusion conditions in the sample. It would not be possible to attribute it to a specific diffusion mechanism, e.g. the grain boundary diffusion.

4.4.3 Surface boundary condition

4.4.3.1 Time dependent relation

As it was already discussed in Section 4.2, the segregation on top of the sample is a real feature not just a measurement artifact. The proper analysis of this region is required to gain a valuable piece of information about the type of the surface boundary, just like it was described in Section 2.3.5. The dependence of the amount of silicon found on the surface on the annealing time was investigated by the ToF-SIMS and the result for both the crystalline and amorphous phases is presented on Figure 4.9.

In the amorphous phase the amount of silicon that is found on the surface is very small and is not significantly changed with the increase of the annealing time and temperature. In most cases it was slightly bigger for higher temperatures or times, but there were contrary examples as well. What is most important is the fact that it was always very small and therefore may be attributed to the surface contamination and therefore it can be concluded that the surface segregation of Si is not present for amorphous samples.

In the crystalline phase, however, the amount of silicon found on the

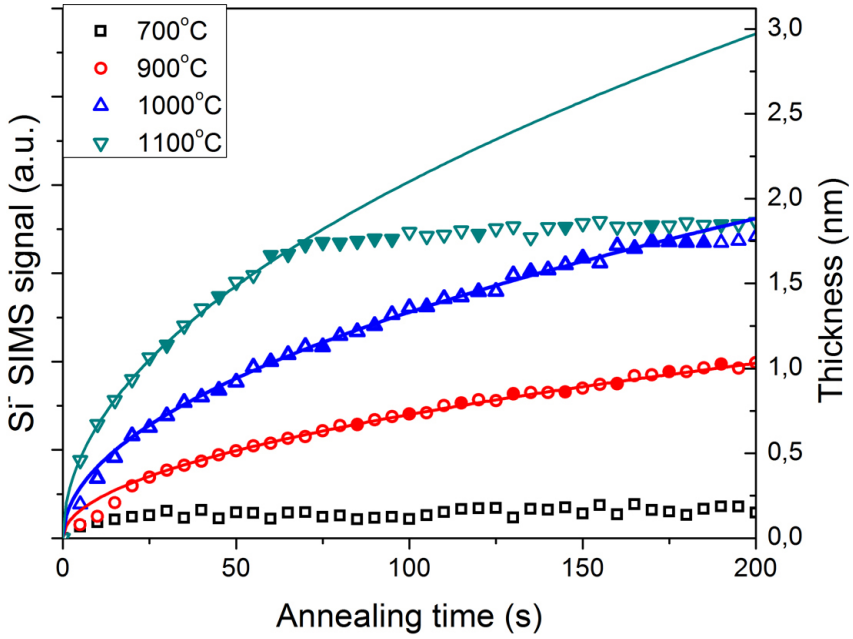

Figure 4.9: The relation between the Si^- signal (which is proportional to the amount of silicon found on the surface) and the annealing time. The amorphous sample ($700°C$) exhibits no significant segregation. For the crystalline samples the concentration of the Si on the surface scales, as expected, with a square root of time. Two diversions can be noted: at the beginning of the profile the actual concentration is lower than expected (visible for $900°C$ and $1000°C$). It shows that it takes some time for silicon to diffuse through the sample and to form the surface agglomeration. Furthermore, the amount of silicon that can agglomerate on the surface is saturable. Symbols (both full and empty) represent ToF-SIMS experimental data and solid lines represent square root fitting performed on the data in a range 20 – 50 seconds where no diversion from the expectations was noted. The fits were expanded to a full range. Full symbols and right scale represent XRR thickness measurements of SiO_2 layer (samples were exposed to air and therefore the top layer oxidized). An agreement between ToF-SIMS and XRR measurements was found and therefore it was possible to present both of them on the same figure.

surface increases with the annealing time. Similarly to the time-dependent diffusion into the thin film region, it scales, as expected (see Equation 2.60), with the square root of time with a diversion at the region of the lowest and the highest times. In both cases the amount of silicon found on the surface was below the expectations. The explanation of this phenomenon is not difficult. The diffusing silicon, as described in Section 2.3.5, is not expected to be found at the surface immediately as it needs some time to diffuse through the thin film and to reach the surface. On the other hand, at some point the saturation of surface segregation takes place and no additional Si can be agglomerated. To prove this theory the time dependent diffusion was analyzed for the full temperature range. It was noted that for the higher temperatures the first effect is strongly reduced as the diffusion rate is higher and thus the formation of Si segregated layer starts much faster. On the other hand, since the diffusion is enhanced, in higher temperatures the saturation appears earlier when compared to the samples annealed at low temperatures. This phenomenon is very well visible in Figure 4.9. For the sample annealed at $900°C$ there is no saturation, but the diversity on the beginning is clearly visible, while it is reduced for the sample annealed at $1000°C$ and not present at all for the on annealed at $1100°C$. In the two latter cases the faster saturation for higher temperatures is clearly visible. It is also important that the saturation is observed at the same amount of agglomerated silicon for both cases.

This phenomenon was further confirmed by XRR and XPS measurements. Unfortunately, as it was already mentioned in Section 4.2.2, samples had to be removed from vacuum and cleanroom environment and therefore surface contamination and oxidation of silicon layer was expected. Despite this flaw an important information was obtained: XRR measurements proved that the thickness of SiO_2 increased proportionally to the square root of the annealing time and the thickness of a saturated layer was found to be $1.82 \pm 0.15nm$. What is most important those measurements were found to be in agreement with ToF-SIMS measurements that it was possible to present them on the same figure (see Figure 4.9).

XPS measurements, beside proving the same time dependent relation, did not provide any new information. Figure 4.10 presents atomic percentages of Al and Si measured for samples annealed at $1000°C$ (similar plots were obtained for other temperatures). Just like it was proved by other methods the amount of silicon increased proportionally with the square root of the annealing time. The process was found to be saturable and the results were in agreement with other methods for all annealing temperatures. It was not surprising that Al signal was still visible for saturated SiO_2 layer because its thickness was smaller than the depth sensitivity of the tool. It is

clearly visible that measurements are not of the highest quality - surface contamination significantly influenced the results since for a pure Al_2O_3 atomic percentage of Al should be 40% whereas it is significantly lower. Values of Si atomic percentage for annealed samples is similarly reduced. Nevertheless the most important part - time dependence and saturation were undoubtedly confirmed.

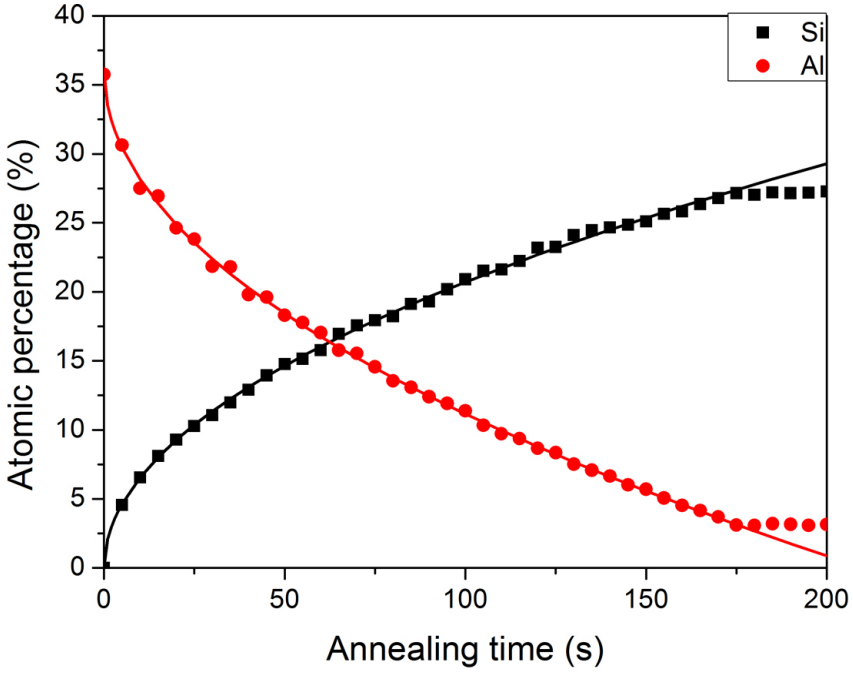

Figure 4.10: Atomic percentages of Al and Si measure by XPS for samples annealed at $1000°C$. Formation of Si agglomerated layer depends on the square root of the annealing time. The process is saturable and occurs around $175s$, just as it was proved by other methods. Symbols represent experimental data and solid lines represent square root fitting.

During the XPS measurements there was an attempt to determine whether agglomerated silicon absorbed some oxygen from the top part of alumina thin film. No such a behavior was observed but since samples were exposed to air oxygen depletion could have been easily replenished and therefore it was not possible to determine whether this effect took place or not. It would be advisable to repeat XPS measurements on samples without removing them from the vacuum but at that time such measurements were not possible.

4.4.3.2 Surface diffusion

XRR measurements were performed on several different spots for each wafer and the results were found to be the same and therefore it was concluded that most probably Si that diffused through the sample spread evenly on the surface rather than formed islands located at the end of grain boundaries. To confirm this expectation AFM imaging was performed and it turned out that indeed SiO_2 was evenly distributed on the surface and the root-mean-square roughness was found to be 4.7 ± 0.3 Å(higher than for as-grown samples which was found to be 1.2 ± 0.2 Å, similar values reported in the literature [259, 260]). This was not surprising as after reaching the surface the Si is no longer confined and may move freely in any plane directions.

The quantitative description of this process is very challenging. No in-situ measurement was available and, what is more important, it is difficult to describe the diffusion process on the surface when increasing amount of Si is reaching the top of the sample every moment. Nevertheless some attempt was done. It is important to emphasize that the proposed method does not exactly describe the surface diffusion of the Si atoms during the annealing, nevertheless it provides valuable information about the general extent of this process and allows to explain the surface segregation in detail.

To measure the surface diffusion a new approach was required. An additional sample set was produced where on top of the very thick (30 nm) alumina thin film a small Si island was deposited. Its thickness was 2nm and its base was in a quadratic form with a side length of 100μm and the shape of that island was measured by AFM since it would be needed as a reference for further measurements. However, the alumina thin film was already in crystalline form because the sample was annealed before the deposition of the silicon island. After the deposition the annealing process was repeated and the AFM measurements on the Si island should provide the desired information about the surface diffusion. An additional test had to be done: since the sample was annealed for a relatively long time it was essential to check whether some Si did not diffused from the substrate to the surface. The ToF-SIMS depth profile was obtained on the middle of the Si island. Figure 4.11 presents the intensity of the Si^- signal for the sample before and after post-annealing. It is clearly visible that the silicon did diffuse from the substrate, but did not reach the surface and therefore it may be concluded that it did not affect the measurement of the surface diffusion. Of course the diffusion from the Si island toward the substrate is also present and visible on the profile.

The samples annealed at a wide temperature range were analyzed with the AFM and the diffusion profiles were obtained. Figure 4.12 presents the

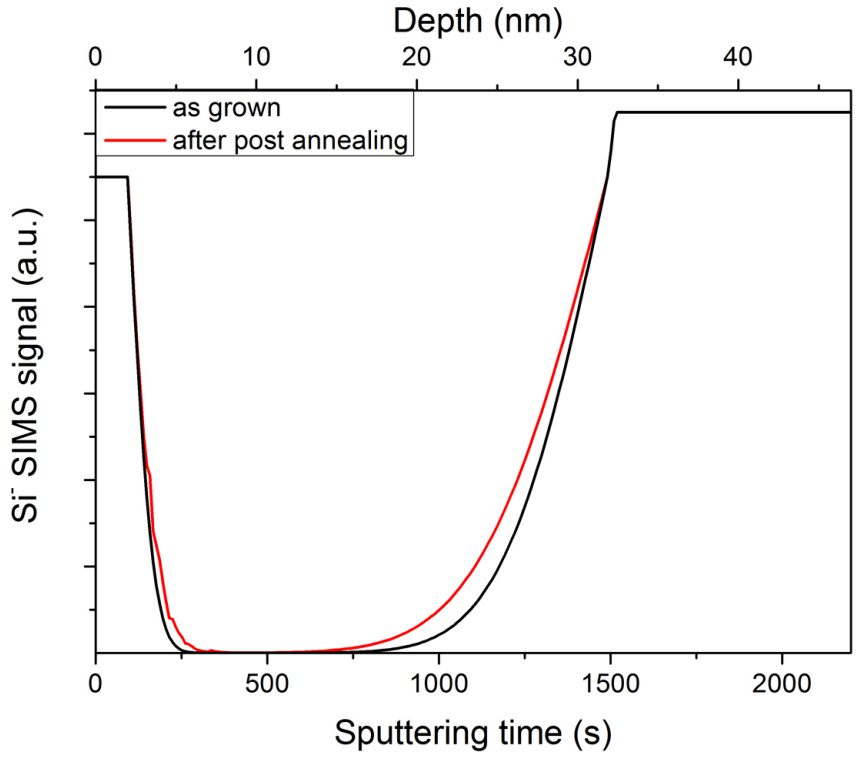

Figure 4.11: Si^- signal for the samples with an additional silicon island deposited on the surface. The alumina thin film is thick enough to ensure that during the post-annealing (at $1000°C$ for $20s$) no Si can diffuse from the substrate and alter the surface of the sample.

example of the sample annealed at $1000°C$ for $20s$ compared to the case without the post-annealing after the Si island deposition. The surface movement of Si is clear. In this case the quantification of the result is relatively easy, because the extent of the system is much larger than the diffusion length and therefore a simple equation of the diffusion into an infinite system can be applied (see Equation 2.21)

The diffusion coefficient was calculated and presented in Table 4.3. In the case of the as-grown sample the parameter presented in the table is of course not the diffusion coefficient, but it describes an error made in the calculation originating form not perfectly perpendicular wall of the Si islands. It was found to be very small so it can be assumed that it does not play a significant role in the calculations.

The temperature dependence of the diffusion coefficient was estimated as described by the Arrhenius equation (see Equation 2.62 and Figure 4.13) and

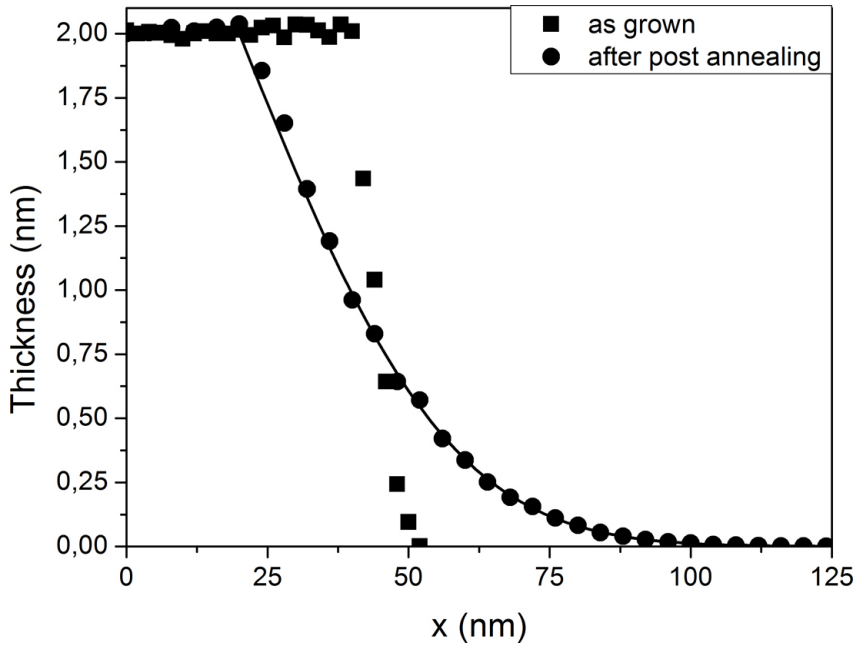

Figure 4.12: The surface diffusion of the 2nm thick Si island deposited on alumina thin film measured by AFM. Symbols represent the experimental data and solid line represents the error functional fitting. The reference measurement for the as-grown sample was included.

the activation energy was calculated. It was found to be 1.5 ± 0.02eV at the pre-exponential factor D_0 of $(7.4 \pm 0.3) \times 10^{-2}\text{cm}^2/\text{s}$

A straightforward conclusion can be made: the activation energy is low and the surface diffusion coefficient is two orders of magnitudes higher than for the bulk diffusion (compare with Section 4.5.1). This means that the movement of the Si atoms on the surface is relatively easy, specially when compared to the bulk diffusion. As it was mentioned before this experiment cannot be directly related to the silicon that spread on the surface after the segregation, but at least gives a good indication about the conditions of that movement. In other words one should not expect to see Si islands located only on top of the grain boundaries — the segregated atoms will spread evenly on the surface forming a layer of Si, just like it was observed in AFM imagining.

Post-annealing temperature $[^{\circ}C]$	Diffusion coefficient $10^{-16}[cm^2/s]$
1100	9990 ± 80
1050	6250 ± 70
1000	4150 ± 70
975	3080 ± 60
950	2200 ± 50
925	1590 ± 40
900	1250 ± 30

Table 4.3: The surface diffusion coefficient with standard deviation calculated as the error functional fitting of the diffusion profile.

4.4.3.3 Conclusions

As it was proved by three independent methods the amount of silicon found on the surface scales, as expected, with the square root of the annealing time and the deviations were explained, the final conclusion can be formulated: no or at least negligible amounts of silicon are lost to vacuum during the RTA process. Furthermore it is justified to assume that the surface of the sample acts as a sink boundary and the Si atoms that reach the surface are collected and have no further impact on the diffusion process in the thin film region provided that no saturation is observed. Therefore the boundary condition at the surface of the sample can be set as a zero concentration assumption for sufficiently short diffusion time.

4.4.4 Conclusions

All regions of interests were carefully characterized and assumptions were justified and therefore a suitable model to describe the diffusion conditions can be chosen. Out of many which were described in Section 2.3.2 the most suitable is the one denoted as "Constant surface concentration and finite sample size" with the boundary and initial conditions $C(x = 0, t) = 0$, $C(x = l, t) = C_s$ and $C(x, t = 0) = 0$ (see Equations 2.40, 2.41 and 2.42, respectively), where $x = 0$ and $x = l$ denotes the surface and the interface, respectively. The solution is given in Equation 2.52. However, this model can only be used if the diffusion saturation is not present and therefore the standard annealing time was set to $20s$. It was not advisable to set it to a lower value, because for lower temperature limited amounts of the substance diffused into the sample. It could not be higher either, because the saturation was observed for the highest annealing temperature.

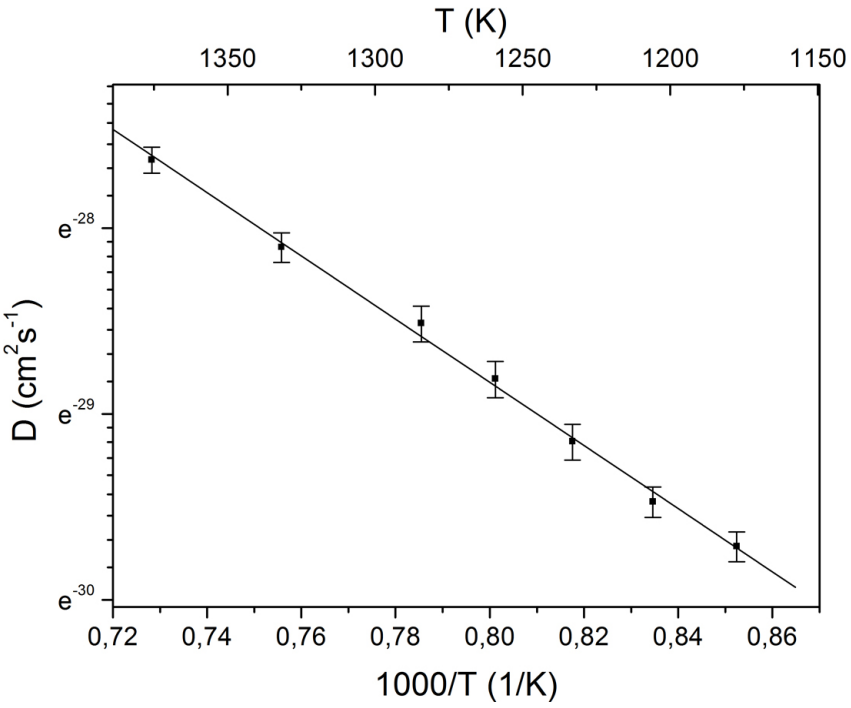

Figure 4.13: The dependence of the diffusion coefficient on the inverse temperature. Symbols represent the experimental data and solid lines represent the linear fitting.

Figure 4.14 presents the error functional fit of the diffusion profile (region (ii)). As it can be clearly seen the deviation is very small and therefore it can be concluded that the model was adequately chosen.

4.5 Diffusion parameters

As the diffusion model was successfully established it is possible to perform the quantitative analysis and thus two physical parameters, namely the diffusion coefficient at infinite temperature and the corresponding activation energy of the diffusion will be calculated. Furthermore, the diffusion length at the saturation points will be considered.

It is important to emphasize that the following calculations of the diffusion parameters are based on more than two thousands depth profiles for samples with different thickness and measured in both positive and negative mode with different sputtering ion energy. The reproducibility of the results were found to be almost perfect and thus it may be concluded that

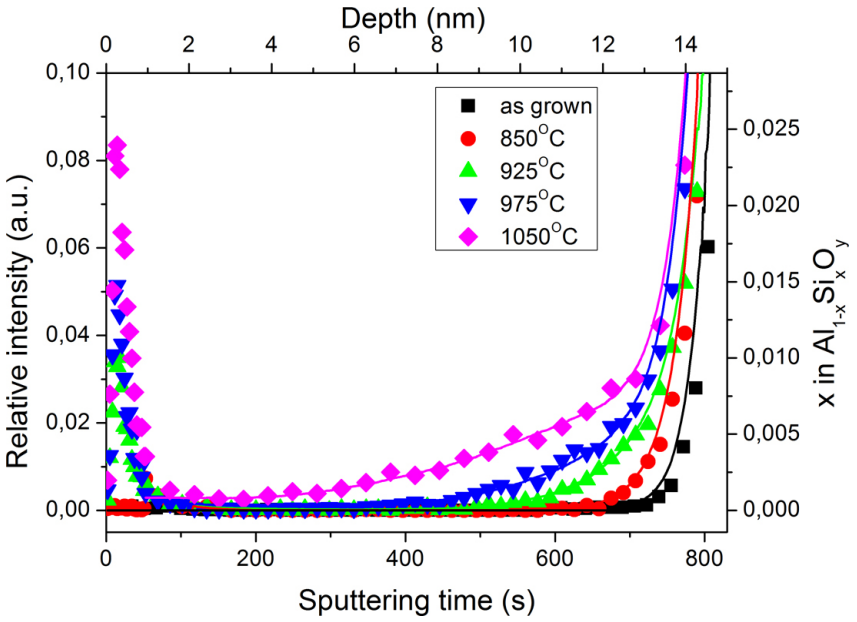

Figure 4.14: The Si^- depth profile for samples annealed at different temperatures for $20s$. Symbols represent experimental data and solid lines represent error functional fitting on the diffusion profile

the accuracy of the calculated diffusion parameters is extremely good.

4.5.1 Diffusion coefficient

From the error functional fitting presented in Figure 4.14 the diffusion coefficient can be determined according to the Equation 2.52. The obtained result for the full temperature range is presented in Table 4.4.

For the as-grown sample there is no diffusion nor segregation. The slope in the interface region can be attributed to the ion mixing during the SIMS depth profiling (see Section 3.2.7.1). However, the ion mixing affects profiles of annealed samples as well and therefore this effect should be properly subtracted to obtain the actual value of the diffusion coefficient. The error functional fitting was performed on the profile of the as-grown sample as well and the resulting parameter M was determined. It describes quantitatively the extent of the ion mixing effect. As the broadening of the diffusion profile scales with the diffusion coefficient, the following relation can be formulated:

$$D_{exp} = D + M \tag{4.1}$$

where D_{exp} is the parameter obtained from the error functional fitting and D

Annealing temperature $[^{\circ}C]$	Diffusion coefficient $10^{-16}[cm^2/s]$	Diffusion coefficient $10^{-16}[cm^2/s]$
1100	564 ± 16	562 ± 18
1050	243 ± 14	241 ± 15
1000	97.7 ± 6.9	96 ± 7.5
975	60.3 ± 5.3	59.0 ± 7.0
950	36.7 ± 3.3	36.4 ± 3.6
925	21.7 ± 2.1	21.0 ± 2.6
900	12.3 ± 1.1	11.9 ± 1.5
850	4.0 ± 0.3	-
800	2.8 ± 0.3	-
750	1.8 ± 0.2	-
700	1.2 ± 0.2	-
650	0.7 ± 0.2	-

Table 4.4: The diffusion coefficient with standard deviation calculated as the error functional fitting of the diffusion profile (second column) and from the amount of silicon found on the surface (third column)

is the actual diffusion coefficient. The parameter M was found to be much smaller than the parameter D_{exp} and it can be assumed that $D \approx D_{exp}$. The problem was a silent assumption that the ion mixing effect is the same for all samples (constant M). Several different experiments were performed with various energies of incoming ions and in both negative and positive modes. The value of parameter M was changing, but it was always much smaller than the parameter D_{exp} and the maximal difference for M calculated at different conditions was smaller than an order of magnitude. Furthermore, the difference between D_{exp} for various experiments was found to be very small, in many cases negligible and therefore it was concluded that the ion mixing effect does not play a significant role and the shape of the diffusion profile can be attributed directly to the diffusion coefficient, i.e. $D \approx D_{exp}$ as assumed earlier.

The calculation of the diffusion coefficient can also be based on the amount of silicon found on the surface. As it was discussed, it is reasonable to assume that the system has a source-sink behavior. However, this assumption is only valid for annealing times that are far from saturation. As it was shown in Section 4.4.3, this is fulfilled for the particular case (annealed for 20 seconds). The gradient of the concentration at $x = 0$, which determines the flux through the boundary there, followed the Equation 2.61. If the flux is integrated over the time of the annealing, the amount of silicon

found on the surface can be calculated and compared to the experimental value and thus the diffusion coefficient can be determined. As it is presented in Table 4.4, the diffusion coefficient calculated with those two methods are in a good agreement. This might serve as an additional, strong indication that no or negligible small amounts of silicon are lost to vacuum during the annealing process. Otherwise the diversity should be much higher.

At this point it is important to stress again an excellent reproducibility of the results. As it was already explained in Section 3.2.7.4, each calculation was based on at least ten profiles and the following results were complementary. In this case the situation is much stronger: the diffusion coefficient was calculated from multiple measurements with both positive and negative modes, different sputtering energies and what is most important - on samples annealed for different times. And in every situation the resulting diffusion coefficient was the same with very small discrepancies.

4.5.2 Diffusion length

As the diffusion coefficient was calculated, the corresponding diffusion length can be determined as well. It is particularly interesting to examine the L_d at points were some deviations from the square root of the time dependency was noted.

At the beginning the total amount of silicon that diffused into the sample as a function of time was analyzed (see Figure 4.8). It was noted that the discrepancy occurs for $L_d \approx 20nm$. The value was higher than expected since the relation given by Equation 2.60 should hold only for diffusion length smaller than the size of the sample. However, the problem can be adequately explained: as it was described above the sample can be approximated as a source-sink system and therefore the Si atoms which reached the surface have no further influence on the diffusion conditions in the thin film region, provided that the surface saturation is not experienced (this assumption holds in this situation, the surface segregation appears later, compare Figure 4.9) and thus the amount of silicon that contributes to the diffusion process is limited.

It is not proper to determine the diffusion length which corresponds to the surface saturation, because the diffusion rate is significantly changed after $L_d \approx 20nm$. However, a qualitative conclusion should be formulated: the surface segregation is saturable, as it was already shown in Section 4.4.3

4.5.3 Activation energy

As it was explained in Section 2.3.3, the temperature dependence of the diffusion coefficient is given by the Arrhenius equation. Figure 4.15 presents the Arrhenius plot as derived according to Equation 2.62. Two temperature regimes are evident which correspond to the transition from the amorphous to the crystalline phase around 1150 K. In both regimes, the linearity confirms the validity of Equation 2.62. The derived energies of activation are 0.80 ± 0.03eV and 2.64 ± 0.02eV at pre-exponential factors D_0 of $(1.6 \pm 0.3) \times 10^{-12}$cm^2/s and $(2.9 \pm 0.2) \times 10^{-4}$cm^2/s for amorphous and crystalline samples, respectively.

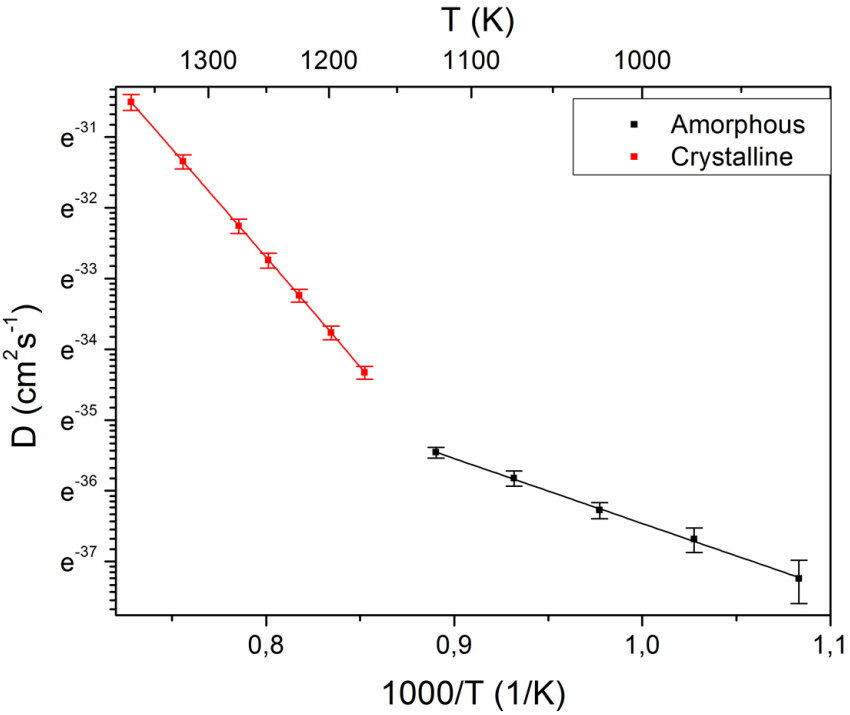

Figure 4.15: The dependence of the diffusion coefficient on inverse temperature. Linear behavior for two regimes: crystalline and amorphous phase. Symbols represent experimental data and solid lines linear fitting.

It is important to interpret properly the calculated values and understand what they mean in practice. The diffusion rate for amorphous samples was found to be relatively low. Perhaps the collective mechanism (see Section 2.3.4) plays a significant role in the diffusion process. Further experiments should be performed to determine the diffusion mechanism in amorphous samples.

4.5.4 Conclusions

The relatively small activation energy, in particular for the amorphous state, allows for the diffusion of a considerable amount of Si into the film and to the surface. This will alter the composition and the electrical properties of the films, and may have a significant influence on the performance of the alumina-based memory devices. Similar problems caused by Si segregation were reported for other high-k materials too [238, 239].

The silicon segregated at the surface may not be the most challenging obstacle. The knowledge of its presence gives a chance to get rid of it during the production process by using cleaning procedures like etching. The by far worse problem is the silicon diffusing into the thin film, especially when one takes into consideration that the advancing of the scaling down of the memory devices will require materials to be thinner than 15 nm as used in this work.

4.6 Samples with different compositions

So far only the pure alumina thin films deposited on a Si wafer with a native oxide have been considered (those samples will be named AOS denoting the **a**lumina-native **o**xide-**s**ilicon wafer stack). A relatively small modifications of the stack composition may prove to be beneficial and therefore two major changes will be discussed, namely an additional Si_3N_4 sublayer (ANOS - the additional letter N denotes the additional **n**itride layer in the stack) and a composite material, $Al_{1-x}Si_xO_y$.

4.6.1 Si_3N_4 sublayer

Figure 4.16 presents a typical depth profile for sample deposited with a silicon nitride sublayer. The presence of an additional layer can be easily seen between the alumina thin film and the native oxide of the Si substrate.

The direct comparison of the AOS (see Figure 4.2) and ANOS samples provides three conclusions:

1. The ANOS samples are somewhat less contaminated (lower C^- signal). This can be a result of a slightly different preparation conditions. Nevertheless the contamination level for both samples is relatively low and one would not expect any major influence on the diffusion process.

2. The Si diffusion and segregation is stronger for the AOS samples, which is especially visible for the Si segregation peak. Total amount of diffused

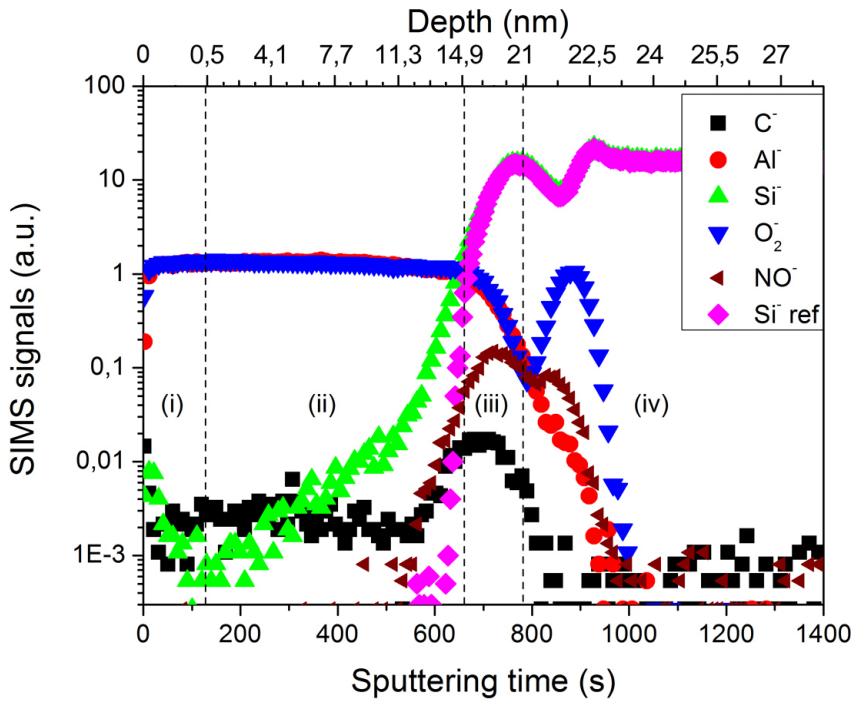

Figure 4.16: Typical depth profile for a sample deposited on a wafer with an additional sublayer and annealed at $1000°C$ for $20s$. All presented ions are singly ionized and each element refers to the most abundant isotope. Four regions can be identified: (i) a thin top layer indicating surface segregation of Si, (ii) the alumina thin film with a Si concentration gradient, (iii) silicon nitride sublayer, and (iv) the interface to the Si bulk substrate. The Si^-ref shows the intensity of Si for a non-annealed sample. Unfortunately N^- signal is usually too weak in SIMS measurements to draw any conclusions from it and therefore NO^- has to be presented. Sputtering rate is significantly different for each region and therefore the depth scale was adjusted for each region separately.

Annealing temperature $[^{\circ}C]$	Diffusion coefficient $10^{-16}[cm^2/s]$	Diffusion coefficient $10^{-16}[cm^2/s]$
1100	266 ± 13	263 ± 13
1050	100 ± 10	97 ± 11
1000	32.1 ± 2.7	31.8 ± 2.9
975	19.2 ± 1.9	19.2 ± 2.1
950	10.6 ± 1.1	10.1 ± 1.2
925	6.6 ± 0.7	6.2 ± 0.8
900	3.1 ± 0.4	3.0 ± 0.5
850	3.6 ± 0.3	-
800	2.4 ± 0.2	-
750	1.8 ± 0.2	-
700	1.0 ± 0.2	-
650	0.6 ± 0.2	-

Table 4.5: The diffusion coefficient with standard deviation calculated as the error functional fitting of the diffusion profile (second column) and from the amount of silicon found on the surface (third column)

Si is about 1.5 times higher for the AOS than ANOS after the identical annealing treatment.

3. It should be also noted that the interface between the alumina thin film and the substrate is defined in the same way as it was for the AOS samples - at the point where the Al^- signal is decreased by half. However, the intensity of Si^- at that point is lower than it was for the AOS samples and therefore it should be concluded that the surface concentration (C_s in Equation 2.52) is smaller for the ANOS samples.

Following the same procedure as described before, the diffusion coefficient for the ANOS samples was calculated. Table 4.5 presents the obtained result. Once again a good agreement for both methods (calculation based on the diffusion profile and the amount of silicon found on the surface) can be seen.

As an obvious next step the activation energy of the Si diffusion was calculated. The Arrhenius plot is presented on Figure 4.17. The energies of activation was found to be: 0.83 ± 0.03eV and 3.10 ± 0.02eV at the pre-exponential factors D_0 of $(2.0 \pm 0.3) \times 10^{-12}\text{cm}^2/\text{s}$ and $(6.7 \pm 0.2) \times 10^{-3}\text{cm}^2/\text{s}$ for the amorphous and crystalline samples, respectively.

The comparison to the pure AOS film shows a rather unexpected result: the diffusion parameters were found to be very similar for the amorphous

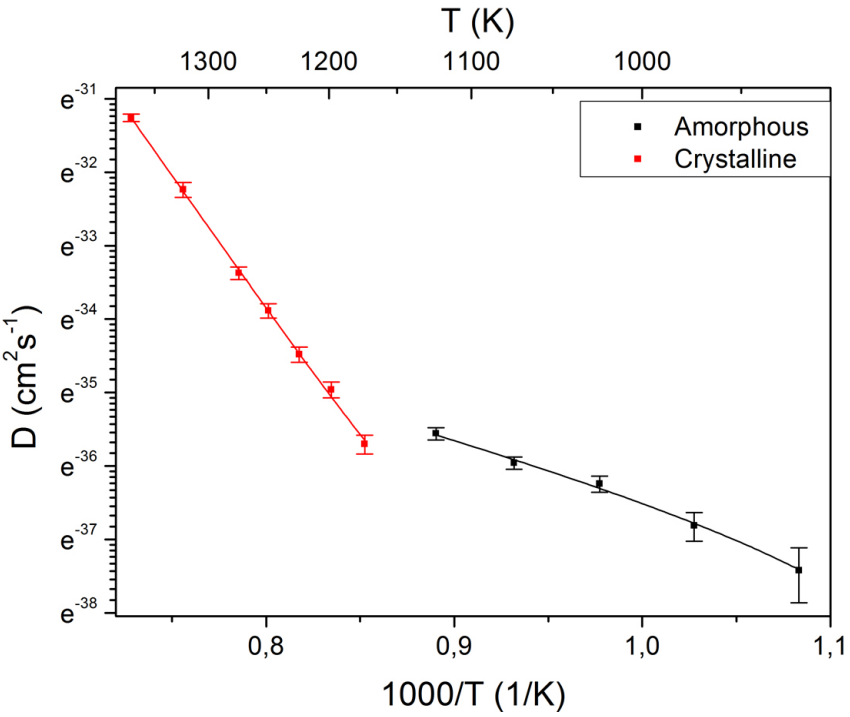

Figure 4.17: The dependence of the diffusion coefficient on the inverse temperature. The linear behavior for two regimes, the crystalline and amorphous phases, is apparent. Symbols represent experimental data and solid lines represent linear fitting.

phase, whereas significantly different for the crystalline samples. An additional layer may influence the properties of the source e.g. the energy which a diffusing atom should acquire to overcome the binding energy and to be injected from the source to the sample, but it should not influence the actual diffusion rate in the thin film region. In the case of the amorphous samples this reasoning seems to be valid: smaller amounts of diffused Si are found inside the ANOS than AOS samples, but so is the surface concentration of Si at the interface and the diffusion rate is similar for both types of samples.

The situation was complex in the crystalline samples. The influence of the substrate type on the microstructure of various materials (including changing the average grain size) was reported in the literature [261–264] but the microstructure was determined during the growth of the samples whereas in the following experiments crystallization (and thus formation of grains) occurred during the annealing process of a full grown thin films and therefore the influence of the substrate should be significantly decreased (or even not

present at all). Therefore such a big difference of activation energy of ANOS and AOS samples could not explained on the basis of the grain boundary diffusion.

To overcome this problem an additional sample set was created: a thick layer (30 nm) of alumina was deposited on wafers with native oxide and then samples were annealed for a short time just to ensure the crystallization (it was proved by XRD measurements). Since the annealing conditions were exactly the same it could be assumed that the average grain size was the same (or at least almost the same) for all samples. Only after that an additional 5 nm layer of SiO_2 or Si_3N_4 was deposited on the top of the samples. Annealing process was repeated but with much lower temperature (below $900°C$) to avoid recrystallization and changing the grain structure. By comparing the ToF-SIMS measurements of both samples an ability of Si atom originating from SiO_2 and Si_3N_4 to be injected into alumina thin films could be determined.

The direct comparison was, however, not possible. Several issues had to be taken into account before the final conclusion would be made. First of all it had to confirmed that the silicon from the bottom of the sample did not diffuse through the whole sample. The procedure was already described in Section 4.4.3.2 and obtained results were very similar to those presented in Figure 4.11 - it was confirmed that Si coming from the substrate did not reach the top part of the alumina thin film.

The second problem was that, as it was already mentioned, the surface concentration of Si was smaller for ANOS samples but since it did not change the shape of the diffusion profile (see Equation 2.52) nor the diffusion length signals were normalized (the value at the beginning of the diffusion profile was set to 1).

The most challenging problem was the fact that SIMS mixing effects are much stronger in the direction of sputtering and cannot be treated as negligible (for most experiments the diffusion from the substrate, not from the top of the sample was considered). It was therefore immediately apparent that any quantitative results would not be possible to obtain. Nevertheless qualitative information was successfully established: ToF-SIMS measurements were repeated with all possible ion species and energies (and hence with different mixing properties) and for each measurement the result was the similar to the one presented on Figure 4.18: the diffusion length was higher for AOS samples.

A final conclusion could be formulated: since the grain structure was the same for both types of samples (and thus the diffusion rate in the thin film region can be assumed to be the same for both cases) Si atoms required higher energy to be injected from nitride layer into the crystalline alumina thin film

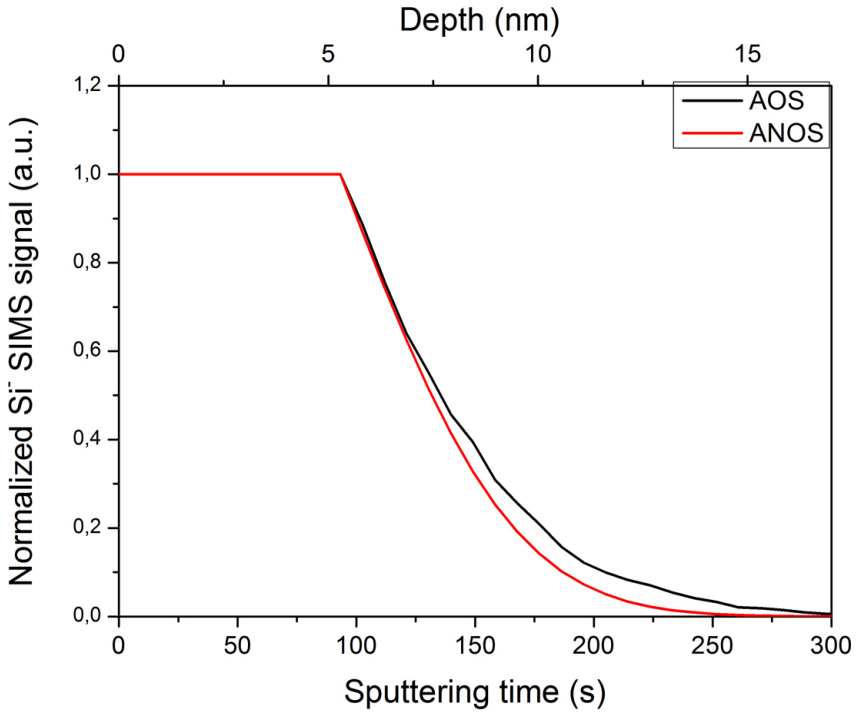

Figure 4.18: Normalized Si^- signals originating from SiO_2 and Si_3N_4 layers deposited on top of thick alumina thin films. Despite the elevated mixing effects it is clearly visible that the diffusion length is higher for AOS samples.

than from the oxide layer. That is why the activation energy was found to be higher for ANOS samples. It is not a surprising conclusion because Si_3N_4 is reported to be more thermally stable than SiO_2[265]. Therefore the rate of the thermal decomposition is higher for SiO_2 and thus more Si atoms can be injected into the alumina thin film.

4.6.2 Composite material $Al_{1-x}Si_xO_y$

The same procedure as described above was performed for the Si-containing samples deposited on both native oxide and silicon nitride substrates. The ToF-SIMS depth profiles were obtained, diffusion coefficients were calculated and plotted as a function of the inverse temperature and the activation energy of the diffusion was calculated. A surprising fact was observed: the activation energy for the amorphous samples (both AOS and ANOS compositions) and for the crystalline ANOS samples decreases for higher silicon concentration, whereas it increases for the crystalline AOS samples. Figure 4.19 presents

this relation. The dependence is linear and was found to be $E_a = 0.8 - 0.51x$ eV for the amorphous samples, $E_a = 3.10 - 0.53x$ eV for the crystalline ANOS samples and $E_a = 2.64 + 1.65x$ eV for the crystalline AOS samples. Parameter x describes the concentration of Si ($Al_{1-x}Si_xO_y$).

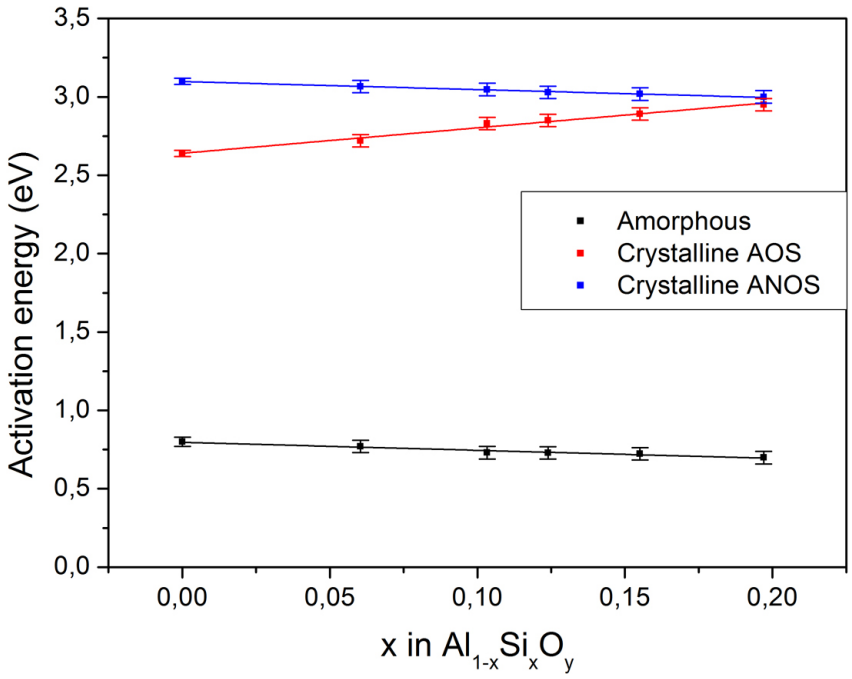

Figure 4.19: The dependence of the activation energy of the diffusion on silicon concentration. The activation energy decreases with higher Si concentration for the ANOS samples and the amorphous AOS while it increases for the crystalline AOS samples. Symbols represent experimental data and solid lines represent linear fitting.

To explain the resulting data the samples with the different annealing time were analyzed. The following observation was made: the crystalline AOS samples have a strong tendency to form an intermixed layer between the alumina and the silicon oxide layers. This results in the restraint of further Si diffusion. This effect was not seen for the amorphous AOS and both ANOS samples. Figure 4.20 presents a suitable comparison for the crystalline AOS and ANOS samples. A small plateau of Si^- signal clearly visible for AOS samples can be attributed to an additional interface layer.

Furthermore, it was noted that the size of the interface layer depends strongly on the annealing time and the Si concentration. The dependence on the temperature is also present, but much weaker compared to the former

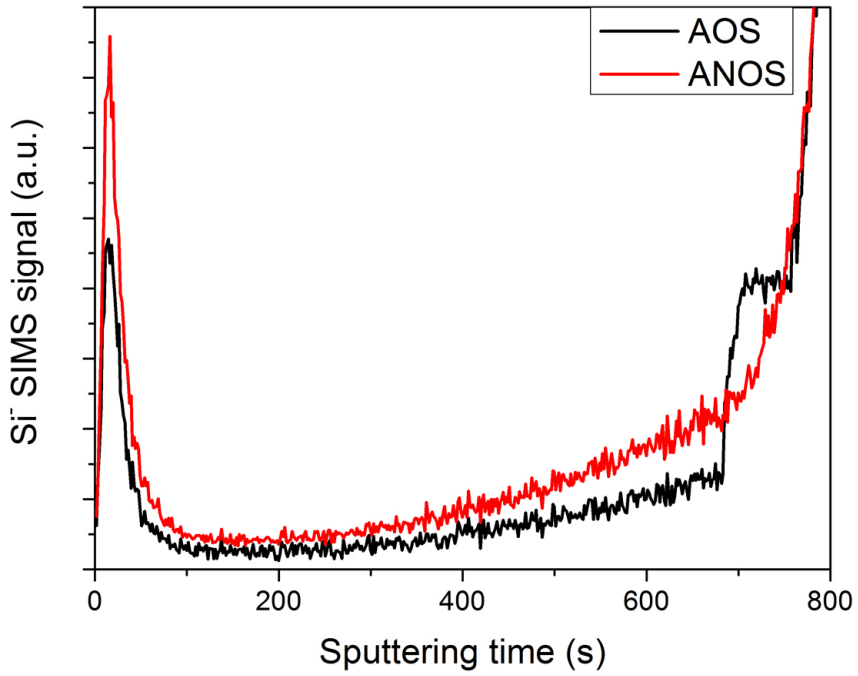

Figure 4.20: Si^- signal for the pure alumina samples annealed for 40 seconds. An interface between Al_2O_3 and the substrate can be identified for the AOS samples.

two factors. For larger interface thickness the restraint of the Si diffusion was bigger.

One more interesting fact was observed. It turned out that the thickness of the interface layer is proportional to the square root of the annealing time as presented on Figure 4.21. This behavior is expected because as it was explained in Section 2.3.2 the amount of silicon which diffuses from the substrate into the sample is proportional to the square root of time (see Equation 2.29) and the interface layer can be formed only if enough Si is present in the sample. Plots were interpolated and it turned out that the formation of the interface layer starts when the concentration of Si near the substrate is $x \approx 0.11$ regardless the initial amount of Si in the composite material. In other words: this condition is fulfilled from the very beginning for the material with initial $x = 0.12$ and therefore the formation of the interface is observed immediately. For samples with $x = 0.06$ it takes ten seconds to accumulate enough silicon near the substrate to create the interface layer and for pure alumina thin films - forty seconds. It was tested for samples with different initial x as well and every time the interpolation gave

the same result - the threshold annealing time required to start the formation of the interface layer corresponds to Si concentration $x \approx 0.11$ in the region next to the substrate. Unfortunately the interface layer with thickness lower than 0.5 nm is not visible in ToF-SIMS measurements. However, the agreement of measurements on samples with different compositions suggests that the threshold amount of Si required to form the interface layer is not a measurement artifact.

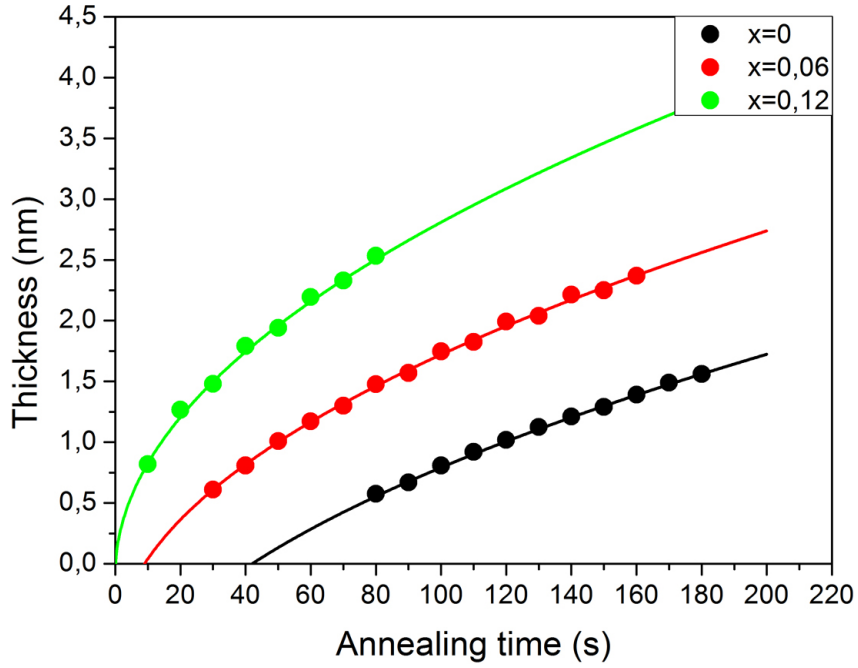

Figure 4.21: The thickness of the interface layer for $Al_{1-x}Si_xO_y$ samples with varying Si concentration x annealed at the same temperature for a different periods of time. An interpolation of those plots suggested that the formation of the interface layer starts at $x \approx 0.11$

Given the amount of information provided by the experiment, the final conclusions can be formulated. Calculated activation energy is a global parameter describing the amount of silicon that can be found on the surface and inside the alumina layer, but cannot be equivalent to the activation energy of the diffusion only. At least four different factors have a major influence on the global activation energy:

1. *Injection of Si from the substrate.* The ability of Si to reach the alumina thin film depends on the type of the layer stack. Experiments with reversed stack composition (SiO_2 and Si_3N_4 layer deposited on

top of the thick alumina thin film) proved that it is higher for the AOS samples.

2. *Interface formation.* The crystalline AOS samples have a strong tendency to form a blocking layer during the annealing which restrain further diffusion. This effect strongly depends on the annealing time and the Si concentration in the composite material layer since the diffusion occurs in both directions and Si incorporated in the thin film may participated in formation of an interface. The influence of the annealing temperature is much weaker. It is reasonable to assume that this phenomenon is not visible for the amorphous samples because not enough silicon can diffuse to the sample for a given annealing times. This effect was also not observed for the ANOS samples, but still may be present, as suggested by Chang et al. [266].

3. *Actual diffusion through the thin film.* The slight decrease of the global activation energy for the ANOS samples with the growing Si concentration serves as a indication that the diffusion is enhanced. It might be explained by the higher probability of silicon to be segregated and thus trapped (which means that it does not influence the diffusion process any further) on the surface, but to gain detailed information further analysis is required.

Taking into account three different processes that occur during the RTA one can provide the answer for the phenomenon: for the ANOS samples the injection of Si through the nitride layer is difficult, but the rise of the temperature, the annealing time and the Si concentration increases the total amount of Si on the surface and in the thin film. Therefore the global activation energy slightly decreases for the samples with higher Si concentration. On the other hand the injection of Si through the oxide layer is relatively easy, but the rise of the annealing time, the Si concentration and, to a small extent, the temperature results in formation of an interface between the silicon oxide and the thin film which restrains further diffusion and thus the global activation energy increases for the samples with higher Si concentration or annealed for longer times.

4.7 Dielectric measurements

Dielectric measurements were by provided by courtesy of Fraunhofer Institute and were not performed by the author of this work.

ToF-SIMS measurements provided a lot of useful information concerning the diffusion and the structural changes in $Al_{1-x}Si_xO_y$ thin films. It is, however, always advisable to confirm an established diffusion model with other, independent technique and therefore dielectric measurements were performed on samples with various annealing conditions (time and temperature) and compositions (composite materials).

It is obvious that that the measurement of a relative permittivity of a sample is not enough to provide any advanced information about its structure or the diffusion process. The results, however, were compared to the suggested diffusion model and an agreement was noted. It can serve as an additional indication that the suggested model is valid.

4.7.1 Amorphous samples

At the beginning the samples without thermal treatment were investigated. A relative permittivity of a pure alumina thin film was found to be 9.20 ± 0.05 which is in agreement with the value reported in a literature[36–42]. An interesting fact was observed for composite materials: for samples with sufficiently low amount of silicon ($x < 0.2$ in $Al_{1-x}Si_xO_y$) the relative permittivity of the sample decreases linearly with the increasing amount of silicon as presented on Figure 4.22 and described by the Equation 4.2.

$$\epsilon = 9.21 - 5.54x \tag{4.2}$$

As it was discussed in Section 4.2.1 the amount of silicon that diffused through the sample was below that limit for most experiments and therefore it was possible to analyze the relative permittivity of amorphous samples that were thermally treated as well.

An interesting observation was made for samples annealed at the same temperature for different periods of time. It turned out that the relative permittivity decreases with a square root of time. It is in accordance with the expectations: as it was discussed in Section 2.3.2 the amount of silicon which diffuses into the sample is proportional to the square root of time (see Equation 2.29) and the relative permittivity decreases linearly with increasing Si concentration as derived in Equation 4.2.

Finally, the diffusion model suggested in Section 4.4 can be tested. As it was derived the diffusion profiles should follow the Equation 2.52. It can be combined with an empirical relation described by the Equation 4.2 and thus the expected value of the relative permittivity can be calculated. The procedure is relatively simple (see Figure 4.23 for schematic presentation): a sample can be treated as a series of parallel-plate capacitors with a given

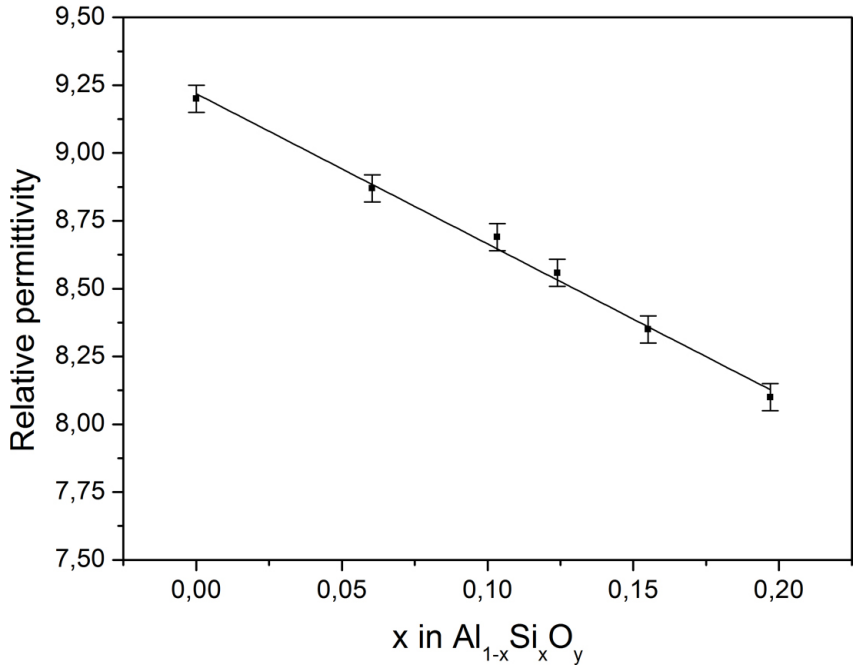

Figure 4.22: The relative permittivity of the as-grown amorphous samples scales linearly with the increasing amount of Si up to $x \approx 0.2$

capacitor area A and infinitesimal thickness dt. For each capacitor the concentration of silicon can be calculated in accordance with the Equation 2.52 and the resulting relative permittivity can be obtained from the Equation 4.2. Using a well known property of the series of capacitors the capacitance of the whole sample can be calculated as an integral given in Equation 4.3:

$$\frac{1}{C} = \int_0^L \frac{t}{\epsilon(t)\epsilon_0 A} dt \tag{4.3}$$

Using this procedure the theoretical and experimental value of the relative permittivity were compared and found to be in agreement. It is important to stress that it was done for more than one hundred amorphous samples, with different thickness, annealing time and temperature and a match of theoretical and experimental values with negligible discrepancy was found for all of them. It may serve as a strong indication that the suggested diffusion model is valid.

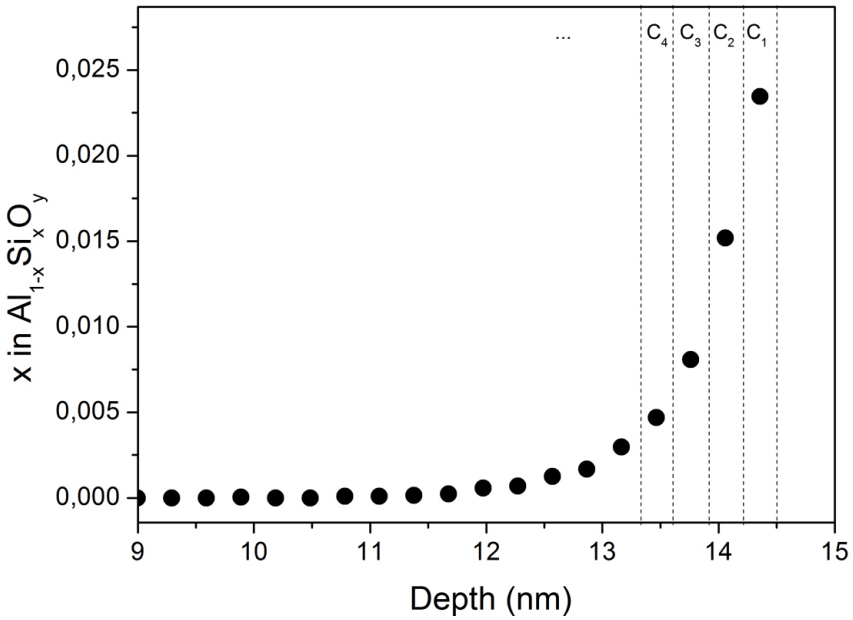

Figure 4.23: The sample is treated as a series of parallel-plate capacitors with infinitesimally small thickness. For each capacitor Si concentration is determined from the previously established theoretical diffusion model and the relative permittivity is calculated from the empirical relation. The capacitance and thus the relative permittivity of the whole sample can be calculated using the well known property of the series of capacitors.

4.7.2 Crystalline samples

The crystalline samples proved to be by far more challenging. It would be advisable to perform a similar procedure like it was applied in case of amorphous samples but a serious problem occurred: the basic information about the amorphous samples was established by analysis of the uniform as-grown $Al_{1-x}Si_xO_y$ thin films. Alas, uniform crystalline samples do not exist, simply because the crystallization process requires the thermal annealing and it leads to the diffusion of Si from the substrate. One can of course argue that for small amounts of Si a crystalline sample may have similar properties as an amorphous one i.e. the relative permittivity should decrease linearly with the increasing amount of silicon in the composite material. Such an assumption may seem to be reasonable but it is just an ad hoc hypothesis. One has to remember that crystalline alumina is an anisotropic material and the relative permittivity is reported to be significantly different when measured parallel and perpendicular to C-axis (11.5 and 9.3, respectively)[267]. Furthermore

it was suggested that the grain boundary diffusion is the most dominant diffusion mechanism and thus the anisotropy of the system can be expected to be even higher. Assuming that the crystalline sample has similar properties like amorphous one is therefore unfounded.

To overcome this problem a new series of $Al_{1-x}Si_xO_y$ samples was created with much higher thickness (30 nm). They were annealed in low temperature and for a short period of time, just to ensure the crystallization process. ToF-SIMS measurements confirmed that for the pure alumina thin film the silicon did not reach the top of the sample (see Figure 4.24). The relative permittivity was measured and then the top 5 nm of the sample was sputtered away with ToF-SIMS tool using low energy ions to prevent sample mixing. The relative permittivity was measured again at the bottom of the crater and from those two values the relative permittivity of the sputtered layer could be directly calculated. Since silicon did not diffuse to that layer the calculated value of the relative permittivity describes the properties of an uniform crystalline alumina thin film.

In case of composite $Al_{1-x}Si_xO_y$ thin films a small adjustment to the procedure had to be made since a surface segregation occurs immediately during the annealing (Silicon that was already in the sample tends to agglomerate at the surface). Before the first dielectric measurement the top 2-3 nm of the sample was sputtered away to eliminate the surface segregated layer. The rest of the procedure did not differ from the pure alumina thin film. In this way the relative permittivity of uniform crystalline $Al_{1-x}Si_xO_y$ thin films with various Si content was measured.

The relative permittivity of a pure crystalline alumina thin film was found to be 11.41 ± 0.05 (as it was reported in the literature[267]). Similarly to the amorphous samples for small amounts of Si ($x \approx 0.2$ in $Al_{1-x}Si_xO_y$) the relative permittivity decreases linearly with the increasing amount of silicon as presented on Figure 4.25 and given by the Equation 4.4.

$$\epsilon = 11.41 - 7.64x \tag{4.4}$$

Before checking if the dielectric measurements confirm the diffusion model for crystalline samples one more measurement had to be performed. It was mentioned earlier that in most crystalline samples a Si segregated layer is present at the top of the sample. Using a well established technique (measurement performed on the whole sample and repeated for sample with the segregated layer removed) the relative permittivity of the top layer was found to be 3.91 ± 0.07 which is the value of silicon dioxide. It is not surprising because samples were removed from vacuum before dielectric measurements and the segregated layer is very thin (usually 1-2 nm) and therefore one expect that the whole agglomerated silicon oxidized.

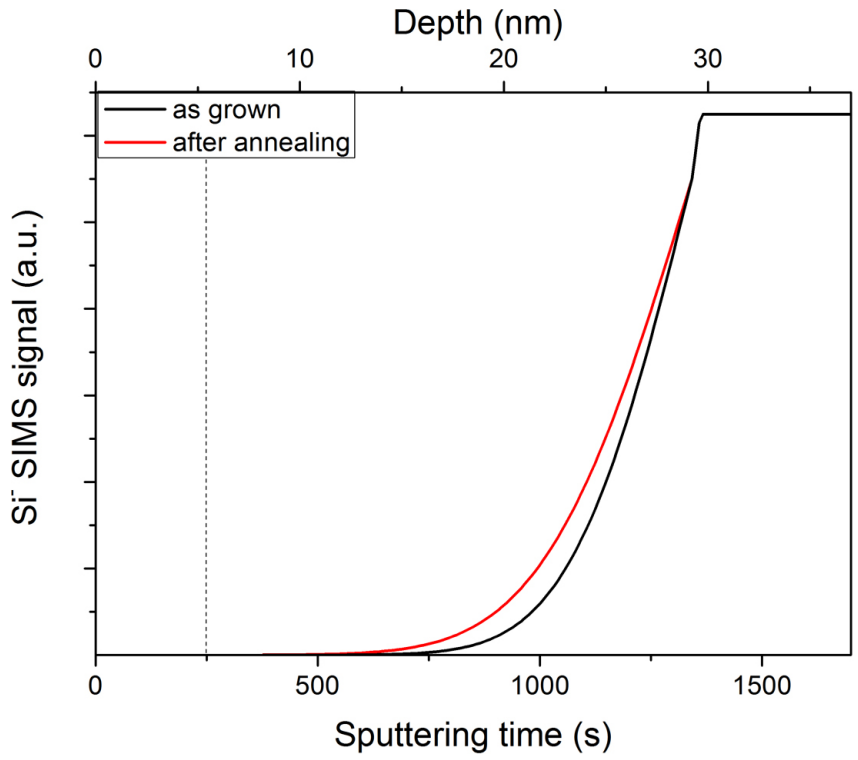

Figure 4.24: ToF-SIMS measurements confirms that for sufficiently thick sample silicon cannot diffuse to the surface of the sample and therefore such a sample can be used to determine the relative permittivity of a crystalline thin film. After the annealing the relative permittivity of the whole sample was measured. Then a top 5 nm layer (dashed line) were sputtered away and the dielectric measurement was repeated. The relative permittivity of the removed layer can be directly calculated and since no Si managed to diffuse up to that layer the result describes the properties of an uniform crystalline sample.

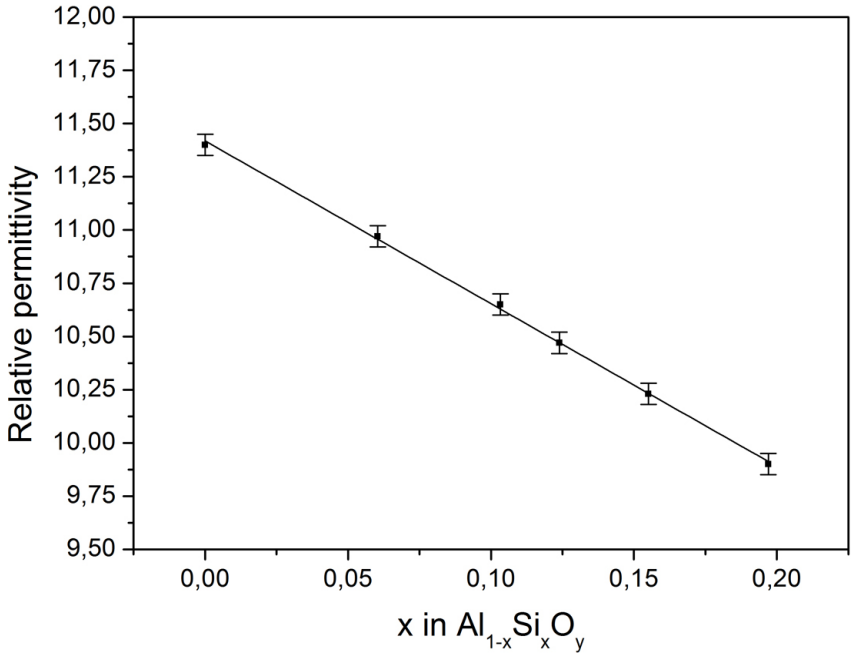

Figure 4.25: The relative permittivity of the uniform crystalline samples scales linearly with the increasing amount of Si up to $x \approx 0.2$

With that knowledge dielectric measurements can be used to test the diffusion model for the crystalline samples. The theoretical value of the relative permittivity can be calculated using the diffusion profile (Equation 2.52) and the empirical relation described by the Equation 4.4. An additional capacitor representing the top segregated layer has to be added to the series and the relative permittivity of the whole sample can be calculated as schematically presented on Figure 4.26. Once again an agreement was found for more then five hundred different samples with varying thickness and annealing conditions (both temperature and time). It further confirms the validity of the suggested diffusion model.

4.7.3 Interface

Samples with an interface layer (see Section 4.6.2) are particularly interesting for dielectric measurements. The relative permittivity of the the interface layer can be obtained by two different ways: ToF-SIMS low energy sputtering can be used to remove the thin film up to the interface layer and then the relative permittivity can be directly measured or one can measure the relative permittivity of the whole sample and then calculate it for the interface layer

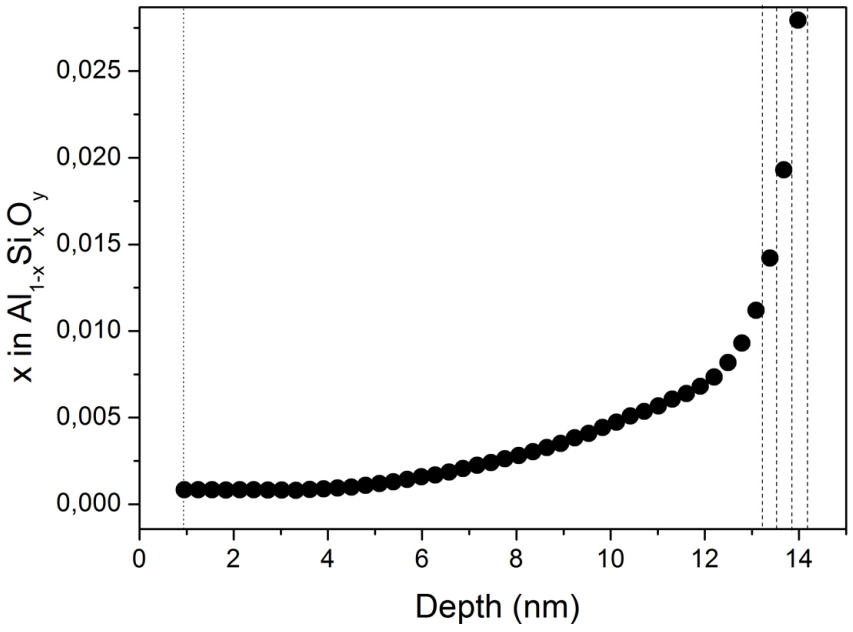

Figure 4.26: The sample is treated as a series of parallel-plate capacitors with infinitesimally small thickness. For each capacitor Si concentration is determined from the previously established theoretical diffusion model and the relative permittivity is calculated from the empirical relation. The top layer (first nanometer) consists of silicon dioxide. The capacitance and thus the relative permittivity of the whole sample can be calculated using the well known property of the series of capacitors.

by subtraction of the impact of the Si segregated layer and the diffusion profile, just as it was described for crystalline sample. It turned out that the results of both procedures were consistent and therefore the second one was used because it was significantly less time consuming.

The relative permittivity of the interface layer is significantly lower than of the alumina thin films, usually ranging between 5.4 and 6. It was noted that for pure alumina thin films the relative permittivity of the interface layer is decreasing with a square root of annealing time as presented on Figure 4.27. As it was previously discussed such a behavior was expected due to the increasing amount of silicon diffusing into the sample.

The case of the composite $Al_{1-x}Si_xO_y$ samples was by far more interesting. It turned out that the relative permittivity of the interface layer is constant for sufficiently low annealing times and starts to drop only after some time (see Figure 4.27). The effect was particularly well visible for samples with

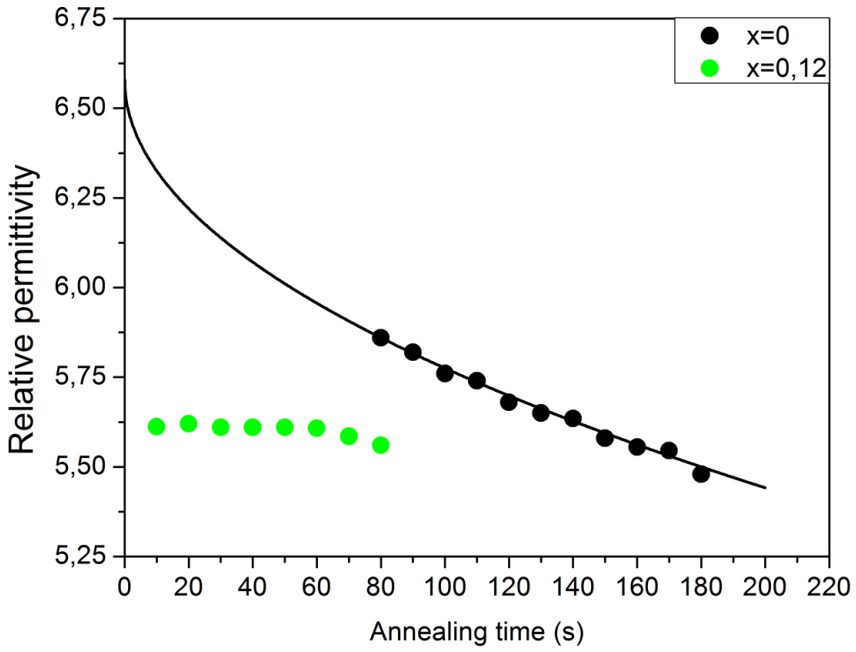

Figure 4.27: For pure alumina thin films the relative permittivity of the interface layer decreases with the square root of time. For composite materials the relative permittivity is constant for sufficiently low annealing times because only limited amounts of Si can diffuse into the sample. After some time the amount of diffused Si is comparable to the initial concentration and then a clear decrease of the relative permittivity can be observed.

$x > 0.1$. The explanation of this phenomenon is not difficult. For sufficiently low annealing times only a small amount of Si may diffuse into the sample and the interface is formed from the silicon which was already incorporated within the sample during the production. And since it was evenly distributed the relative permittivity of the interface layer is constant. For sufficiently long annealing times the amount of Si that diffused into the sample is comparable or even surpass the initial concentration and thus the drop of the relative permittivity can be observed.

One more phenomenon can explain the fact that the relative permittivity of the interface layer is constant at the beginning of the annealing process. Samples with a high concentration of Si ($x > 0.3$) were investigated. As it was discussed in Section 4.2.1 the quantitative description is not possible but the qualitative measurements revealed that the formation of the interface layer may start during the production procedure. In other words: qualitative ToF-SIMS measurements on as-grown $Al_{1-x}Si_xO_y$ samples with high Si

concentration revealed a clear interface layer. And since the silicon is evenly distributed in the sample the relative permittivity of the interface layer is constant for sufficiently low annealing times.

Chapter 5

Summary

A sample set consisting of the $Al_{1-x}Si_xO_y$ ultra thin films atomic layer deposited on a different substrates was fabricated, annealed in various conditions and successfully investigated by means of the ToF-SIMS and other analytical techniques. The thermally induced structural and compositional changes that occurs in the alumina thin films during the annealing were acknowledged and quantitatively characterized

This chapter will be devoted to summarize the knowledge that has been obtained about the processes occurring in the alumina samples during the annealing; to discuss their influence on the performance of the hypothetical alumina-based memory devices. Furthermore, usefulness of ToF-SIMS technique as a leading analytical method will be discussed.

5.1 Results

Figure 5.1 presents a summary of the obtained results. Many of the processes take place simultaneously but will be considered separately to provide good comprehension of the annealing influence.

1. The $Al_{1-x}Si_xO_y$ ultra thin film is atomic layer deposited on the Si wafer. The exact type of the substrate is not specified as the most conclusions are similar and the differences will be noted. Then the sample is exposed to the thermal process. A high temperature and a long annealing time treatment will be considered since the integration of the alumina thin films in memory devices requires them to be in the crystalline phase.

   At the beginning of the annealing process the sample is still amorphous. The exact diffusion mechanism was not identified. There were some indications pointing out at the dangling bond diffusion (a reduction of the

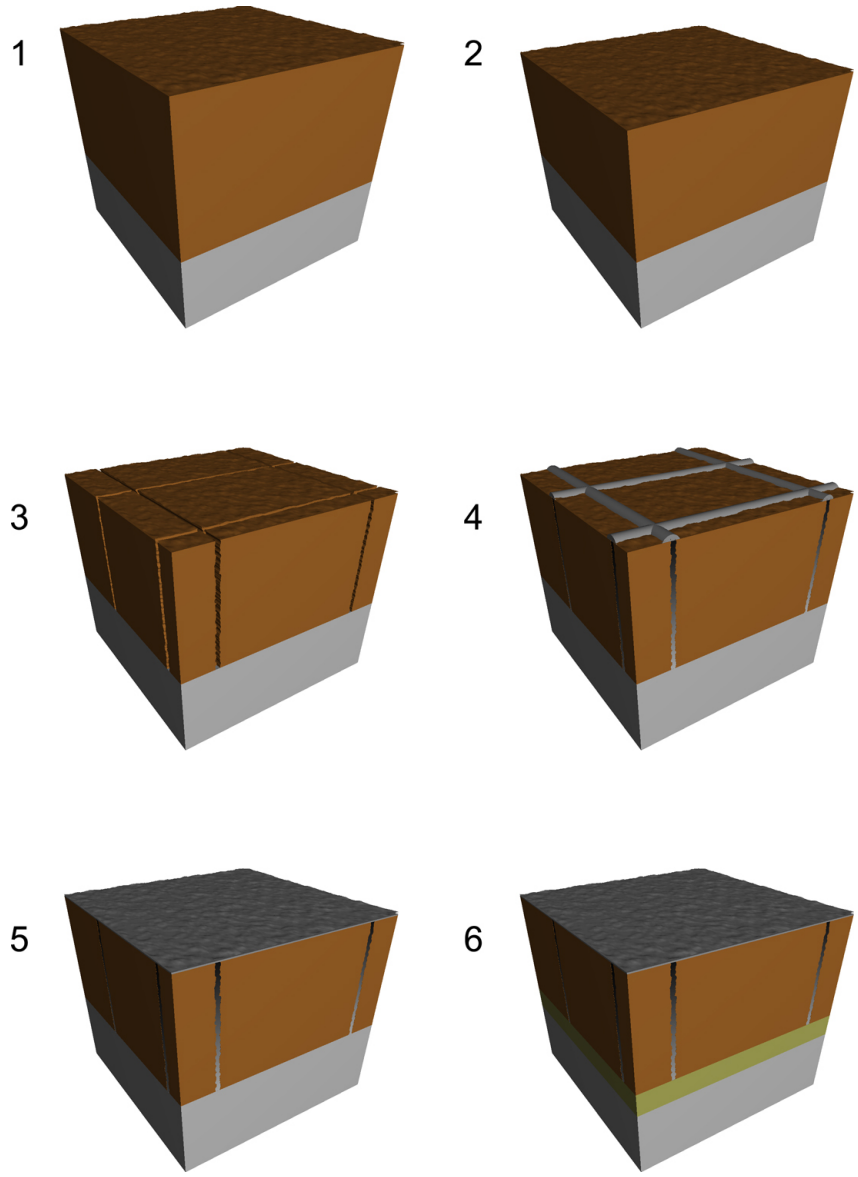

Figure 5.1: Summary of the thermally induced processes occurring in the $Al_{1-x}Si_xO_y$ ultra thin films: 1) Initial state, the thin film (brown) is deposited on the substrate (gray). 2) Densification and shrinkage of the sample. 3) Polycrystallization and formation of the grain boundaries. 4) Grain boundary diffusion and surface segregation. 5) Surface diffusion and formation of a Si layer covering the whole surface of the sample. 6) Formation of the interface between the thin film and the substrate.

diffusion rate for samples annealed in oxygen) and the collective mechanism (a relatively low value of D_0). However, the diffusion parameters were quantitatively described: the activation energy was found to be relatively low, but so was the diffusion coefficient and thus the Si diffusion is very small, almost negligible, as the time when the sample remains amorphous is very limited.

Furthermore the validity of the diffusion parameters was additionally confirmed by the dielectric measurement. The theoretical and experimental values of the relative permittivity of the samples were found to be in agreement.

2. At sufficiently high temperature the sample starts to crystallize after a very short time. It leads to the densification and thus to the shrinkage of the sample. It was found that the thickness of the sample is reduced by about 10% of its initial value.

3. The sample does not crystallize as a single crystal but forms a polycrystalline structure. The grain size and thus the grain boundary density depend on the cooling rate. Bigger grains (i.e. lower grain boundary density) is typical for samples with a lower cooling rate.

4. The grain boundary diffusion is the leading diffusion mechanism in the crystalline samples. Many observation were made which would be difficult to explain without the grain boundary diffusion assumption (e.g. the dependence on the cooling rate surface segregation of Si that diffused through the whole sample).

   Silicon is injected from the substrate and diffuse along the boundaries toward the surface of the sample. There it segregates forming so-called islands — regions where the diffused atoms are agglomerated.

   The extent of the diffusion process depends on the type of the substrate. It was proved that the silicon injection is much easier for samples deposited on a silicon wafer with a native oxide. An additional silicon nitride layer prevents the penetration of silicon from the substrate to the thin film region.

5. The segregated silicon starts to diffuse along the surface of the sample. The diffusion coefficient was found to be relatively large (two orders of magnitude higher than the bulk diffusion) and therefore the formation of island described in the previous point cannot be observed — the silicon atoms are spread evenly on the surface very fast. The formation

of a silicon layer was successfully acknowledged and its saturation was observed and successfully characterized.

Similarly to the amorphous samples the validity of the diffusion parameters was confirmed by the dielectric measurements.

6. During the thermal treatment the thin film and the substrate start to form an interface layer. Its size depends strongly on the annealing time and the amount of Si that was incorporated in the thin film during the production process. The temperature influence was much weaker but still present. It was noted that the formation of the interface layer may only start if enough silicon is present at the thin film/substrate interface. The relative permittivity of the interface layer was found to be significantly lower than of the alumina thin film.

   This effect was very strong for samples deposited on wafers with just native oxide. For samples with an additional silicon nitride layer the effect was not observed by means of the ToF-SIMS, but its presence cannot be excluded.

It can be concluded that the diffusion process occurring in the $Al_{1-x}Si_xO_y$ ultra thin films deposited on a silicon substrate was described in details. The relatively small activation energy allows for the diffusion of a considerable amount of Si into the film and to the surface. This will alter the composition and the electrical properties of the films and may have a significant influence on the performance of the alumina-based memory devices. As it was already mentioned before, the surface segregated layer does not seem to be a challenging problem, as it can be easily removed by various cleaning procedures. The silicon incorporated in the thin film region is a far worse problem, especially at the interface with the substrate. It may create many trap levels and significantly disturb the performance of memory devices. Further suggestions about the analyzing and production techniques will be aimed to identify the sources of the bad performance of memory devices and propose a suitable procedure to overcome them.

5.2 Usefulness of ToF-SIMS technique

One of the biggest achievements of this work was delivering a proof that Time-of-Flight Secondary Ion Mass Spectroscopy can be used as a leading analytical technique for characterization of high-k thin films. Obviously, it cannot work as a completely independent method as its measurements are in relative form. There is always a need to compare the ToF-SIMS results

with other analytical technique but after a few test a suitable models can be created and further characterization can be performed with ToF-SIMS measurements only.

At this point it is possible to measure an unknown $Al_{1-x}Si_xO_y$ sample and determine its thickness, composition before annealing (parameter x), exact distribution of Si in the whole sample after the diffusion process, thickness of the SiO_2 layer segregated at the surface of the sample, thickness of the interface layer and relative permittivity of the whole sample and of any of its parts and it can be achieved by a single ToF-SIMS measurement whereas it would require several other techniques if no model was created.

Furthermore in the specific laboratory that this experiments were performed ToF-SIMS method was usually cheaper and faster then other techniques, it did not require any additional sample preparation nor removal from the vacuum system which for some samples is a crucial requirement.

There is no reason to doubt that similar procedure of establishing suitable quantitative models can be applied for other materials as well which can prove to be beneficial both time- and expense-wise.

There are, however, some limitations. As it was shown for some samples which are significantly different then others (e.g. high parameter x in $Al_{1-x}Si_xO_y$) quantification is not possible. For those cases only general qualitative description was available. Furthermore it should be noted that ToF-SIMS measurements in most cases can only describe global parameters. Calculated activation energies and diffusion coefficients cannot be associated with any of the specific diffusion mechanism but should be rather treated as a global description of the diffusion process. Similarly, it was not possible to obtain quantitative information about the microstructure of the samples. Precise defect analysis and average grain size should be measured by other analytical techniques.

Bibliography

[1] G. Moore. *Cramming more components onto integrated circuits.* Electronics Magazine. p. 4, 1965.

[2] G. Moore. *Progress in digital integrated electronics.* IEEE, IEDM Tech Digest. p. 11-13, 1975.

[3] C. Disco and B. van der Meulen. *Getting new technologies together.* New York: Walter de Gruyter. p. 206207, 1998.

[4] M. Dubash. *Moore's Law is dead, says Gordon Moore.* Techworld, 2005.

[5] H.R. Huff, C.A. Richter, M.L. Green, G. Lucovsky, and T. Hattori. *Ultrathin SiO_2 and High-K Materials for ULSI Gate Dielectrics.* Cambridge University Press, 1999.

[6] G.D. Wilk, R.M. Wallace, and J.M. Anthony. *High-k gate dielectrics: Current status and materials properties considerations.* Journal of Applied Physics, 89, 5243, 2001.

[7] *Physics and technology of high-k gate dielectrics I.* Electrochemical Society, 2003.

[8] *Physics and technology of high-k gate dielectrics II.* Electrochemical Society, 2004.

[9] H. Huff and D. Gilmer. *High Dielectric Constant Materials: VLSI MOSFET Applications.* Springer, 2005.

[10] A.A. Demkov and A. Navrotsky. *Materials Fundamentals of Gate Dielectrics.* Springer, 2006.

[11] E. Gusev. *Defects in High-k Gate Dielectric Stacks: Nano-Electronic Semiconductor Devices.* Springer, 2006.

[12] M. Houssa. *High k Gate Dielectrics.* CRC Press, 2010.

[13] H. Wong. *Nano-CMOS Gate Dielectric Engineering.* CRC Press, 2011.

[14] G. He and Z. Sun. *High-k Gate Dielectrics for CMOS Technology.* John Wiley and Sons, 2012.

[15] S. Kar. *High Permittivity Gate Dielectric Materials.* Springer, 2013.

[16] M. Oshima, S. Toyoda, T. Okumura, J. Okabayashi, H. Kumigashira, K. Ono, M. Niwa, K. Usuda, and N. Hirashita. *Chemistry and band offsets of HfO_2 thin films for gate insulators.* Applied Physics Letters, 83, 2172, 2003.

[17] T. Lee, J. Ahn, J. Oh, Yangdo Kim, Y.-B. Kim, D.-K. Choi, and J. Jung. *Characterization of Ultra-Thin HfO_2 Gate Oxide Prepared by Using Atomic Layer Deposition.* Journal of the Korean Physical Society, 42, No. 2, 272-275, 2003.

[18] K. Xiong, J. Robertson, M.C. Gibson, and S.J. Clark. *Defect energy levels in HfO_2 high-dielectric-constant gate oxide.* Applied Physics Letters, 87, 183505, 2005.

[19] C. Shen, M.F. Li, H.Y. Yu, X.P. Wang, Y.-C. Yeo, D.S.H. Chan, and D.-L. Kwong. *Physical model for frequency-dependent dynamic charge trapping in metal-oxide-semiconductor field effect transistors with HfO_2 gate dielectric.* Applied Physics Letters, 86, 093510, 2005.

[20] K. Tse and J. Robertson. *Defect passivation in HfO_2 gate oxide by fluorine.* Applied Physics Letters, 89, 142914, 2006.

[21] S. Sugiura, S. Kishimoto, T. Mizutani, M. Kuroda, T. Ueda, and T. Tanaka. *Normally-off AlGaN/GaN MOSHFETs with HfO_2 gate oxide.* Physica Status Solidi C, 5, 1923-1925, 2008.

[22] G. Hyvert, T. Nguyen, L. Militaru, A. Poncet, and C. Plossu. *A study on mobility degradation in nMOSFETs with HfO_2 based gate oxide.* Materials Science and Engineering B, 165, 129-131, 2009.

[23] J.B. Park, W.S. Lim, B.J. Park, I.H. Park, Y.W. Kim, and G.Y. Yeom. *Atomic layer etching of ultra-thin HfO_2 film for gate oxide in MOSFET devices.* Journal of Physics D: Applied Physics, 42, 055202, 2009.

[24] A.P. Huang, Z.C. Yang, and P.K. Chu. *Hafnium-based High-k Gate Dielectrics.* Advances in Solid State Circuit Technologies 16, 333, 2010.

[25] G.D. Wilk, R.M. Wallace, and J.M. Anthony. *Hafnium and zirconium silicates for advanced gate dielectrics.* Journal of Applied Physics 87 (1), 484-492, 2000.

[26] G. Lucovsky and G.B. Raynery. *Microscopic model for enhanced dielectric constants in low concentration SiO_2-rich noncrystalline Zr and Hf silicate alloys.* Applied Physics Letters 77, 2912, 2000.

[27] G.D. Wilk and R.M. Wallace. *Electrical properties of hafnium silicate gate dielectrics deposited directly on silicon.* Applied Physics Letters 74 (19), 2854-2856, 1999.

[28] H.T. Johnson-Steigelman, A.V. Brinck, and P.F. Lyman. *Production of a hafnium silicate dielectric layer for use as a gate oxide by solid-state reaction.* Journal of Vacuum Science and Technology A, 24 (4), 2006.

[29] T. Erlbacher, A.J. Bauer, and H. Ryssel. *Hafnium silicate as control oxide in non-volatile memories.* Microelectronic Engineering, 84 (9-10), 2239-2242, 2008.

[30] M. Copel, M. Gribelyuk, , and E. Gusev. *Structure and stability of ultrathin zirconium oxide layers on Si(001).* Applied Physics Letters, 76, 436, 2000.

[31] J.P. Chang, Y-S. Lin, S. Berger, A. Kepten, R. Bloom, and S. Levy. *Ultrathin zirconium oxide films as alternative gate dielectrics.* Journal of Vacuum Science and Technology B 19, 2137, 2001.

[32] M. Yanjun, O. Yoshi, L. Stecker, D.R. Evans, and S.T. Hsu. *Zirconium oxide based gate dielectrics with equivalent oxide thickness of less than 1.0 nm and performance of submicron MOSFET using a nitride gate replacement process.* Electron Devices Meeting, 1999. IEDM '99, 149-152, 199.

[33] G.D. Wilk and R.M. Wallace. *Stable zirconium silicate gate dielectrics deposited directly on silicon.* Applied Physics Letters, 76, 112, 2000.

[34] W.J. Qi, R. Nieh, E. Dharmarajan, B.H. Lee, Y. Jeon, L. Kang, K. Onishi, and J.C. Lee. *Ultrathin zirconium silicate film with good thermal stability for alternative gate dielectric application.* Applied Physics Letters, 77, 1704-1706, 2000.

[35] K. Jaehyun and Y. Kijung. *Characterization of Zirconium Silicate Gate Dielectrics Deposited on Si(100) Using $Zr(NEt_2)_4$ and $Si(O^nBu)_4$.* Electrochemical and Solid-State Letters, 7 (5), F35-F37, 2004.

[36] C. H. Lee, K. C. Park, and K. Kim. *Charge-trapping memory cell of $SiO_2/SiN/high-K$ dielectric Al_2O_3 with TaN metal gate for suppressing backward-tunneling effect.* Applied Physics Letters 87, 073510, 2005.

[37] Ch. H. Lee, S. H. Hur, Y. Ch. Shin, J. Ch. Choi, D. G. Park, and K. Kim. *Charge-trapping device structure of $SiO_2/SiN/high-k$ dielectric Al_2O_3 for high-density flash memory.* Applied Physics Letters 86, 152908, 2005.

[38] R. Chau, J. Brask, S. Datta, G. Dewey, M. Doczy, B. Doyle, J. Kavalieros, B. Jin, M. Metz, A. Majumdar, and M. Radosavljevic. *Application of high-k gate dielectrics and metal gate electrodes to enable silicon and non-silicon logic nanotechnology.* Microelectronic Engineering 80, 1-6, 2005.

[39] S. Maikap, H. Y. Lee, T. Y. Wang, P. J. Tzeng, C. C. Wang, L. S. Lee, K. C. Liu, J. R. Yang, and M. J. Tsai. *Charge trapping characteristics of atomic-layer-deposited HfO_2 films with Al_2O_3 as a blocking oxide for high-density non-volatile memory device applications.* Semiconductor Science and Technology 22, 884889, 2007.

[40] G. Wang and M. H. White. *Characterization of scaled MANOS nonvolatile semiconductor memory (NVSM) devices.* Solid-State Electronics 52, 14911497, 2008.

[41] G. D. Wilk, R. M. Wallace, and J. M. Anthony. *High-k gate dielectrics: Current status and materials properties considerations.* Journal of Applied Physics 89, 5243, 2001.

[42] M. Copel, E. Cartier, E.P. Gusev, S. Guha, N. Bojarczuk, and M. Poppeller. *Robustness of ultrathin aluminum oxide dielectrics on Si(001).* Applied Physics Letters 78, 2670, 2001.

[43] J.I. Frenkel. Zeitschrift fuer Physik 35, 652, 1926.

[44] C. Wagner and W. Schottky. Zeitschrift fuer Physikalische Chemie B 11, 163, 1931.

[45] P. Ehrhart. *Properties and interactions of atomic defects in metals and alloys.* Landolt-Boernstein, New Series III, Springer, Berlin, 1991.

[46] R.W. Siegel. *Atomic Defects and Diffusion in Metals, in Point Defects and Defect Interactions in Metals; J.I. Takamura (ed.).* North Holland, Amsterdam, 1982.

[47] J.H. Crawford and L.M. Slifkin. *Point Defects in Solids.* New York: Plenum Press, 1975.

[48] G. D. Watkins. *Native defects and their interactions with impurities in silicon, in Defects and Diffusion in Silicon Processing; T. Diaz de la Rubia, S. Coffa, P.A. Stolk, and C.S. Rafferty (eds.).* MRS Symposium Proceedings, volume 469, Materials Research Society, Pittsburgh, 1997.

[49] J.P. Hirth and J. Lothe. *Theory of dislocations.* Krieger Pub Co., 1992.

[50] H. Kleinert. *Gauge Fields in Condensed Matter, Vol. II, Stresses and defects.* World Scientific, Singapore, 1989.

[51] H. Schmalzried. *Solid State Reactions.* Verlag Chemie, Weinheim, 1981.

[52] C.P. Flynn. *Point Defects and Diffusion.* Clarendon Press, Oxford, 1972.

[53] C.P. Flynn. *Point Defects and Diffusion.* Clarendon Press, Oxford, 1972.

[54] A.M. Stoneham. *Theory of Defects in Solids.* Clarendon Press, Oxford, 1975.

[55] F. Agullo-Lopez, C.R.A. Catlow, and P. Townsend. *Point Defects in Materials.* Academic Press, London, 1988.

[56] H.J. Wollenberger. *Point Defects, in: Physical Metallurgy, R.W. Cahn and P. Haasen (Eds.).* North-Holland Publishing Company, 1983.

[57] L.W. Barr and A.B. Lidiard. *Defects in Ionic Crystals, in: Physical Chemistry An Advanced Treatise.* Academic Press, New York, 1970.

[58] R.G. Fuller. *Ionic Conductivity including Self-diffusion, in: Point Defects in Solids, J. M. Crawford Jr. and L.M. Slifkin (Eds.).* Plenum Press, 1972.

[59] A. Seeger, D. Schumacher, W. Schilling, and J. Diehl. *Vacancies and Interstitials in Metals.* North-Holland Publishing Company, Amsterdam, 1970.

[60] N.L. Peterson and R.W. Siegel. *Properties of Atomic Defects in Metals.* North-Holland Publishing Company, Amsterdam, 1978.

[61] C. Abromeit and H. Wollenberger. *Vacancies and Interstitials in Metals and Alloys.* Materials Science Forum 1518, 1987.

[62] O. Kanert and J.M. Spaeth. *Defects in Insulating Materials.* World Scientific Publ. Comp., Ltd., Singapore, 1993.

[63] H. Ullmaier. *Atomic Defects in Metals.* Springer-Verlag, Berlin and Heidelberg, 1991.

[64] M. Schulz. *Impurities and Defects in Group IV Elements and III-V Compounds.* Springer-Verlag, 1989.

[65] F. Beniere. *Diffusion in Alkali and Alkaline Earth Halides; in: Diffusion in Semiconductors and Non-metallic Solids; D.L. Beke (Vol.Ed.).* Springer-Verlag, 1999.

[66] G. Erdelyi. *Diffusion in Miscelaneous Ionic Materials, in: Diffusion in Semiconductors and Non-metallic Solids; D.L. Beke (Vol.Ed.).* Springer-Verlag, 1999.

[67] A. Seeger and H. Mehrer. *Analysis of Self-diffusion and Equilibrium Measurements, in: Vacancies and Interstitials in Metals; A. Seeger and D. Schumacher and J. Diehl and W. Schilling (Eds.).* North-Holland Publishing Company, Amsterdam, 1970.

[68] W.M. Lomer. *Vacancies and other Point Defects in Metals and Alloys.* Institute of Metals, 1958.

[69] J. Maier. *Physical Chemistry of Ionic Solids Ions and Electrons in Solids.* John Wiley and Sons, 2004.

[70] A.R. Allnatt and A.B. Lidiard. *Atomic Transport in Solids.* Cambridge University Press, 1993.

[71] J.H. Westbrook. *Structural Intermetallics.* Warrendale, PA, TMS, 1993.

[72] G. Sauthoff. *Intermetallics.* VCH Verlagsgesellschaft, Weinheim, 1995.

[73] H. Bakker. *Tracer Diffusion in Concentrated Alloys, in: Diffusion in Crystalline Solids, G.E. Murch; A.S. Nowick (Eds.).* Academic Press, Inc., 1984.

[74] W. Frank, U. Goesele, H. Mehrer, and A. Seeger. *Diffusion in Silicon and Germanium, in: Diffusion in Crystalline Solids; G.E. Murch and A.S. Nowick (Eds.).* Academic Press, Inc., 1984.

[75] K. Girgis. *Structure of Intermetallic Compounds, in: Physical Metallurgy; R.W. Cahn and P. Haasen (Eds.).* North-Holland Physics Publishing, 1983.

[76] M. Schulz. *Impurities and Defects in Group IV Elements, IV-IV and III-V Compounds.* Springer-Verlag, 2002.

[77] T.Y. Tan and U. Goesele. *Diffusion in Semiconductors, in: Diffusion in Condensed Matter Methods, Materials, Models; P. Heitjans and J. Kaerger (Eds.).* Springer-Verlag, 2005.

[78] S.M. Sze. *Physics of Semiconductor Devices.* Wiley, New York, 1967.

[79] A. Seeger nad K.P. Chik. *Diffusion Mechanisms and Point Defects in Silicon and Germanium.* Physica Status Solidi 29, 455542, 1968.

[80] M. Werner and H. Mehrer. *in: DIMETA-82, Diffusion in Metals and Alloys; F.J. Kedves and D.L. Beke (Eds.);* . Trans Tech Publications, Diffusion and Defect Monograph Series No. 7, 392, 1983.

[81] F.J. Humphreys and M. Hatherly. *Recrystallisation and related aneal-ing phenomena.* Elsevier, 2004.

[82] A.P. Sutton and R.W. Balluffi. *Overview no. 61: On geometric criteria for low interfacial energy.* Acta Metallurgica 35 (9), 1987.

[83] R.D. Doherty, D.A. Hughes, F.J. Humphreys, J.J. Jonas, D. Juul Jenson, M.E. Kassner, W.E. King, T.R. McNelley, H.J. McQueen, and A.D. Rollett. *Current Issues In Recrystallisation: A Review.* Materials Science and Engineering A238, 1997.

[84] G. Gottstein and L.S. Shvindlerman. *Grain Boundary Migration in Metals: Thermodynamics, Kinetics, Applications, 2nd Edition.* CRC Press, 2009.

[85] R. Phillips. *Crystals, Defects and Microstructures. Modeling Across Scales.* Cambridge University Press, 2001.

[86] A.R. Allnatt. *Statistical Mechanics of Point-Defect Interactions in Solids.* Wiley and Sons, Inc., 2007.

[87] S. Pizzini. *Defect Interaction and Clustering in Semiconductors. in Solid State Phenomena, Volumes 85 - 86.* Trans Tech Publications, 2001.

[88] A.J. Morton. *Point defects and defect interactions in metals.* Acta Crystallographica Section A 40 (3), 2001.

[89] A.I. Morosov and A.S. Sigov. *Indirect interaction between mobile defects and their clusterization in metals.* Solid State Communications 67 (9), 2001.

[90] D. Kropman, U. Abru, T. Kaerner, U. Ugaste, E. Mellikov, M. Kauk, I. Heinmaa, A. Samoson, and A. Medvid. *Point Defects Interaction with Extended Defects and Impurities and Its Influence on the $Si-SiO_2$ System Properties.* Solid State Phenomena, 108-109, 333, 2005.

[91] R.M. Barrer. *Diffusion in and through Solids.* The Syndics of the Cambridge University Press, 1951.

[92] P.G. Shewmon. *Diffusion in Solids.* MacGraw-Hill Book Company, 1963.

[93] J.R. Manning. *Diffusion Kinetics of Atoms in Crystals.* D. van Norstrand Company, 1968.

[94] C.P. Flynn. *Point Defects and Diffusion.* Clarendon Press, Oxford, 1972.

[95] D. Shaw. *Atomic Diffusion in Semiconductors.* Plenum Press, New York, 1973.

[96] B. Tuck. *Introduction to Diffusion in Semiconductors.* IEE Monograph Series 16, Inst. Electr. Eng., 1974.

[97] A.S. Nowick and J.J. Burton. *Diffusion in Solids Recent Developments.* Academic Press, Inc., 1975.

[98] J.P. Stark. *Solid-State Diffusion.* John Wiley and Sons, 1976.

[99] S. Mrowec. *Defects and Diffusion an Introduction, Materials Science Monographs, Vol. 5.* Elsevier, Amsterdam, 1980.

[100] G.E. Murch. *Atomic Diffusion Theory in Highly Defective Solids.* Diffusion and Defect Monograph Series No. 6, edited by Y. Adda, A.D. Le Claire, L.M. Slifkin, F.H. Wohlbier, Trans Tech SA, Switzerland, 1980.

[101] J. Crank. *Free and Moving Boundary Problems.* Oxford University Press, 1984.

[102] G.E. Murch and A.S. Nowick. *Diffusion in Crystalline Solids*. Academic Press, Inc., 1984.

[103] J.S. Kirkaldy and D.J. Young. *Diffusion in the Condensed State*. The Institute of Metals, London, 1987.

[104] R.J. Borg and G.J. Dienes. *An Introduction to Solid-State Diffusion*. Academic Press, Inc., 1988.

[105] B. Tuck. *Diffusion in III-V Semiconductors*. A. Hilger, London, 1988.

[106] I. Kaur, W. Gust, and L. Kozma. *Handbook of Grain and Interphase Boundary Diffusion Data*. Ziegler Press, Stuttgart, 1989.

[107] H. Mehrer. *Diffusion in Solid Metals and Alloys*. Landolt-Boernstein, New Series, Group III, Vol. 26, Springer-Verlag, 1990.

[108] A.R. Allnatt and A.B. Lidiard. *Atomic Transport in Solids*. Cambridge University Press, 1993.

[109] I. Kaur, Y. Mishin, and W. Gust. *Fundamentals of Grain and Interphase Boundary Diffusion*. John Wiley and Sons, 1995.

[110] D.L. Beke. *Diffusion in Semiconductors and Non-Metallic Solids, Subvolume A, Diffusion in Semiconductors*. Landolt-Boernstein, New Series, Group III, Vol. 33, Springer-Verlag, 1998.

[111] M.E. Glicksman. *Diffusion in Solids Field Theory, Solid-State Principles and Applications*. John Wiley and Sons, 2000.

[112] D.S. Wilkinson. *Mass Transport in Solids and Liquids*. Cambridge University Press, 2000.

[113] D.L. Beke. *Nanodiffusion*. Special Issue of J. of Metastable and Nanocrystalline Materials 19, 2004.

[114] A. Gusak. *Diffusion, Reactions, Coarsening Some New Ideas*. Cherkassy National University, 2004.

[115] D. Gupta. *Diffusion Processes in Advanced Technological Materials*. William Andrew, Inc., 2005.

[116] P. Heitjans and J. Kaerger. *Diffusion in Condensed Matter Methods, Materials, Models*. Springer-Verlag, 2005.

[117] H. Mehrer. *Diffusion in Solids. Fundamentals, Methods, Materials, Diffusion-Controlled Processes*. Springer, 2007.

[118] A. Fick. *Annalen der Phyik und Chemie 94*. Philos. Mag. 10, 30, 1855.

[119] J.B.J. Fourier. *The Analytical Theory of Heat*. Translated by A. Freeman, University Press, Cambridge, 1978.

[120] K.D. Elworthy. *Stochastic Differential Equations on Manifolds, in: London Mathematical Society Lecture Note Series*. Cambridge University Press, London, 1982.

[121] N. Ikeda and S. Watanabe. *Stochastic Differential Equations and Diffusion Processes*. North-Holland/Kodansha, Amsterdam, 1989.

[122] N.G. van Kampen. *Stochastic Processes in Physics and Chemistry*. North-Holland Personal Library, New York, 1992.

[123] A.D. Polyanin and V.F. Zaitsev. *Handbook of Nonlinear Partial Differential Equations*. Chapman and Hall/CRC, Boca Raton, 2004.

[124] W.E. Schiesser and G.W. Griffiths. *A Compendium of Partial Differential Equation Models. Method of Lines Analysis with Matlab*. Cambridge University Press, 2009.

[125] W. Jost. *Diffusion in Solids, Liquids, Gases*. Academic Press, Inc., New York, 1952.

[126] J. Crank. *The Mathematics of Diffusion, 2nd edition*. Oxford University Press, 1975.

[127] R. Ghez. *A Primer of Diffusion Problems*. Wiley and Sons, 1988.

[128] M.E. Glicksman. *Diffusion in Solids*. Wiley and Sons, 2000.

[129] H.S. Carslaw and J.C. Jaeger. *Conduction of Heat in Solids*. Clarendon Press, Oxford, 1959.

[130] L. Fox. *Moving Boundary Problems in Heat Flow and Diffusion*. Clarendon Press, Oxford, 1974.

[131] D.V. Widder. *The Laplace Transform*. Princeton University Press, 1941.

[132] J.C. Jaeger and G.H. Newstead. *An Introduction to the Laplace Transformation with Engineering Applications*. London: Methuen, 1949.

[133] R.V. Churchill. *Operational Mathematics.* New York: McGraw-Hill, 1958.

[134] P. Franklin. *An Introduction to Fourier Methods and the Laplace Transformation.* New York: Dover, 1958.

[135] M.R. Spiegel. *Theory and Problems of Laplace Transforms.* New York: McGraw-Hill, 1965.

[136] G.A. Korn and T.M. Korn. *Mathematical Handbook for Scientists and Engineers (2nd ed.).* McGraw-Hill Companies, 1967.

[137] M. Abramowitz and I.A. Stegun. *Laplace Transforms. Ch. 29 in Handbook of Mathematical Functions with Formulas, Graphs, and Mathematical Tables, 9th printing.* New York: Dover, 1972.

[138] F. Oberhettinger. *Tables of Laplace Transforms.* New York: Springer-Verlag, 1973.

[139] G. Doetsch. *Introduction to the Theory and Application of the Laplace Transformation.* Berlin: Springer-Verlag, 1974.

[140] G. Arfken. *Mathematical Methods for Physicists, 3rd ed.* Orlando, FL: Academic Press, 1985.

[141] A.P. Prudnikov, Y.A. Brychkov, and O.I. Marichev. *Integrals and Series, Vol. 4: Direct Laplace Transforms.* New York: Gordon and Breach, 1992.

[142] A.P. Prudnikov, Y.A. Brychkov, and O.I. Marichev. *Integrals and Series, Vol. 5: Inverse Laplace Transforms.* New York: Gordon and Breach, 1992.

[143] A.D. Polyanin and A.V. Manzhirov. *Handbook of Integral Equations.* Boca Raton: CRC Press, 1998.

[144] B. Davies. *Integral transforms and their applications (3rd ed.).* New York: Springer, 2002.

[145] W. Arendt, C.J.K. Batty, M. Hieber, and F. Neubrander. *Vector-Valued Laplace Transforms and Cauchy Problems.* Birkhaeuser Basel, 2002.

[146] U. Graf. *Applied Laplace Transforms and z-Transforms for Scientists and Engineers: A Computational Approach using a Mathematica Package.* Birkhaeuser Basel, 2004.

[147] R.V. Churchill. *Modern Operational Mathematics in Engineering*. New York: McGraw Hill, 1944.

[148] H. Mehrer. *Defect and Diffusion Forum 129130, 57*. 1996.

[149] M. Werner and H. Mehrer. *in: DIMETA-82, Diffusion in Metals and Alloys; F.J. Kedves and D.L. Beke (Eds.)*. Trans Tech Publications, Diffusion and Defect Monograph Series No. 7, 392, 1983.

[150] D.N. Yoon and D. Lazarus. *Pressure Dependence of Ionic Conductivity in KCl, NaCl, KBr, and NaBr*. Physical Review B 5, 4935, 1972.

[151] B.E. Mellander. *Electrical conductivity and activation volume of the solid electrolyte phase α-AgI and the high-pressure phase fcc AgI*. Physical Review B 26, 5886, 1982.

[152] N.H. Nachtrieb, H.A. Resing, and S.A. Rice. *Effect of Pressure on Self-Diffusion in Lead*. Journal of Chemical Physics 31, 135, 1959.

[153] N.H. Nachtrieb and C. Coston. *in: Physics of Solids at High Pressure; C.T. Tomizuka and R.M. Emrick (Eds.)*. Academic Press, 1965.

[154] R.M. Emrick. *Pressure Effect on Vacancy Migration Rate in Gold*. Physical Review 122, 17201733, 1961.

[155] H. Mehrer. *Diffusion in Solid Metals and Alloys*. Landolt-Boernstein, Numerical Data and Functional Relationships in Science and Technology, New Series, Group III: Condensed Matter, Vol. 26, Springer-Verlag, 1990.

[156] D.L. Beke. *Diffusion in Semiconductors and Non-Metallic Solids*. Landolt-Boernstein, Numerical Data and Functional Relationships in Science and Technology, New Series, Group III: Condensed Matter, Vol. 23, Springer-Verlag, 1999.

[157] A.M. Brown and M.F. Ashby. *Correlations for diffusion constants*. Acta Metallurgica 28, 1085, 1980.

[158] G.P. Tiwari, R.S. Mehtrota, and Y. Iijima. *Solid-State Diffusion and Bulk Properties; in: Diffusion Processes in Advanced Technological Materials; D. Gupta (Ed.)*. William Andrew, Inc., 2005.

[159] N.L. Peterson. *Diffusion in Metals*. Solid State Physics 22, 481, 1968.

[160] A.D. Le Claire. *in: Diffusion in Body Centered Cubic Metals; J.A. Wheeler and F.R. Winslow (Eds.).* A.S.M., Metals Parks, 1965.

[161] B.S. Bokstein, S.Z. Bokstein, and A.A. Zhukhvitskii. *Thermodynamics and Kinetics of Diffusion in Solids.* Oxonian Press, New Dehli, 1985.

[162] L.W. Barr and A.B. Lidiard. *Defects in Ionic Crystals, in: Physical Chemistry an Advanced Treatise.* Academic Press, New York, Vol. X, 1970.

[163] A.V. Chadwick and J.N. Sherwood. *Self-diffusion in Molecular Solids, in: Diffusion Processes, Vol. 2; Proceedings of the Thomas Graham Memorial Symposium; University of Strathclyde; J.N. Sherwood and A.V.Chadwick and W.M. Muir and F.L. Swinton (Eds.).* Gordon and Breach Science Publishers, 1971.

[164] A. Einstein. *Uber die von molekularkinetischen Theorie der Waerme geforderte Bewegung von in ruhenden Fluessigkeiten suspendierten Teilchen.* Annalen der Physik 17, 549, 1905.

[165] M. Smoluchowski. *Zur Kinetischen Theorie der Brown'schen Molekularbewegung und der Suspensionen.* Annalen der Physik 21, 756, 1906.

[166] J.R. Manning. *Diffusion Kinetics for Atoms in Crystals.* D. van Norstrand Comp., Inc., 1968.

[167] J. Bardeen nad C. Herring. *Atom Movements.* A.S.M. Cleveland, 1951.

[168] J. Bardeen nad C. Herring. *Imperfections in Nearly Perfect Solids.* Wiley, New York, 1952.

[169] V. Pontikis. *Thermally Activated Processes, in: Diffusion in Materials; A.L. Laskar, J.L. Bocqut, G. Brebec and C. Monty (Eds.).* Kluwer Academic Publishers, Dordrecht, The Netherlands, 1990.

[170] Y. Mishin. *Atomistic Computer Simulation of Diffusion, in: Diffusion Processes in Advanced Technological Materials; D. Gupta (Ed.).* William Andrews, Inc., 2005.

[171] H.B. Huntington and F. Seitz. *Mechanism for Self-Diffusion in Metallic Copper.* Physical Review 61, 315, 1942.

[172] H.B. Huntington. *Self-Consistent Treatment of the Vacancy Mechanism for Metallic Diffusion.* Physical Review 61, 325, 1942.

[173] Z. Jeffries. Transactions of the American Institute of Mining, Metallurgical and Petroleum Engineers 70, 303, 1924.

[174] C. Zener. Acta Crystallographica 3, 346, 1924.

[175] E.O. Kirkendall. Transactions of the American Institute of Mining, Metallurgical and Petroleum Engineers 147, 104, 1942.

[176] A.D. Smigelskas and E.O. Kirkendall. Transactions of the American Institute of Mining, Metallurgical and Petroleum Engineers 171, 130, 1947.

[177] N.L. Peterson. Journal of Nuclear Materials 69-70, 3, 1978.

[178] H. Mehrer. Journal of Nuclear Materials 69-70, 38, 1978.

[179] A. Seeger. *in: Ultra-High-Purity Metals; K. Abiko, K. Hirokawa and S. Takaki (Eds.).* The Japan Institute of Metals, Sendai, 1995.

[180] A. Seeger. Defect and Diffusion Forum 143147, 21, 1997.

[181] O. Sneh, R.B. Clark-Phelps, A.R. Londergan, J. Winkler, and T.E. Seidel. *Thin film atomic layer deposition equipment for semiconductor processing.* Thin Solid Films 402 (1-2), 248261, 2002.

[182] M.D. Groner, F.H. Fabreguette, J.W. Elam, and S.M. George. *Low-Temperature Al_2O_3 Atomic Layer Deposition.* American Chemical Society, 2004.

[183] A. Londergan. *Atomic Layer Deposition Applications 2.* The Electrochemical Society, 2007.

[184] A. Sherman. *Atomic Layer Deposition for Nanotechnology: An Enabling Process for Nanotechnology Fabrication.* Ivoryton Press, 2008.

[185] S.M. George. *Atomic Layer Deposition: An Overview.* American Chemical Society, 2009.

[186] S.M. George. *Applications of atomic layer deposition to nanofabrication and emerging nanodevices.* American Chemical Society, 2009.

[187] H. Kim, H.B.R. Lee, and W.J. Maeng. *Atomic Layer Deposition of Nanostructured Materials.* Thin Solid Films 517 (8), 25632580, 2011.

[188] T. Kaariainen, D. Cameron, M.L. Kaariainen, and A. Sherman. *Atomic Layer Deposition: Principles, Characteristics, and Nanotechnology Applicatons, 2nd Edition*. Wiley, 2013.

[189] R.B. Fair. *Rapid Thermal Processing: Science and Technology*. Academic Press, Inc., 1993.

[190] V. Borisenko and P.J. Hesketh. *Rapid Thermal Processing of Semiconductors*. Springer, 1997.

[191] F. Roozeboom. *Rapid Thermal and Other Short-time Processing Technologies: Proceedings of the International Symposium*. The Electrochemical Society, 2000.

[192] H. Fukuda. *Rapid Thermal Processing for Future Semiconductor Devices*. Elsevier B.V., 2003.

[193] W. Lerch and J. Niess. *Rapid Thermal Processing and beyond: Applications in Semiconductor Processing*. Trans Tech Publications, Inc., 2008.

[194] R.M.A. Azzam and N.M. Bashara. *Ellipsometry and polarized light*. North-Holland Pub. Co., 1977.

[195] H.G. Tompkins. *A User's Guide to Ellipsometry*. Academic Press, San Diego, 1993.

[196] H.G. Tompkins and W.A. McGahan. *Spectroscopic Ellipsometry and Reflectometry: A User's Guide*. John Wiley and Sons, 1999.

[197] H.G. Tompkins and E.A. Irene. *Handbook of Ellipsometry*. William Andrew Pub., 2005.

[198] H. Fujiwara. *Spectroscopic Ellipsometry: Principles and Applications*. Wiley, 2007.

[199] U. Pietsch, V. Holy, and T. Baumbach. *High-Resolution X-Ray Scattering: From Thin Films to Lateral Nanostructures*. Springer, 2004.

[200] E.J. Mittemeijer and P. Scardi. *Diffraction Analysis of the Microstructure of Materials*. Springer, 2004.

[201] M. Birkholz. *Thin Film Analysis by X-Ray Scattering*. Wiley-VCH, 2006.

[202] P. Mueller-Buschbaum. *A Basic Introduction to Grazing Incidence Small-Angle X-Ray Scattering*. Springer, 2009.

[203] R. Guinebretiere. *X-Ray Diffraction by Polycrystalline Materials*. Wiley, 2010.

[204] J. Benavides. *Evaluation of a Procedure for the Measurement of Thin Film Thickness by X-ray Reflectivity*. National Aeronautics and Space Administration, Goddard Space Flight Center, 1997.

[205] J. Daillant and A. Gibaud. *X-ray and Neutron Reflectivity: Principles and Applications*. Springer, 2009.

[206] L.M. Surhone, M.T. Timpledon, and S.F. Marseken. *X-Ray Reflectivity*. VDM Publishing, 2010.

[207] D. Briggs and M.P. Seah. *Practical Surface Analysis -Auger and X-ray Photoelectron Spectroscopy*. Wiley Interscience, 1990.

[208] E. Adem. *VG Scientific XPS Handbook*. VG Scientific, 1991.

[209] N. Ikeo, Y. Iijima, N. Nimura, M. Sigematsu, T. Tazawa, S. Matsumoto, K. Kojima, and Y. Nagasawa. *Handbook of X-ray Photoelectron Spectroscopy*. JEOL, 1991.

[210] J. Moulder, W.F. Stickle, P.E. Sobol, and K.D. Bomben. *Handbook of X-ray Photoelectron Spectroscopy*. Perkin Elmer Corporation (Physical Electronics), 1992.

[211] T.L. Barr. *Modern ESCA - The Principles and Practice of X-ray Photoelectron Spectroscopy*. CRC, 1994.

[212] S. Huefner. *Photoelectron Spectroscopy*. Springer Series in Solid-State Sciences Vol. 82, 1995.

[213] P. Heide. *X-ray Photoelectron Spectroscopy: An introduction to Principles and Practices*. Wiley, 2011.

[214] *The Impedance Measurement Handbook: A Guide to Measurement Technology and Techniques*. Agilent Technologies Co. Ltd, 2000.

[215] A.C. Diebold. *Handbook of Silicon Semiconductor Metrology*. CRC Press, 2001.

[216] E.H. Nicollian and J.R. Brews. *MOS (Metal Oxide Semiconductor) Physics and Technology*. Wiley, 2002.

[217] Y.E. Strausser. *Characterization in Silicon Processing.* Momentum Press, 2010.

[218] S.H. Cohen and M.L. Lightbody. *Atomic Force Microscopy, Scanning Tunneling Microscopy 3.* Springer, 1999.

[219] B. Bhushan, H. Fuchs, and M. Tomitori. *Applied Scanning Probe Methods.* Springer, 2004.

[220] A.S. Lee. *Atomic Force Microscopy Applications in Sensing and Actuation.* ProQuest, 2006.

[221] W.R. Bowen and N. Hilal. *Atomic Force Microscopy in Process Engineering: An Introduction to AFM for Improved Processes and Products.* Butterworth-Heinemann, 2009.

[222] B. Bhushan. *Scanning Probe Microscopy in Nanoscience and Nanotechnology.* Springer, 2010.

[223] P. Eaton and P. West. *Atomic Force Microscopy.* OUP Oxford, 2010.

[224] P. Sigmund. *Theory of Sputtering. I. Sputtering Yield of Amorphous and Polycrystalline Targets.* Physical Review 184, 383; 187, 768, 1969.

[225] C. Andersen and J. Hinthorne. *Ion Microprobe Mass Analyzer.* Science 75,853, 1972.

[226] R. Kelly and J. Sanders. *Recoil implantation from a thin source: I. Underlying theory and numerical results.* Surface Science 57, 143-156, 1976.

[227] H. Storms, K. Brown, and J. Stein. *Evaluation of a cesium positive ion source for secondary ion mass spectrometry.* Analytical Chemistry 49, 2023, 1977.

[228] A. Benninghoven, F. Rudenauer, and H. Werner. *Secondary Ion Mass Spectrometry.* New York, Wiley, 1987.

[229] V.T. Cherepin. *Secondary Ion Mass Spectroscopy of Solid Surfaces.* VSP, 1987.

[230] R. Wilson, F. Stevie, and C. Magee. *Secondary Ion Mass Spectrometry, A practical handbook for depth profiling and bulk impurity analysis.* New York, Wiley, 1989.

[231] K. Wittmaack. *Practical Surface Analysis.* ed. by Briggs and Seah, John Wiley and Sons Chicester, 1992.

[232] P. Zalm. *Ultra shallow doping profiling with SIMS.* Reports on Progress in Physics 58,1321, 1995.

[233] K. Iltgen, C. Bendel, E. Niehuis, and A. Benninghoven. *Secondary Ion Mass Spectrometry SIMS X.* ed. by A. Benninghoven, B. Hagenhoff, H. Werner p.375, Wiley, Chicester, 1996.

[234] J. Grams. *New Trends and Potentialities of ToF-SIMS in Surface Studies.* Nova Science Publishers, Inc., 2007.

[235] K. Sawada, M. Ishida, T. Nakamura, and N. Ohtake. *Metalorganic molecular beam epitaxy of $\gamma - Al_2O_3$ films on Si at low growth temperatures.* Applied Physics Letters 52, 1672, 1988.

[236] M. Kundu, M. Ichikawa, and N. Miyata. *Effect of oxygen pressure on the structure and thermal stability of ultrathin Al_2O_3 films on Si(001).* Journal of Applied Physics 91, 492, 2002.

[237] V. V. Afanasev, A. Stesmans, B. J. Mrstik, and C. Zhao. *Impact of annealing-induced compaction on electronic properties of atomic-layer-deposited Al_2O_3.* Applied Physics Letters 81, 1678, 2002.

[238] G. Lippert, J. Dabrowski, V. Melnik, R. Sorge, Ch. Wenger, P. Zaumseil, and H. J. Mussig. *Si Segregation into Pr_2O_3 and La_2O_3 high-k gate oxides.* Applied Physics Letters 86, 042902, 2005.

[239] S. Abhaya, G. Amarendra, P. Gopalan, G. L. N. Reddy, and S. Saroja. *Study of surface segregation of Si on palladium silicide using Auger electron spectroscopy.* Journal of Physics D: Applied Physics 37, 3140, 2004.

[240] Z. Wang, C. Zhao, P. Yang, L. Winnubst, and C. Chen. *Effect of annealing in O_2 or N_2 on the aging of $Fe_{0.5}Mn_{1.84}Ni_{0.66}O_4$ NTC-ceramics.* Solid State Ionics 177, 21912194, 2006.

[241] M.E. Zvanut, S. Jeddy, E. Towett, G.M. Janowski, C. Brooks, and D. Schlom. *An annealing study of an oxygen vacancy related defect in $SrTiO_3$ substrates.* Journal of Applied Physics 104, 064122, 2008.

[242] G.A. Kimmel and N.G. Petrik. *Tetraoxygen on Reduced TiO_2(110): Oxygen Adsorption and Reactions with Bridging Oxygen Vacancies.* Physical Review Letters 100, 196102, 2008.

[243] S. Park, S. Bang, S. Lee, J. Park, Y. Ko, and H. Jeon. *The effect of annealing ambient on the characteristics of an indium-gallium-zinc oxide thin film transistor.* Journal of Nanoscience and Nanotechnology 11 (7), 6029-6033, 2011.

[244] C.V. Rajan, C.P. Sharma, and A. Sharma. *Heat treatment principles and techniques.* New Delhi: Prentice-Hall of India, 1994.

[245] ed. Y Kuo. *Thin Film Transistor Technologies VI: Proceedings of the International Symposium.* The Electrochemical Society, 2003.

[246] L.B. Freund and S. Suresh. *Thin Film Materials: Stress, Defect Formation and Surface Evolution.* Cambridge University Press, 2003.

[247] J.L. Dossett and H.E. Boyer. *Practical Heat Treating.* ASM International, 2006.

[248] M. Umemoto, Z.H. Guo, and I. Tamura. *Effect of cooling rate on grain size of ferrite in a carbon steel.* Materials Science and Technolog 3(4), 1987.

[249] L.A. Dobrzanski, R. Maniara, and J.H. Sokolowski. *The effect of cooling rate on microstructure and mechanical properties of AC AlSi9Cu alloy.* Archives of Material Science and Engineering 28, 2, 2007.

[250] Z. Ning, P. Cao, H. Wang, J. Sun, and D. Liu. *Effect of Cooling Conditions on Grain Size of AZ91 Alloy.* Journal of Materials Science and Technology 23, 5, 2007.

[251] M. Esmailian. *The effect of cooling rate and austenite grain size on the austenite to ferrite transformation temperature and different ferrite morphologies in microalloyed steels.* Iranian Journal of Materials Science and Engineering 7, 1, 2010.

[252] A. Marmorstein, A.T. Voutsas, and R. Solanki. *A systematic study and optimization of parameters affecting grain size and surface roughness in excimer laser annealed polysilicon thin films.* Journal of Applied Physics 82 (9), 1997.

[253] A.C. Sun, S.C. Chen, P.C. Kuo, C.Y. Chou, Y.H. Fang, J.-H. Hsu, H.L. Huang, and H.W. Chang. *Reduction of Grain Size and Ordering Temperature in $L1_0FePt$ Thin Films.* IEEE Transactions on Magnetics 41, 10, 2005.

[254] S. Heiroth, R. Frison, J.L.M. Rupp, T. Lippert, E.J.B. Meier, E. Mueller Gubler, M. Doebeli, K. Conder, A. Wokaun, and L.J. Gauckler. *Crystallization and grain growth characteristics of yttria-stabilized zirconia thinfilms grown by pulsed laser deposition.* Solid State Ionics 191, 1223, 2011.

[255] C. Herzig and S.V. Divinski. *Grain Boundary Diffusion in Metals: Recent Developments.* Materials Transactions 44, 1, 2003.

[256] Q. Jiang, S.H. Zhang, and J.C. Li. *Grain size-dependent diffusion activation energy in nanomaterials.* Solid State Communications 130, 581584, 2004.

[257] Y.P. Valiev et al. *Grain Boundary Diffusion and Properties of Nanostructured Materials.* Cambridge Int Science Publishing, 2007.

[258] H.M. Zhang and B. Wu. *Size-Dependent Diffusion Coefficient in Nanocrystalline Materials.* Advanced Materials Research 391-392, 2011.

[259] A.W. Ott, K.C. McCarley, J.W. Klaus, J.D. Way, and S.M. George. *Atomic Layer Controlled Deposition of Al_2O_3 Films Using Binary Reaction Sequence Chemistry.* Applied Surface Science 107, 1996.

[260] K.-S. An, W. Cho, K. Sung, S.S. Lee, and Y. Kim. *Preparation of Al_2O_3 Thin Films by Atomic Layer Deposition Using Dimethylaluminum Isopropoxide and Water and Their Reaction Mechanisms.* Bulletin of the Korean Chemical Society 24, 11, 2003.

[261] S.H. Chen, L. Liu, and T.C. Wang. *Small scale, grain size and substrate effects in nano-indentation experiment of filmsubstrate systems.* International Journal of Solids and Structures 44, 13, 2007.

[262] H. Foell. *Al Grain Structure on Different Substrates.* Electronic Materials, University of Kiel, 2010.

[263] W.P. Lin, S. Chu-Hsuan, P.J. Wang, and C.C. Lee. *Microstructures of silver films plated on different substrates and annealed at different conditions.* Electronic Components and Technology Conference 2011, 2011.

[264] P.Q. La, X.J. Zhen, X.F. Lu, Y.P. Wei, C.L. Li, and S.L. Hu. *Effects of Different Substrates on Microstructures and Mechanical Properties of a Bimodal Bulk Nano/Micro Grained 1020 Carbon Steels Prepared*

by Aluminothermic Reaction Casting. Advanced Engineering Materials 16, 2, 2014.

[265] M.M. Sung, G.J. Kluth, and R. Maboudian. *Formation of alkylsiloxane self-assembled monolayers on Si_3N_4.* Journal of Vacuum Science and Technology A 17(2), 1999.

[266] M. Chang, Y. Ju, J. Lee, S. Jung, H. Choi, M. Jo, S. Jeon, and H. Hwang. *Impact of oxygen incorporation at the Si_3N_4/Al_2O_3 interface on retention characteristics for nonvolatile memory applications.* Applied Physics Letters 93, 022101, 2008.

[267] W. Martienssen and H. Warlimont. *Handbook of Condensed Matter and Materials Data.* Springer Handbooks, 2005.